UNIVERSITY OF CALIFORNIA

Los Angeles

Overcoming the Scaling Limitations of Ring-Cusp DC Ion Thruster Discharges

A dissertation submitted in partial satisfaction
of the requirements for the degree
Doctor of Philosophy in Aerospace Engineering

by

Ben Dankongkakul

2017

ABSTRACT OF THE DISSERTATION

Overcoming the Scaling Limitations of Ring-Cusp DC
Ion Thruster Discharges

by

Ben Dankongkakul
Doctor of Philosophy in Aerospace Engineering
University of California, Los Angeles, 2017
Professor Richard E. Wirz, Chair

Ion thruster discharges exhibit impressive performance at conventional scales (∼30 cm in diameter); however, scaling to smaller sizes (∼3 cm) presents considerable challenges. This research effort addresses the miniaturization of direct current (DC) discharges via a series of careful investigations (i.e., near-field cusp-confinement, discharge experiments, computational efforts, and theoretical analyses). These investigations provided insight into the plasma behavior and loss mechanisms within small-scale DC discharges. This insight was then used to develop and demonstrate a highly efficient miniature-scale DC ion source called the Axial Ring-Cusp Hybrid (ARCH) discharge. Implemented as a 3 cm ion thruster, it can potentially achieve a discharge loss of 160 eV/ion and mass utilization efficiencies of 0.89 — performance values that have previously only been attainable by conventional-scale discharges (≥10 cm). The improve performance will greatly expand the mission capabilities of many future spacecraft missions by providing the high efficiency of ion thrusters at small powers and scales.

This thesis describes 3 efforts that were undertaken to better understand cusp-confinement physics and miniature DC discharge behavior. Since small-scale DC discharges are limited by their ability to effectively utilize the high-energy primary electrons, the first effort began with experiments utilizing an electron flood gun to investigate the loss behavior of magnetically-

confined primary electrons. It was found that increasing the complexity of the upstream field affected the spatial complexity of the loss area. These efforts showed that, in contrast to existing theory, the primary electron loss can be strongly influenced by the upstream magnetic fields. This behavior is particularly important and noticeable for miniature-scale discharges where small perturbations of the primary electrons gyro-center are preserved from one cusp to the next. The second effort was then used to investigate the overall confinement behavior of a cusp discharge, to baseline the probing techniques for magnetized plasma discharges, and to validate computational models. It was found that the plasma electron temperature and primary electron density must be analyzed via the electron energy distribution function (EEDF) data. The interpreted primary electron density showed good quantitative agreement with computational simulations.

The final effort was to investigate and improve the discharge efficiency of miniature-scale DC ion thruster discharges. The plasma parameter maps for several magnetic field and discharge conditions were analyzed in conjunction with estimated performance measurements. For the 3 cm Miniature Xenon Ion (MiXI) thruster, the detail discharge maps revealed the mechanisms responsible for the MiXIs flat beam profile and high discharge loss. Analyses of the ionization rates confirm previous computational findings that the plasma within the original MiXI design is created almost entirely by direct primary electron ionization of the xenon gas. Multiple ring cusp configurations (i.e., 3-ring, 4-ring, and 5-ring) were also examined. These efforts revealed that a major redesign is necessary to avoid some of the inherent limitations of ring-cusp discharges at the miniature scale. Ultimately, a new discharge design called the ARCH discharge was developed. Performance data and discharge maps show that this approach provides high primary electron confinement, high plasma electron density, high plasma uniformity along the extraction plane, and discharge performance that may rival well-designed conventionally-sized ion thrusters.

The dissertation of Ben Dankongkakul is approved.

George Morales

Muhamed Abdou

Dan M. Goebel

Pirouz Kavehpour

Richard E. Wirz, Committee Chair

University of California, Los Angeles

2017

Dedicated to mother and father,
for the opportunity and support.

Table of Contents

List of Figures

List of Tables

Acknowledgments

My deep gratitude first goes to my advisor, Prof. Richard Wirz, for the opportunity, guidance, and friendship throughout this endeavor. You took a chance with me, not just by taking me on as your first undergraduate student, but also by continuously supporting me throughout the years. I was an average student with no scholarships, accolades, or noteworthy accomplishments. You saw something in me that I myself didn't and helped me grow into the researcher I am today. It is now quite amusing to reminisce about the early days in the Lab: a large empty room with only 3 desks, a couple bookshelves, and one small unassembled vacuum chamber.

I am also very grateful for the time and support of my graduate committee: Prof. Pirouz Kavehpour, Prof. Muhamed Abdou, and Prof. George Morales, and Prof. Dan Goebel. Thank you Prof. Kavehpour for unintentionally setting me on a path towards my PhD. Thank you Prof. Goebel for everything that I have learned from you. You are a master of your craft and a great role model.

Throughout my long residency in the Wirz Research Group, I have had the great pleasure of getting to know several past and current lab mates: Hann, Jun, Perry, Phil, Lauren, Marlene, Taylor, Sebastian, Ryan, Emily, Chris, Amey, Louis, Mario, Gary, Cesar, Stephen, Ani, and Ryudo. I am very grateful for your friendship and support. I would especially like to thank Jun and Marlene for the countless dinners (and time thinking about where to go for dinner) in and around Westwood. Special thanks also goes to Dr. Taylor Matlock who inspired me to become a better researcher. Your technical expertise and "library catalog" recall of publications will never cease to amaze me.

To my parents, Sumet and Piyaporn, I am eternally grateful for your love and encouragement. I wasn't a very good student throughout grade school. Thank you for having the patience of letting me find my way and always being there for me when I needed your

support.

To my lovely girlfriend, Nicha, thank you so much for your support, love, compassion, etcetera, etcetera. You have been with me through thick and thin, since the beginning of this long journey. I know that it must have taken a lot of love and patience to have always supported me throughout my graduate school career.

Lastly, I would also like acknowledge the financial support from the Air-force Office of Scientific Research through the Young Investigator Program and the UCLA Dissertation Year Fellowship.

Vita

2009	B.S. (Aerospace Engineering), University of California, Los Angeles.
2009	NASA Space Grant - Jet Propulsion Laboratory, research advisor: Dr. Richard Hofer.
2009–2017	Graduate Student Researcher, Mechanical & Aerospace Engineering Department, University of California, Los Angeles.
2010–2014	Teaching Assistant, *Introduction to Astronautics*, Mechanical & Aerospace Engineering Department, University of California, Los Angeles.
2010	Teaching Assistant, *Spacecraft Subsystems & Rocket Propulsion*, Mechanical & Aerospace Engineering Department, University of California, Los Angeles.
2012	M.S. (Aerospace Engineering), University of California, Los Angeles.
2015	NASA Space Grant Award
2015	Dissertation Year Fellowship, University of California, Los Angeles.

Publications

Dankongkakul B. and Wirz R.E., "Axial Ring-Cusp Hybrid (ARCH) Discharge Design: A Highly Efficient Miniature-Scale Ion Source," *Plasma Sources Science and Technology*, June 2017, under preparation.

Dankongkakul B. and Wirz R.E., "Discharge Performance and Behavior of Miniature-Scale DC Ion Thruster Designs," *Journal of Applied Physics*, July 2017, under preparation.

Dankongkakul B. and Wirz R.E., "Design of Miniature Ring-Cusp Ion Thrusters via Discharge EEDF and Plasma Parameter Analysis," *51st AIAA Joint Propulsion Conference & Exhibit*, AIAA 2016-3963, 25-28 July 2016, Salt Lake City, Utah.

Dankongkakul, B., Araki S.J., and Wirz R.E., "Magnetic field structure influence on primary electron cusp losses for micro-scale discharges," *Physics of Plasmas* **21**, 043506 (2014)

Dankongkakul B. and Wirz R.E., "Electron Loss at a Magnetic Cusp for a Range of Upstream Magnetic Field Conditions," *33rd International Electric Propulsion Conference*, IEPC-2013-331, 06-10 October 2013, Washington, D.C.

Dankongkakul B., Araki S.J., and Wirz R.E., "Influence of Upstream Field Structure on Primary Electron Loss for a Permanent Magnet Cusp," *49th AIAA Joint Propulsion Conference & Exhibit*, AIAA 2013-3963, 15-17 July 2013, San Jose, California.

Wirz R.E., Araki S.J., and Dankongkakul B., "Near-Surface Cusp Confinement for Weakly Ionized Plasma," *48th AIAA Joint Propulsion Conference & Exhibit*, AIAA 2012-3948, 30 July - 01 August 2012, Atlanta, Georgia.

CHAPTER 1

Introduction

Ion thrusters and other electric propulsion (EP) systems offer a highly efficient form of space propulsion that are attractive for long distance and/or long duration missions. They are already commonly used for high ΔV orbit station keeping and have also recently been used as a primary propulsion system for deep space missions. Miniature ion thrusters (typically 1-3 cm diameter) are an attractive option for formation flying and attitude control in medium size spacecraft, or for orbit transfer in smaller spacecraft [1, 2, 3]. To date, discharges using ring-cusp designs have exhibited the best efficiency for ion thrusters at all scales [4, 5]. However, smaller ion thrusters exhibit relatively low discharge efficiency due to the inherent increase to the surface area-to-volume ratio of the plasma generation (i.e. discharge) chamber [6]. A better understanding of magnetic cusp confinement to improved discharge efficiency of miniature ion thrusters is needed to enable missions for small spacecraft as well as advance the design of conventional-scale ion thrusters.

Larger scale ion sources ($\geq$10 cm) for space propulsion require higher performance than sources used for terrestrial applications due to more stringent requirements for better efficiencies and lower erosion rates. However, many applications for an ion beam source require only a small beam profile where the advantages of a ring-cusp design heavily taper off. A miniature ion beam source can be used for a wide variety of micro and nano-scale fabrication where low background pressures, high ion energy, and highly anisotropic sputtering is desired. To properly motivate this research, section 1.1 of this chapter provides a general overview of electric propulsion and the need for an efficient miniature to micro-scale ion thrusters. In section 1.2, the overarching dissertation objectives and approach are discussed,

followed by a brief overview of each chapter of this dissertation.

1.1 Background

1.1.1 Electric Propulsion

Electric propulsion (EP) systems generate thrust by using electrical power to impart kinetic energy to the propellant mass. Although they operate under the same action-reaction principle as chemical rockets, EP systems can generate much greater exhaust velocities. The benefits of such a propulsion system is readily apparent by examining the Tsiolkovskly rocket equation written in terms of the propellent mass, m_p:

$$m_p = m_d \left[e^{\Delta v / v_{ex}} - 1 \right] = m_d \left[e^{\Delta v / (I_{sp} \cdot g_0)} - 1 \right], \tag{1.1}$$

where m_d is the delivered mass, Δv is total velocity change of the spacecraft, g_0 is the gravity on the Earth's surface, and v_{ex} is the effective exhaust velocity of the thruster. The equation is also written in terms of specific impulse, I_{sp}, a parameter commonly used to describe the efficiency of rocket engines and is defined as total impulse (change in momentum, p) gained from consuming a unit of propellant weight ($g_0 \Delta m_p$):

$$I_{sp} = \frac{\Delta p}{g_0 \Delta m_p} = \frac{v_{ex}}{g_0}. \tag{1.2}$$

Eq. (1.1) shows an exponential relationship between the exhaust velocity and the minimum propellant required to achieve the mission Δv requirement. While modern chemical rockets typical provide a specific impulse in the range of $300 - 400$ s, modern EP systems are able to achieve a large range of specific impulse from $500 - 10,000$ s [7, 8], depending on the type of EP thruster. Chemical rockets operate on the concept of using exothermic chemical reactions to ultimately impart kinetic energy to the exhaust product/propellent. The energy density, and therefore the theoretical efficiency is limited by the energy yield stored within the

chemical bonds for a given propellent. EP systems have an external electric power source that uses electrical energy to increase the propellant exhaust velocity. The theoretical efficiency of an EP system is thereby limited by the available electric power in conjunction with the mission requirements. On the other hand, EP systems have additional complexities and mass from the power processing system and require larger solar arrays that are not necessary for chemical systems. For high Δv or high payload missions, this mass can easily be offset by the large reduction of the propellant mass. Overall, EP technology can considerably reduce in the mass of the spacecraft and the associated launch cost. It can also enable certain high Δv missions with greater deliverable mass that would not be feasible with chemical rockets.

The main drawback of EP systems is that they generate significantly less thrust. Therefore, to provide equivalent impulse for a mission, EP systems must operate over long thrust times. Whereas the available specific energy limits the specific impulse of chemical systems, the available electrical power limits the thrust of EP systems. Orbital maneuvers are instead accomplished through continuous low thrust operations in the relatively drag-free environment of space. Operating at higher I_{sp} to reduce the propellant mass for a given Δv comes at the expense of the thrust for a fixed electrical power. The thrust is the product of the propellant exhaust velocity and the mass rate at which it is ejected:

$$T = \dot{m}_p v_{ex} = \frac{2}{g_0} \frac{\eta_T P_T}{I_{sp}}. \tag{1.3}$$

The total efficiency (η_T) is defined as the jet (kinetic thrust) power divided by the total electrical input power (P_T) of the device, which can be written as:

$$\eta_T = \frac{T^2}{2\dot{m}_p P_T}. \tag{1.4}$$

Inserting Eq. (1.4) into the equation for thrust leads to the right hand side of Eq. (1.3). The equation shows that, for a fixed electrical power and thruster efficiency, the thrust is inversely proportional to the I_{sp}.

The two most common EP systems used for high Δv missions are Hall and ion thrusters. Ion thrusters are characterized by an ionization chamber for plasma generation and electrostatic grids to accelerate ionized propellant at high velocities. Compared to other EP systems, ion engines have very high exhaust velocities ($I_{sp} = 2500$ to 3600 s) and total efficiencies. Hall thrusters on the other hand, are less efficient but can produce higher thrust for the same available power. Ion thruster also have considerably lower divergence, which is attractive for performance but is also very important for spacecraft integration. For low power thrusters, < 500 W, ion thrusters scale considerably better than Hall thrusters, and are therefore a much better option as a primary propulsion system for small spacecraft and as secondary propulsion system for larger spacecraft.

1.1.2 Miniature Ion Thrusters

Miniature ion thrusters are a low power EP system that is able to provide high specific impulse and precision thrust with low disturbance and plume angle [6]. These capabilities are attractive for a wide range of missions with both small and large spacecraft. The MiXI thruster was identified as a baseline propulsion system for the Terrestrial Planet Finder (TPF) mission to find extrasolar planets [2], shown in figure 1.2. One hundred MiXI thrusters (20 for each of 5 spacecraft) would have been used to achieve precise formation flying and attitude control. Another exoplanet finding mission currently proposed is the New Worlds Mission [9], also shown in figure 1.2, in which the star's light would be blocked by a large occulter to image the orbiting planets. Miniature ion thrusters would be an attractive secondary propulsion system as the starshade occulter would have to be flown in a precise formation 100's of thousands of miles away from the telescope. A recent study by Conversano and Wirz has shown the MiXI thruster can be used to perform a wide range of Earth orbiting missions for a 3U CubeSat, as well as execute a Lunar impact mission from a low Earth orbit [3]. Since this study, many miniature ion thruster missions have been proposed, including a planetary defense system from near-Earth objects (NEO) [10]. Several low-cost CubeSats

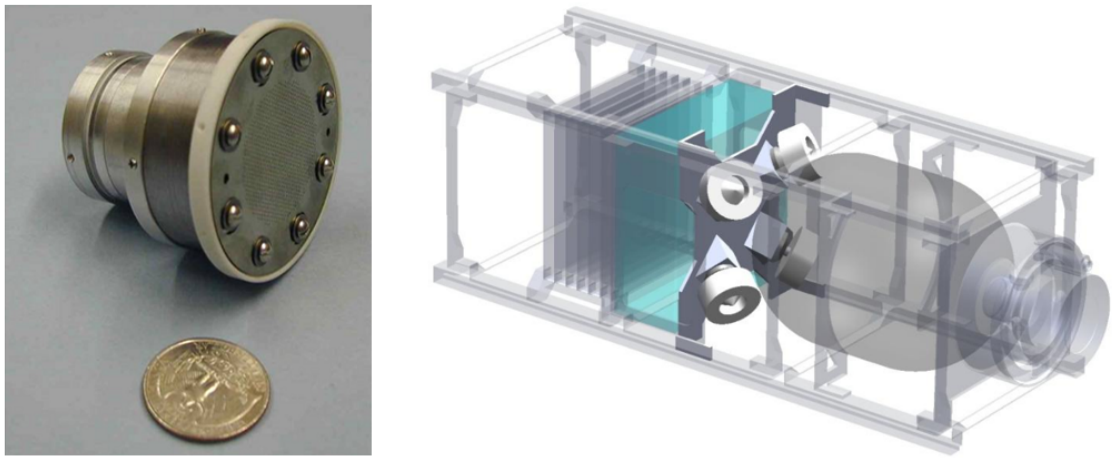

Figure 1.1: Left: image of the the MiXI ion thruster. Right: HiVel 3U CubeSat concept powered by the MiXI thruster [3].

would be used to survey and impact the targets between the orbits of Venus and Mars.

Before the 1980's, miniature scale (< 5 cm) as well as conventional scale ion thrusters operated using cesium or mercury for the propellent gas due to their low ionization energies [6]. These gasses have since been abandoned by modern ion thrusters as they were a hazard to the spacecraft and to engineers. The 3 cm Miniature Xenon Ion (MiXI) thruster developed by Wirz [11], shown in figure 1.1, was the first miniature noble gas ion thruster and provides the highest efficiency for miniature ion thrusters. This was achieved by using a 3 ring-cusp field geometry with a reduced cusp field strength to ensure discharge stability. In addition, improvements to the ion optics allowed for greater gas pressures within the discharge camber without sacrificing the mass utilization efficiency. Table 1.1 is a comparison between published miniature ion thruster systems as well as the conventional-scale XIPS ion thruster. Although radio-frequency (rf) and microwave ion thrusters have certain operational advantages, direct-current (DC) ion thrusters has so far demonstrated the highest discharge efficiencies at all scales [6]. However, compared to conventional-scale ion thrusters (e.g., XIPS-25), the MiXI thruster exhibits relatively low electrical efficiency due to the challenges of scaling miniature DC discharges to smaller scales [12]. These challenges will be discussed in detail in chapter 2.

Thruster Name	Discharge Type	Diameter (cm)	Propellant Efficiency (%)	Electrical Efficiency (%)
MiXI	direct-current	3	42-82	73-67
μNRIT-2.5	radio-frequency	2.5	15-52	4-47
MRIT	radio-frequency	1	80	15.2
MMIT	microwave	2	32	50
μ1	microwave	1.6	46	-
XIPS-25	direct-current	25	82.2	87.5

Table 1.1: Comparison of the efficiencies between the various miniature ion thruster technology. It should be noted that many the of values above do not include efficiency loss from power supplies, cables, and the neutralizer cathode.

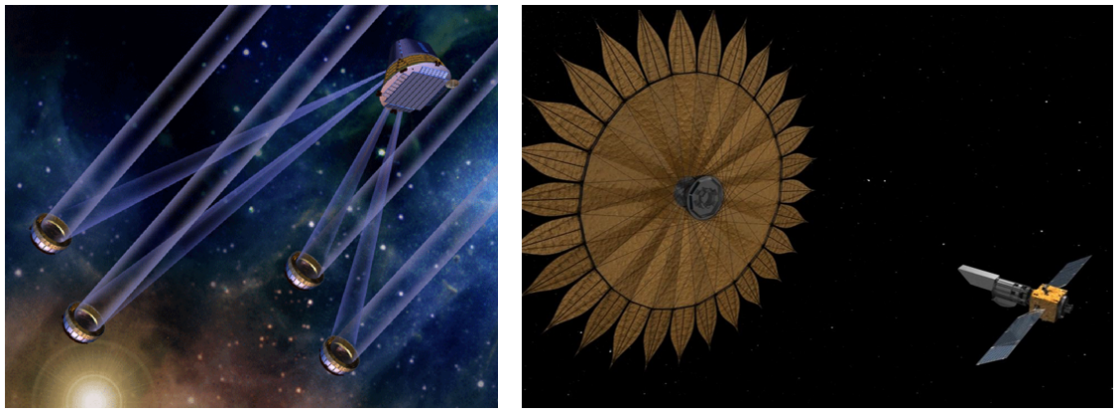

Figure 1.2: Conceptual illustration of the Terrestrial Planet Finder (TPF)-Emma spacecraft (left) [2] and the Starshade Occulter (right) [9].

1.2 Dissertation Objective & Overview

1.2.1 Objective and Approach

The objective of this research effort is to characterize the behavior and limitations of the plasma confinement for miniature ring-cusp discharges; and then use this knowledge to develop and demonstrate a highly efficiency miniature plasma discharge design. The first step in this effort was to investigate the confinement and loss mechanisms of each plasma species for a range of cusp-based magnetic field structures and operating conditions for small and miniature scale discharges. The results from these experiments were coupled with computational and analytical models to understand plasma confinement at small scales. This understanding was then used to develop a new approach to miniature plasma discharge confinement, the "Axial Ring-Cusp Hybrid" (ARCH) discharge.

1.2.2 Chapter-by-Chapter Overview

Throughout this research journey, each successive effort uncovered new insights that informed the subsequent steps. Therefore, a total of three distinct efforts are presented in the main chapters (chapters 3 to 5) of this dissertation, which for the most part, are self-contained. As presented in chapter 6, the results of these efforts led to a new miniature-scale discharge design that can achieve efficiencies that was not thought possible at the time. The following is a brief chapter-by-chapter summary:

Chapter 2 presents an overview of a DC ring-cusp ion thrusters including: the essential components and power supplies, physical processes involved in the thrust generation, and important parameters that are used to characterize their performance. The chapter provides background on the physics of magnetic cusp confinement in relation to how they drive ion thruster design. The chapter concludes with a discussion on the difficulties of scaling down a DC ring-cusp ion thruster.

Chapter 3 covers a range of experiments utilizing an electron flood gun to investigate the loss behavior of energetic primary electrons confined to magnetic fields. Their leak widths to a point-cusp were spatially resolved for a range of upstream magnetic field configurations with increasing complexity: first field-free, then a Helmholtz-field, and lastly a multi ring-cusp field. The experimental measurements were compared to computational simulations and analytical models to understand the mechanisms responsible for the unique leak patterns observed.

Chapter 4 is a transition from investigations into primary electrons to a weakly ionized plasma after learning, per the efforts described in chapter 3 and appendix A, that it is difficult to independently characterize the plasma loss to a single cusp element in a miniature-scale discharge. An 8 cm ring-cusp confined discharge was developed as a multipurpose experiment to baseline probing techniques in a cusp plasma and to validate computational models. This chapter also outlines the discharge mapping approach that was used here and in the following two chapters. Two sets of plasma parameter maps, including the electron energy distribution function (EEDF), were acquired for the entire discharge chamber using two orthogonally oriented Langmuir probes. Each of the plasma parameters were comparatively analyzed to understand how the probe orientation and theories were affected by the magnetic field. A Monte-Carlo Collision (MCC) particle pushing model was also developed (details in appendix B) for which the resulting primary electron density contours compared favorably to the experimental data.

Chapter 5 implements the probing technique developed in chapter 4 to the discharge chamber of the 3-cm MiXI ion thruster. The approach describes a new experimental facility, various modifications to the magnetic field topology of the MiXI discharge, and the simulated ion thruster operations. The discharge maps are found to be an essential tool to understanding the discharge behavior and processes in relation to the thruster's performance parameters. They confirm previous computational results that the original MiXI is a "primary ionizer" because of the under-confined primary electrons and low ionization. Through

analysis of the other magnetic field configurations, this chapter frames the key challenges of miniature ion thruster development and the tools/approaches used to address them.

Chapter 6 details the design of the Axial Ring-Cusp Hybrid (ARCH) discharge. The chapter describes the operating principle of the ARCH design and how it simultaneously addresses each of the key challenges discussed in chapter 5. The simulated performance measurements show that the ARCH discharge is over 2.5 times more efficient than the previous state-of-the-art and was able to achieve discharge efficiencies similar to conventional scale ion thrusters. In conjunction with discharge maps, the data show that the primary electrons were almost completely confined from the walls and that the bulk plasma was efficiently generated along the extraction plane. The chapter concludes with a discussion on possible improvements and the scalability of the ARCH design.

Chapter 7 summarizes the insights and conclusions drawn from the preceding chapters. There is a discussion of the major findings and contributions to the field of miniature DC discharges and ion thrusters. Future work relating to both the design and physical processes of miniature plasma discharges are recommended.

CHAPTER 2

Discharge Performance of Direct Current Ring-Cusp Ion Thrusters

This chapter presents an overview of the basic operating principles of a direct-current (DC) ion thruster along with a brief discussion on the relevant plasma processes and interactions. There is a review of the metrics and parameters generally used to characterize the performance of ion thrusters that is important for chapter 5 and chapter 6. Furthermore, most modern DC ion thrusters have adopted a ring-cusp magnetic field configuration for plasma confinement to improve the discharge efficiency and a brief review of cusp confinement is covered in section 2.3. Lastly, this chapter addresses the specific challenges and inherent difficulties involved in scaling down these devices.

2.1 Ion Thruster Operation

A simple diagram of a miniature electron-bombardment ring-cusp ion thruster is shown in figure 2.1 along with the key components and power supplies. The discharge chamber is backfilled with the neutral propellant gas, typically xenon in most modern ion thrusters. High-energy (primary) electrons are emitted from the discharge cathode, which directly and indirectly ionizes the neutral gas to generate a partially ionized plasma. Ions that are incident to the ion optic grids are extracted from the plasma and accelerated to high exit velocities by the electric field established between the upstream screen grid and the downstream accelerator grid. The neutralizer cathode outside of the discharge chamber emits

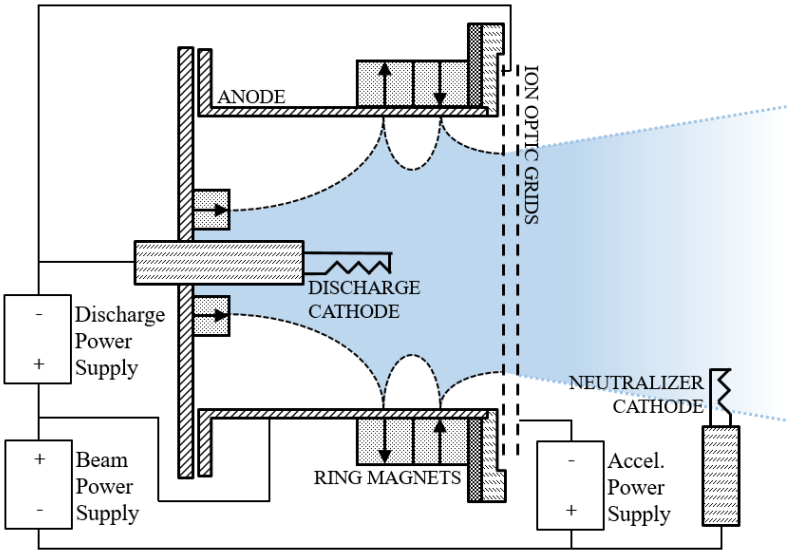

Figure 2.1: Basic component and circuit diagram of the MiXI thruster. The diagram does not include the heater power supplies for the discharge and neutralizer cathodes.

electrons to effectively neutralize the ion beam and prevents the spacecraft from accumulating a net negative potential relative to the space potential.

Flight ion thrusters utilizes a hollow cathode as oppose to a heated tungsten filament for the discharge and neutralizer cathodes. The relatively high work function of a tungsten filament ($\sim$4.5 eV) requires high heater power to reach emission temperatures and consequently generates much more waste heat. In addition, filaments have short lifetimes due to evaporation and ion sputtering from the discharge plasma. The design of the hollow cathode addresses both of these issues by creating a region of dense, low temperature plasma inside a thermally insulated refractory tube. The propellent gas is injected down the tube where it is ionized by electrons emitted from a low work-function insert, typically barium oxide or lanthanum hexaboride. The insert is generally designed to be self-heated, either directly through ion bombardment of the insert or indirectly through orifice heating. The high neutral density ensures low electron temperatures and low plasma potentials inside the cathode, which reduce sputtering of the insert.

The plasma generation inside the discharge chamber can be accomplished with a direct-

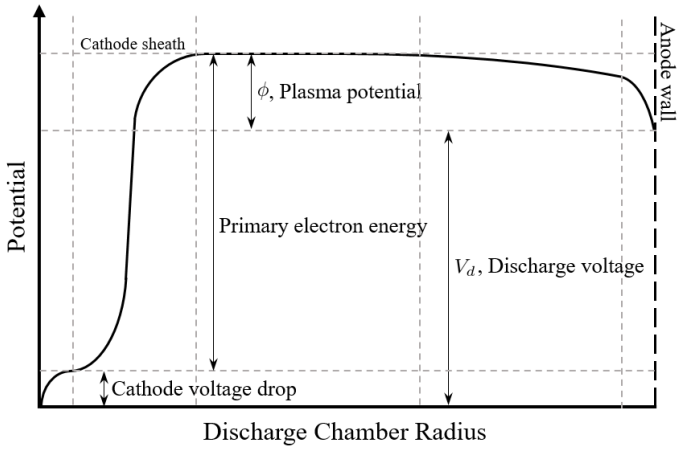

Figure 2.2: Illustration of the radial potential profile of a DC ion thruster discharge.

current (DC), radio-frequency (rf), or a microwave discharge. However, DC discharges were investigated for this work as they exhibit the highest efficiencies for both large and small scale thrusters [8, 6]. In a DC ion thruster, the power required for plasma generation is provided by a continuous current of high energy electrons from the discharge cathode. The anode surfaces of the chamber are biased to a discharge voltage ($\sim$25 V) relative to the discharge cathode. As illustrated in figure 2.2, the bulk plasma is typically at a positive plasma potential relative to the anode voltage. The potential self-consistently establishes a negative-going sheath towards the anode to maintain quasi-neutrality between the fast-moving electrons and the heavy, slow-moving ions. Primary electrons emitted at the discharge cathode are immediately accelerated by the cathode sheath to energies sufficient to ionize the neutral atoms. The energetic primary electrons encounter few large-angle elastic collisions during their lifetimes. They independently traverse the discharge chamber in a manner governed by the Lorentz force until they either encounter an inelastic collision or are collected at the chamber walls. The discharge energy carried within the primary electron population is lost to four dominate mechanisms:

1. Ionization collisions: a primary electron collides with a neutral atom and sufficient energy is transferred to free a bounded electron, ionizing the atom. After the collision, a positively charged ion and low-energy "plasma electron" pair is generated. For typ-

ical DC discharges, where the incident primary electron possesses ∼20 eV of energy, the post-collision primary electron has sufficiently low energy that it is unlikely to encounter another ionization or excitation collision with a heavy particle. Therefore, the primary can generally be assumed to rapidly thermalize with the plasma electron population afterward. Primaries can also collide with ions to generate doubly-charged ions. However, these events are rare for a properly designed ion thruster discharge.

2. Excitation collisions: similar to ionization collisions but the energy transferred to the atom is only sufficient to promote a bounded electron to a higher energy state. The interaction does not generate any additional species and the excited neutral atom will eventually emit a photon when it reverts back to its ground state. As with ionization collisions, the post-collision primary electron is rapidly thermalized.

3. Thermalization: through several inelastic collisions with the plasma electrons, the primary electron eventually joins and its energy transferred to the Maxwellian plasma electron population.

4. Wall losses: primary electrons with a directional energy sufficient to overcome the sheath will contact the chamber wall where its remaining energy is loss in the form of heat.

The probability of each of above interaction has an associated collision cross-section, length-scale, or reaction rate that is strongly dependent on the discharge chamber design and operating condition. For higher plasma electron temperatures, the high-energy tail of the Maxwellian plasma electron population can account for most of the ionization or excitation of the neutral gas. The high-energy tail can also have energies sufficient to generate doubly-charged ions from the singly-charge ion, where the rate can be significant in a highly ionized plasma (∼10%). The generation of double ions is detrimental to the efficiency and lifetime of the ion thruster. The ionization potential is higher and they impact the cathode surfaces at twice the energy of a singly-charged ion.

As shown in figure 2.1, the entire discharge chamber is biased to a beam voltage (∼1000-1500 V) relative to the space ground potential (or neutralizer cathode potential). Since the plasma potential is small compared to the beam voltage, ions are ejected from the thruster at near the applied beam voltage. The ion optics are a set of multi-aperture grids that are designed to extract the ions from the discharge plasma, focus the ion beam, and contain the neutral gas. The screen grid is in direct contact with the discharge plasma and is biased to or below the discharge cathode potential to reflect electrons. The screen grid has a high ion transparency to minimize its contact with the discharge plasma and thus, ions lost to the grid. The accelerator (accel) grid is closely spaced downstream of the screen grid and is biased below the neutralizer cathode or space potential. This negative bias is set to prevents electrons from the neutralizer cathode from backstreaming into the discharge chamber, which would lead to high electrical loss. The accel grid has a low geometric transparency to reduce the loss of neutral gas but are still sufficiently open to allow the focused beamlet of high energy ions to exit the thruster. Some ion thrusters have an additional decelerator (decel.) grid downstream of the accel. grid that is biased to space potential to mitigate erosion of the accel grid. Charge-exchange (CEX) collisions between the beam ion and the escaping neutral gas will generate a low-energy ion within or downstream of the ion optics. A sizable fraction of these low speed ions is trapped within the potential well of the negatively biased accel. grid and will impact the grid with enough energy to sputter the grid material. The decel. grid reduces the length of the potential well and shields the accel. grid form most of CEX ions that are generated downstream of the ion optics. There are many other important factors, such as voltage breakdown and thermal expansion, that determines the design of the ion optics that is not discussed here.

2.2 Ion Thruster and Discharge Performance

Chapters 5 and 6 focus on the optimization of the discharge chamber in order to improve the discharge performance. This section reviews the important metrics used to characterize

ion thruster designs and understanding the macroscopic discharge behaviors. This will only be a brief overview of the necessary formulations and more detail can be found in many references as summarized in Goebel and Katz [13].

Unlike most other forms of electric propulsion, the propellant ejected from an ion thruster is essentially mono-energetic. The ions within the discharge chamber have a negligible thermal spread and the variation in the plasma potential is small compared to the applied beam voltage. Therefore, the total efficiency, Eq. (1.4), can be expressed as:

$$\eta_T = \frac{T^2}{2\dot{m}_p P_T} = \gamma^2 \eta_e \eta_m, \tag{2.1}$$

where η_e and η_m are defined as the electrical and mass utilization efficiency, respectively. The total thrust correction factor, $\gamma = \alpha F_T$, accounts for multiply-charged species (α) and divergence in the ion beam (F_T). This α term is generally greater than 90% in most ion thrusters. The double ion correction factor is defined as the singly and doubly-charge ion ratio of the total beam current:

$$\alpha = \left(1 + \frac{\sqrt{2}}{2}\frac{I_B^{ii}}{I_B^{i}}\right) \Bigg/ \left(1 + \frac{I_B^{ii}}{I_B^{i}}\right), \tag{2.2}$$

where I_B^i and I_B^{ii} are the total singly and doubly-charged ion currents, respectively. The electrical efficiency is defined at the total kinetic power in the ion beam divided by the total input power supplied to the thruster system:

$$\eta_e = \frac{I_B V_B}{I_B V_B + I_d V_d + P_0}, \tag{2.3}$$

where I_B and V_B are the beam current and voltage, I_d and V_d are the discharge current and voltage, and P_0 accounts for any additional power required to operate the ion thruster system. This includes the cathode heater and keeper power, currents to the grid system, and the efficiency of the power supplies. The mass utilization efficiency is defined as the fraction

of the total propellant input into the system that is ejected as beam ions:

$$\eta_m = \frac{I_B^i + 0.5\, I_B^{ii}}{\dot{m}_p} \left(\frac{m_i}{e}\right), \tag{2.4}$$

where $\dot{m}_p$ is the total propellant flow rate, m_i is the mass of the ion, and e is the electron charge. Operation with a neutralizer hollow cathode requires an additional propellant flow external to the discharge chamber. For conventionally sized ion thrusters, this flow rate accounts for a small ratio of the total flow rate and has minor impact to the propellant utilization efficiency. For miniature ion thrusters, the additional gas flow and possibly keeper power may have a more significant impact to the total efficiency. Although this may also be mitigated by sharing a single neutralizer cathode amongst multiple ion engines or by further development of miniature hollow cathode technology.

The electrical efficiency includes the electrical power required to accelerate the ion beam, which is generally several times greater than that needed to generate the beam ions. Therefore, a more useful metric to gauge the performance of the discharge chamber is the discharge loss parameter, which is a ratio of discharge power to the ion beam current [W/A]. This can also be thought of as the energy needed to produce a single beam ion [eV/ion], and is defined by:

$$\epsilon_B = \frac{I_d V_d + I_k V_k}{I_B}, \tag{2.5}$$

where I_k and V_k accounts for the hollow cathode keeper power that may conditionally be required to maintain stable operation of the discharge cathode.

Figure 2.3 is an example plot of a standard performance curve which describes the discharge loss in relation to the propellant utilization efficiency. Each curve typically represents a constant beam current or throttle setting. The "performance knee" corresponds to an optimal condition where the discharge operates at peak total efficiency for the desired beam current. The conditions to the far left of the knee is characterized by a very weakly ionized plasma. Direct ionization collisions between the primary electrons and neutral gas is the

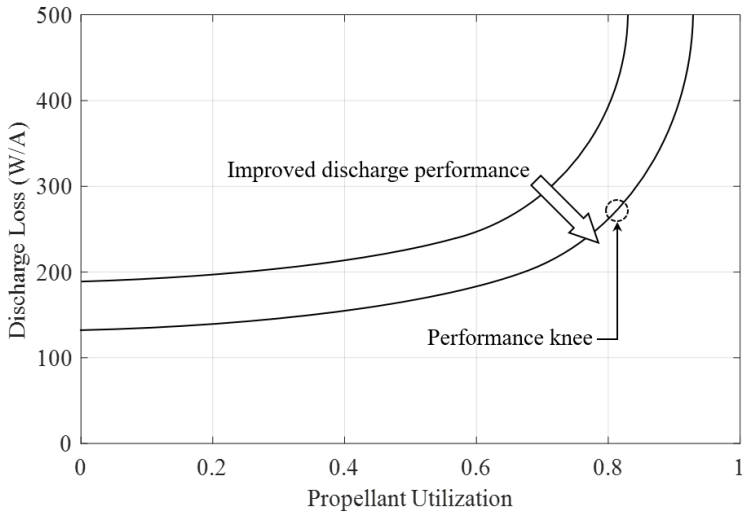

Figure 2.3: Illustration of standard ion thruster performance curves. The curves typically represent a constant beam current.

dominate mechanism for ion generation and there is excessive un-ionized propellant escaping the discharge chamber. Moving pass the optimal knee to the where the curve begins to vertically asymptote, the conditions are characterized by a more highly ionized plasma and increasing plasma electron temperatures. As the plasma density increases and the neutral density depletes, a greater percentage of the primary electrons are colliding/thermalizing with the plasma electrons rather than directly ionizing the propellant. The higher electron temperature and ionization leads to a non-linear increase to the diffusion rates and thus, plasma loss to the chamber walls.

The distribution of plasma along the extraction plane is another important parameter for discharge chamber design. This can be assess by the ion beam density along the extraction plane and is defined as the radial averaged beam current density over the peak beam current density ($j_{B_{MAX}}$):

$$F_B = \frac{2}{R_g^2 j_{B_{MAX}}} \int_0^{R_g} j_B(r) r dr, \tag{2.6}$$

where r is the radial coordinate measured from the center-line, R_g is the grid radius, and j_B is the local beam current density. The beam profile reflects the plasma distribution inside

the discharge chamber which can be strongly influenced by the magnetic field topology. A poor beam flatness parameter will lead to faster erosion of the grids and lower performance since the device will be limited by the tolerable erosion or heating at the location that has the highest beam current density. For example, the 30 cm NSTAR ion thruster has a poor beam flatness parameter with a strong center-line peak in the beam profile caused by axial confinement of the primary electrons. This confinement causes a high relative density of primary electrons, which leads to a reduction of neutral xenon density and a surfeit of xenon ions. The coupling of these effects heightens doubly-charged ion generation along the axis that leads to poorer discharge performance, faster screen grid erosion (a common life-limiter for ion thrusters), and possibly increased accel. grid erosion [14].

For a mono-energetic beam of single ions, the I_{sp} and thrust is calculated from previously defined terms via:

$$I_{sp} = \frac{\gamma \eta_m}{g_0} \sqrt{\frac{2eV_b}{m_i}}, \tag{2.7}$$

$$T = \gamma J_B \sqrt{\frac{2eV_b}{m_i}}. \tag{2.8}$$

Therefore, the performance of most ion thrusters can be accurately accessed without having to directly measure the thrust. Most of the efficiency terms can be calculated by careful measurements of the current and voltage output of the various power supplies. Only the total thrust correction factor and the beam flatness parameter require measurements of the ion beam plume. The plume measurements are simple to obtain except for the doubly-charged ion content, which generally has a small effect on the performance of a properly designed thrusters.

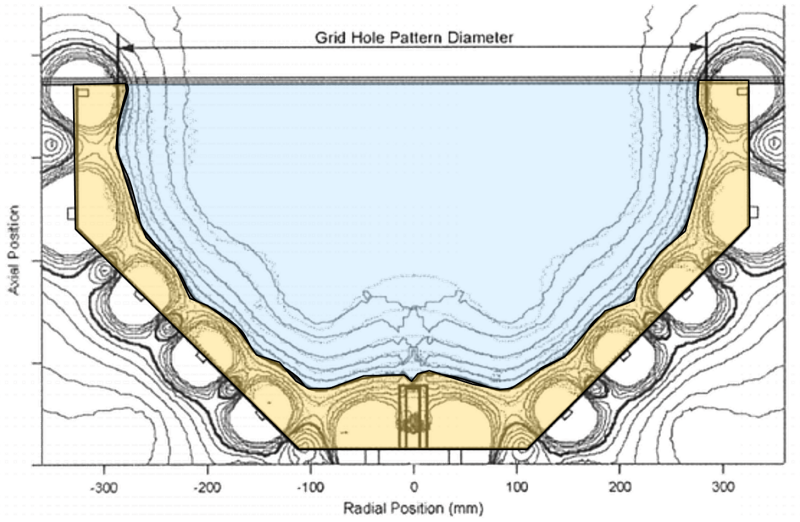

Figure 2.4: The magnetic field contours of the 65 cm Nexis ring-cusp ion thruster [15].

2.3 Magnetic Cusp Confinement

Magnetic cusps are commonly used for plasma confinement to achieve higher overall plasma densities and improved efficiencies of both ion thrusters and laboratory discharges [16, 17, 18]. They serve to increase the confinement path length of the primary electrons as well as reduce the effective diffusion rate of plasma to the chamber walls. For low-beta plasma, ring-cusp and Kaufmann type discharges have been effective in generating nearly uniform un-magnetized plasma of relatively high densities for applications which include plasma processing, electric propulsion, and experiments for plasma physics research. Figure 2.4 is a diagram of the 65-cm NEXIS ion thruster with the magnetic field strength contour. Most conventional-scale ion thrusters have adopted a ring-cusp design using samarium cobalt permanent magnets that have very strong but short-ranged cusp magnetic fields. When the ring-cusp elements are placed in an alternating pattern along the discharge chamber walls, they create a strong cusp confinement boundary near the walls that provide desirable plasma confinement. Collectively, the ring-cusps cancel one another in the far-field region and the electrons are unmagnetized throughout most of the discharge chamber volume. This provides a large "field-free" plasma volume to generate a relatively uniform plasma profile

across the extraction plane for a high beam flatness.

2.3.1 Magnetic Mirroring

An important feature of a magnetic cusp is the mirroring of the high energy primary electrons from the chamber walls. The ionization collision mean free path for the primary electrons is generally much longer than the size of the chamber for standard plasma conditions and raising the neutral density too high leads to lower mass utilization efficiency. Instead, magnetic cusp fields are used to increase the effective path length and residence time of the primaries while still allowing for sufficient plasma electron leakage to the anode necessary to maintain the discharge current. The non-collisional trajectories can be represented by the Lorentz equation which describes a charge particle motion in an electromagnetic field:

$$\mathbf{F} = m\frac{\mathrm{d}\mathbf{v}}{\mathrm{d}t} = q(\mathbf{E} + \mathbf{v} \times \mathbf{B}), \tag{2.9}$$

where $\mathbf{E}$ and $\mathbf{B}$ are the local electric and magnetic field, respectively, and m, $\mathbf{v}$, and q are the particle's mass, velocity, and charge, respectively. The equation shows that magnetized charged particles travel with a helical path line around and along the magnetic field lines. The radius of the circular component is described as the Larmor radius:

$$r_l = \frac{mv_\perp}{qB}, \tag{2.10}$$

where $v_\perp$ is the particle's velocity component parallel to the local magnetic field lines. The parallel component is unaffected by the magnetic field. Combining Eq. (2.9) with the divergence-free property of magnetic fields, $\nabla \cdot \mathbf{B} = 0$, the first adiabatic invariant can be derived:

$$\frac{\mathrm{d}}{\mathrm{d}t}\left(\frac{mv_\perp^2}{2B}\right) = \frac{\mathrm{d}\mu}{\mathrm{d}t} = 0, \tag{2.11}$$

where μ is defined as the magnetic moment of the particle. The magnetic moment is constant for a particle that remains confined to the magnetic field. The expression can then be combined with conservation of energy, $v_0^2 = v_\perp^2 + v_\parallel^2$, to obtain the standard expression for magnetic mirroring written in the form:

$$\frac{B_0}{B_c} = \frac{1}{R_m}, \tag{2.12}$$

where B_c and B_0 are the magnetic field at the particle's initial location and at the cusp where it is loss, respectively. The mirror ratio, R_m, represents the fraction of particles loss to the cusp assuming a one sided isotropic velocity-space distribution.

In a ring-cusp ion thruster, the cusp-boundary reduces the anode area that is exposed to the bulk plasma. The non-collisional primary electrons freely traverse the low field region, reflecting back and forward until they are eventually lost to one of the cusps. Their average path length within the chamber (the confinement length) in the absence of collisions can be approximated as:

$$l_c = \frac{V_{dis}}{A_{loss}}, \tag{2.13}$$

where V_{dis} is the volume of the discharge plasma. A_{loss} is the total loss area of primary electrons, defined as:

$$A_{loss} = 2r_p L_c, \tag{2.14}$$

where r_p is the primary electron Larmor radius and L_c is the combined total azimuthal length of all the ring-cusp elements. The primary electron confinement can then be estimated through a probabilistic collision analysis:

$$P = 1 - \exp(-n_0 \sigma_{in} l_c), \tag{2.15}$$

where n_0 is the neutral gas density, σ_{in} is total inelastic collision cross-section, and P is the probability that the primary electron will be lost to the plasma rather than the walls.

2.3.2 Anisotropic Diffusion within Ion Thruster Discharges

The discharge plasma, except at the sheath boundaries, is considered to be quasi-neutral, meaning that the ion and electron densities are effectively equal. However, there is a large disparity between the mass and velocity of the oppositely charged species. In a non-magnetized plasma, the ambipolar effect ensures that the local flux of ions and electrons are generally equal or else there will be an accumulation of charges. The plasma establishes a small but self-consistent electric field that slows down the fast electrons and accelerates the slow ions. The result is the ambipolar diffusion rate for the combined ion and electron transport that is in between the diffusion rates of the individual species.

In a magnetic field, the light plasma electrons are confined to any appreciable field strength which inhibits their transport across the field lines. Unlike the primary electrons, the plasma electron trajectories are not invariant at the cusp due to the high collisionality. The heavier ions, ie. argon and xenon, are unmagnetized and in most circumstances, their transport across the magnetic field is instead inhibited by ambipolar effects with the confined electrons. This leads to an anisotropy between the plasma diffusion rate along and across the magnetic field lines. The cross-field diffusion rate can either be described as either classical or non-classical (anomalous) diffusion. In the classical theory, charge particles diffuse across field lines through scattering collisions with the neutral background. In a fluid treatment, the derived diffusion coefficient has an inverse-squared dependency on the magnetic field strength. For anomalous diffusion theory, collective plasma instabilities can lead to cross-field transport faster than what can be described by classical theory. The measured diffusion rate in devices with large $\boldsymbol{E} \times \boldsymbol{B}$ drifts has shown to scale closer with the Bohm diffusion coefficient [19], which is inversely proportional to the magnetic field strength.

There is a long history of research characterizing the plasma transport rate through a cusp magnetic field. Many of these experiments were performed using relatively larger plasma discharges with free-standing electromagnetic "picket fence" and spindle cusps [20, 17, 21] or multi-magnet ring and line cusps for permanent magnet discharge [22, 23, 24]. For these

discharges, researchers have consistently defined and demonstrated a semi-empirical "leak width" through which the plasma is lost at the cusp. This behavior has been described by using an ambipolar-type description of the interaction between the ions and electrons within the cusp region [25, 26]. Several researchers have found the leak width, w_l, to be proportional to the hybrid gyroradius r_h, such that:

$$w_l \approx 4r_h = 4\sqrt{r_e r_i}, \tag{2.16}$$

where r_i and r_e are the ion and electron Larmor radii and r_h is effectively a geometric mean of the two radii. Although several researchers have also shown the leak width to scale with the neutral pressure or alternatively in accordance to Bohm diffusion in certain conditions, the hybrid Larmor radius is widely used for modeling of ion thruster discharges [11, 27].

2.4 Discharge Design Consideration

For a given chamber size, the total cusp area is commonly described by the number of ring-cusp elements. The peak field strength at the surface of a permanent magnet does not increase much after a certain thickness of the magnets. Increasing the width of the ring-cusp primarily causes the cusp magnetic fields to penetrate further into the far-field. From a primary electron confinement perspective, it would be ideal to minimize the total cusp area to increase the confinement path length. On the other hand, the discharge current must be collected at the anode to sustain the discharge current via the plasma electrons. Over-confinement of the plasma electrons will drop the plasma potential as necessary to extract more electrons through the sheath. This directly reduces the primary electron energy and can lead to an unstable discharge if the plasma potential becomes sufficiently negative relative to the anode voltage [28].

In addition to the total cusp area, the placement and orientation of the ring-cusp elements are important to the ion confinement and for obtaining a flat beam profile. The "highest

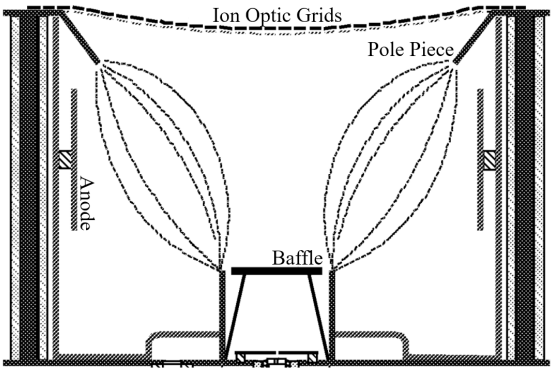

Figure 2.5: Diagram of the T6 Kaufmann ion thruster [30].

closed field contour" is commonly used figure of merit to assess the ion confinement [15, 29]. This value is strongly dependent on the inter-cusp magnetic field strength and is roughly illustrated in figure 2.4 as the contour line separating the two regions. In addition, the magnetic field topology should be designed to maximize the region of low magnetic field, particular along the extraction plane. It is also important to ensure the primary electrons that are emitted from the hollow cathode are able to disperse throughout the discharge chamber.

2.4.1 Alternative Designs

Although this research initially focuses on improving ring-cusp discharges, it was found that Kaufmann and Magneto-Electrostatic or magnetic multipole field [31] discharges have features that are advantageous for primary electron confinement at the miniature-scale. They are used in many of the discharge configurations investigated in chapter 5 and the Axial Ring-Cusp Hybrid (ARCH) discharge in chapter 6. Figure 2.5 is a diagram of the T6 Kaufmann ion thruster. Unlike a ring-cusp discharge, a Kaufmann discharge does not have any magnetic fields from the bulk plasma that terminate at anode surfaces. In this way, the plasma is confined by a diverging axial magnetic field of moderate strength. The non-diffusive primary electrons are not lost to the anode and the discharge current is sustained by cross-field transport of the plasma electrons. There is a delicate balance with the axial

field strength to sufficiently confine the plasma without encountering the discharge stability problems described above for an over-confined discharge. For terrestrial applications, the discharge cathode is generally a filament that spans across a large radial distance in order to generate a uniform ion beam. Flight Kaufmann thrusters have hollow cathodes which emit as a point source. A baffle system is required to injects the primary electrons off-axis to prevent a strongly-peaked beam profile. However, the baffle leads to a high cathode voltage drop which directly reduces the primary electron energy for a given discharge voltage. Therefore, Kaufmann ion thrusters must operate at higher discharge voltages ($\sim$35 V). where the anode is also located at the inter-cusp region in between cathode terminated ring-cusps. The multipole discharge has a magnetic field topology that is slightly similar to a ring-cusp discharge. However, the magnetic cusps terminate at cathode potential and the anode in located within the inter-cusp regions. Similar to Kaufmann discharges, the electrons must diffuse across the field lines to reach the anode.

2.4.2 Discharge Scaling

The primary challenge of miniaturizing a ring cusp ion thruster is the increase surface area-to-volume ratio of the discharge chamber and more directly, the small overall discharge volume. The efficiency of ring cusp discharges relies on having a sufficient primary electron confinement length relative to the inelastic collision mean free path. This confinement length decreases at a cubed rate relative to the discharge chamber diameter. There are limitations on the strength and number of ring cusps because the overall magnetic field topology still has to be considered in the design. In addition, experimental observations by Wirz [12] and Mao and Wirz [32] have shown that using strong magnets can over confine the plasma electrons and create an unstable discharge. The device can be operated at higher neutral and plasma densities to partially mitigate the decreased confinement length since the collision mean free path scales proportionally to the particle density. However, aside from the thermal considerations, the maximum plasma density will still be perveance limited by the ion optics

and thus the neutral density will be limited by the lower propellant utilization efficiency.

The difficulties are further exacerbated by the inherent nature of the permanent magnet fields. Conventional-scale ion thrusters benefit from the rapid decrease in the ring-cusp field strength, which provides a near-boundary confinement at the walls while maintaining a large low field region in the bulk region for plasma uniformity. These boundary characteristics become a volumetric effect in the miniature scale as the strong cusp fields penetrates deep into the discharge chamber. This further reduces the overall discharge volume and leads to strong magnetic fields gradients throughout the entire chamber volume.

CHAPTER 3

Primary Electron Confinement Dynamics

The first experiments of this dissertation investigated the physical processes of primary electron confinement within a magnetic cusp. They are of importance in a MiXI-like discharge where computational models suggest that they account for up to 10% of the total electron population [33]. Furthermore, primary election ionization collisions are the sole mechanism for ion generation because of the low electron temperature. The prevailing theory and experimental data show that the primary electron loss width is approximately twice the electron gyroradius [26, 20, 24]. Although the expression for the hybrid loss width, Eq. (2.16), is only dependent of the ion and plasma electron population, some researchers have suggested that the hybrid leak width can also be strongly influenced by the presence of primary electrons along with plasma properties [21, 34, 35]. The primary electron's elastic and inelastic collisional mean free paths are generally on the order of the chamber size and thus are relatively unaffected by the plasma potential structure and other plasma species. Their dynamics are dominated by the magnetic field structure and their transport can generally be independently studied and simulated with knowledge of macroscopic plasma conditions.

Experiments were developed around an electron flood gun that was used to generate fast electrons. The spatial current density of the primary electrons was measured at a permanent magnet point-cusp for a range of upstream magnetic field topology. The primaries were found to be lost at twice their gyro-radius for an isolated point-cusp in accordance to conventional theory. However, it was found that increasing the complexity of the upstream fields also increased the complexity of the loss pattern. The same phenomena were repeated using a computational simulation and described with an analytical model; both requiring accurate

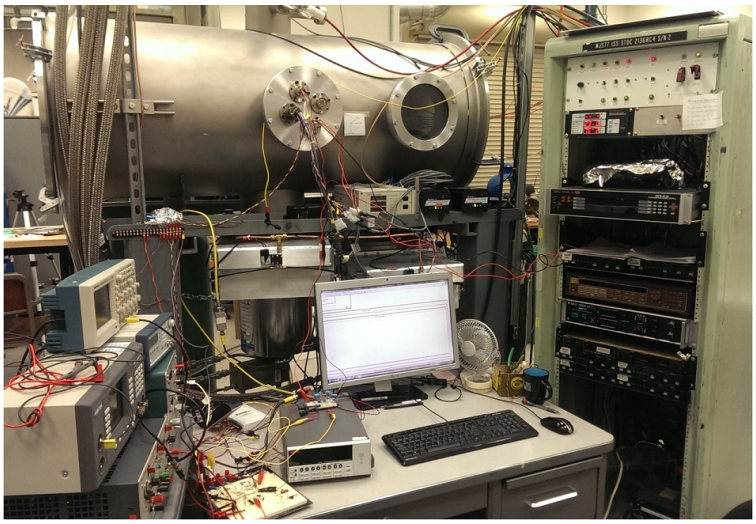

Figure 3.1: The vacuum facility where the cusp experiments are conducted.

sampling of the magnetic fields. The findings from this chapter changed the course this research which was to first characterize the individual cusp loss for each plasma species for a range of cusp elements. The dependency of the primary electron loss behavior, as well as the other plasma species (appendix A), to the overall magnetic field structure indicated that a holistic approach must be taken to improve the performance of miniature-scale discharges.

3.1 Approach

3.1.1 Experimental Facility

All experiments in this chapter were conducted at the UCLA PSPL Micro-Propulsion facility shown in figure 3.1. The chamber was brought to vacuum using two 10" CTI Cryo-Torr cryogenic pumps which provided a total pumping speed of 5000 l/s for argon gas and achieves a base pressure of 3×10^{-8} Torr. The partial gas pressures were measured using a residual gas analyzer and an a hot-filament ionization gauge calibrated for the dominant gas. Inside the chamber is a 3-axis translation stage system with a multi-function mount for diagnostics with various probes. The stages were each driven by a vacuum-prepped

Figure 3.2: The Kimball Physics EGA-1012 electron flood gun.

stepper motor and controlled through LabVIEW with a Velmex VXM-1 motor controller. The overall system was capable of 2000 step/cm automated scans and positional data were confirmed with string potentiometer installed onto each axis.

The electron source was the Kimball Physics EGA-1012 electron flood gun, shown in figure 3.2. The source can be mounted both inside or outside the vacuum chamber depending on the experiment. It provided a well-characterized electron source that was easily adjustable to user-specified electron energies and emission currents. The manufacturer advertises that it is able to produce 2 mA of beam current up to 1000 eV with only 0.5 eV of thermal spread. However, primary electrons in ion thrusters typically operate at < 35 eV where only ~ 30 μA of beam current is available from the gun. The electron gun was used instead of a hot filament emitter with a biased anode because the experiment did not aim to generate a quasi-neutral plasma. Without a plasma, the positively biased anode relative to the cathode filament would create a global electric field inside the device that is not representative of the fields inside a plasma discharge. The gun could produce electrons at primary energies independent of the plasma potential and without the need for a plasma discharge.

The current profile loss to the conducting wall at the magnetic point-cusp was measured using either a wire probe or an embedded wall probe shown in figure 3.3. The wire probe was a simple tungsten wire strung across and isolated from a supporting structure. The wire was long enough to span across the entire collection region as it was translated across the

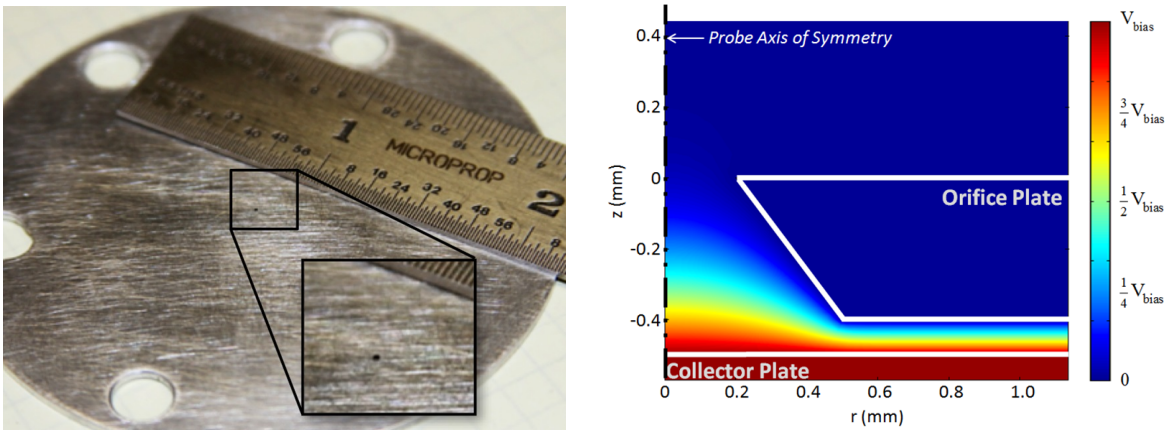

(a) Image **(b)** Diagram

Figure 3.3: The "wall probe" which is designed to measure particle wall loss very near a permanent magnet cusp. The diagram shows that the potential structure from a biased collector plate remains predominately within the orifice plate.

cusp. The wall embedded probe was designed to measure charged particle flux in a non-Debye shielded environment by suppressing the far-field impact from biasing of the probe's collector plate. The probe featured a 0.4 mm chamfered orifice upstream of the collector plate. The entire assembly was 1.2 mm thick, which enabled loss measurements very near the face of the point cusp magnet. The potential contour in figure 3.3b, shows the collector plate biased at -40 V with respect to the orifice plate. The result demonstrates minimal disturbance of potential upstream of the orifice plate, and therefore, minimal expansion of the effective collection area. The probe was mounted onto the translational stages for 2D raster scans at the point cusp.

3.1.2 Particle Simulation

To analyze the data obtained from the experiment, an iterative Monte Carlo electron tracking model was developed and simulated by Araki [36]; it was used to gain a better understanding of the observed loss behavior. The model used analytical equations for magnetic fields induced by permanent block [37] and cylindrical [38] magnets for accurate deter-

mination of the magnetic field at the particle location. This approach minimizes the error associated with interpolation of the fields, particularly very near the cusps. A modified Boris method was used to integrate of the equation of motion, which used a predictor-corrector algorithm in order to accurately capture the circular motion of the electrons in the magnetic field [39, 14].

3.2 Single Point Cusp

3.2.1 Experimental Setup

The first experiment utilizing the electron flood gun source measured the collection area in the simplest of cusp configuration. As shown in figure 3.4, the electron gun was aimed directly at a single cylindrical permanent magnet while measurements were taken using a thin wire probe at chamber base pressure. An AlNiCo magnet was chosen to generate a weaker cusp to obtain a larger leak width and, hence, provide a higher measurement resolution within the cusp region. The electron gun was spaced at an adequate distance from the cusp to allow the electrons to be born in a relatively field free environment. The data was used to validate and characterize the electron gun and to validate components of the simulation

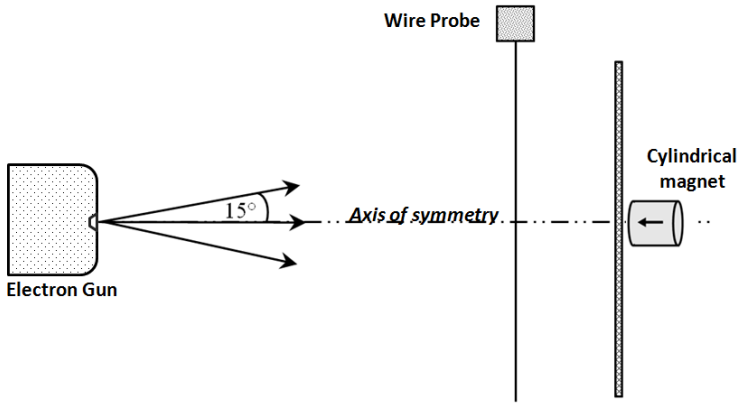

Figure 3.4: Diagram of the single cusp experiment. Wire probe sweeps were taken for a range of distances from the cylindrical point cusp magnet.

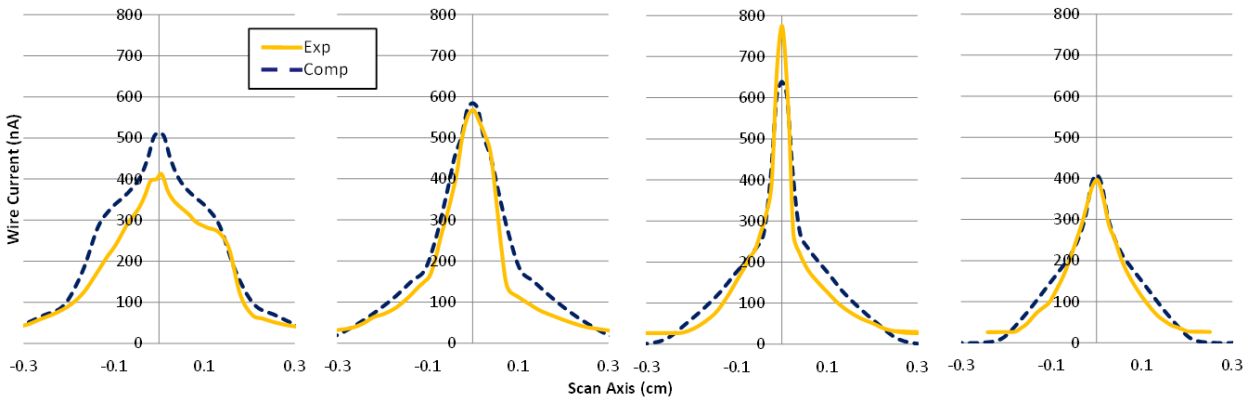

Figure 3.5: Experimental (Exp) and computational (Comp) wire probe measurements across the cusp at 5.5 mm, 4.5 mm, 3.5 mm, and 2.5 mm from the permanent magnet face show good agreement. A fluctuating peak current density and loss width are caused by the point injection of electrons.

model.

3.2.2 Results and Discussion

Figure 3.5 is a comparison between the experimental data and computational results of the line current density profile at incremental distances upstream of the target magnet shown in figure 3.6. For these data, 50 μA of electron current was injected at an energy of 25 eV with 15° half angle divergence. Wire probe measurements were taken at 1 mm axial increments starting from 2.5 mm upstream of the target magnet. The results show a decreasing total current moving towards the magnet surface as electrons are reflected. The line current data can be converted to a current density profile using a reverse Abel transformation; however, the data presented herein is kept unprocessed for direct comparison with the virtual wire scans generated by the simulation results.

The electron loss width at the cusp measures within 2 to 4 times electron gyro-radius. The apparent fluctuations in the line current density and the overall loss width is a consequence of the point source of the electrons. They are ejected from the electron gun towards the cusp with an axis-symmetric distribution that cause the them to gyrate at a semi-synchronous

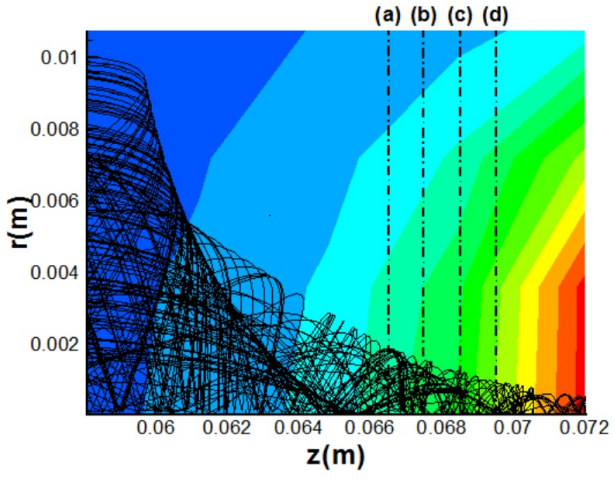

[b!]

Figure 3.6: Sample computational trajectories of primary electrons incident to a cylindrical permanent magnet. The dotted lines corresponds to the location of the simulated wire probe measurements shown in figure 3.5.

trajectory. Therefore, most of the population will roughly converge at the centerline after a full gyro-rotation. A semblance of this effect can be discerned by examining the sample particle traces in figure 3.6. The computational results show a good quantitative and qualitative agreement to the experimental data. This indicates that the particle tracking technique and the magnetic field calculations are accurate. One possible cause of the slight disagreement is the misalignment of the magnet and electron gun axis during the experiment, as seen in the asymmetric scan profile in the data.

3.3 Helmholtz to Single Cusp

3.3.1 Experimental Setup

The Helmholtz-cusp experiment shown in figure 3.7, incorporated two additional magnetic field elements to the single cusp experiment to control the upstream magnetic field. The field in the bulk region incident to the cusp was adjusted through the Helmholtz coils while the cathode coil controlled the field at the electron gun. The configuration created a

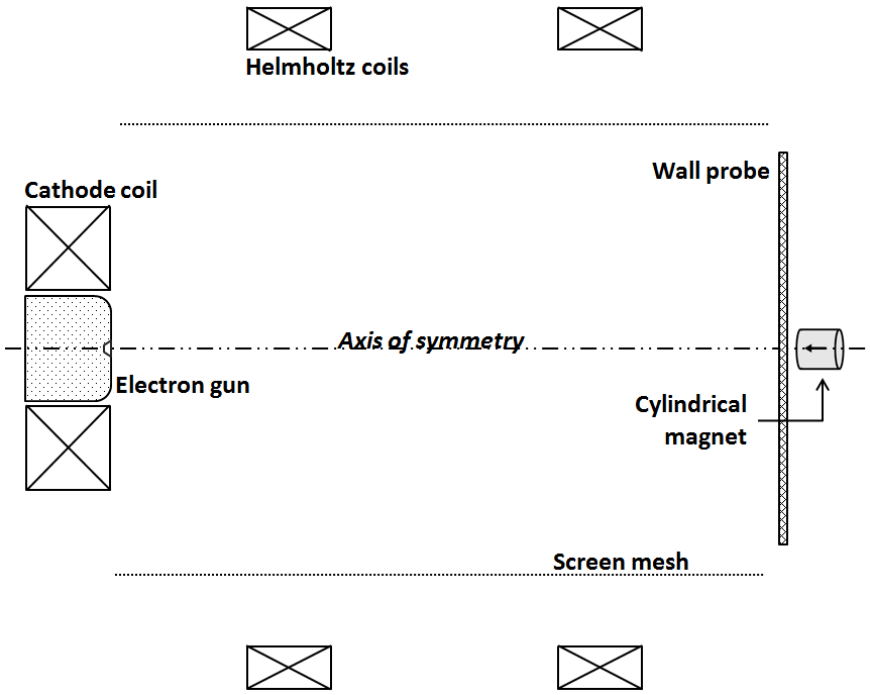

Figure 3.7: Diagram of the Helmholtz cusp experiment. Current density measurements were taken along the r-θ plane at the cylindrical point cusp target magnet using the wall probe.

magnetic bottle where the electron confinement can be adjusted. Particles lost at the cylindrical permanent magnet were measured using the wall probe, which is kept at a grounded potential. The grounded screen mesh prevented undesirable charging of insulated surfaces from affecting the electron trajectories.

3.3.2 Results and Discussion

The experiment was operated with the magnetic field strength at the cusp and the uniform upstream region at 1600 Gauss and 60 Gauss, respectively. In addition, the cathode coil and electron gun were electrically floated to create an electrostatic reflective boundary. Measurements with these surfaces at ground potential gave expected results at the point-cusp similar to the previously discussed single cusp experiment. The results shown in figure 3.8 are planar measurements taken 3 mm upstream of the target magnet with the electron gun

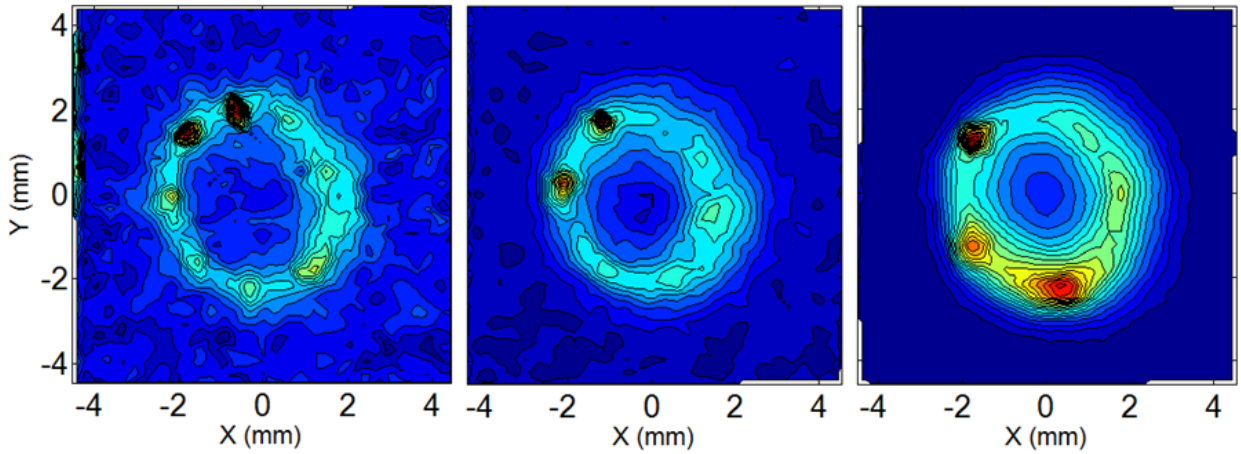

Figure 3.8: Contour plots of the current density measured 2 mm upstream of the target magnet face at base pressure with primary electron energies at 15 eV (left), 25 eV (center), and 35 eV (right). The contours are plotted on a linear scale with a maximum current density of 14 $\mu A/m^2$ (left), 32 $\mu A/m^2$ (center), and 88 $\mu A/m^2$ (right). Orientation is from the perspective of the cylindrical magnet viewing upstream.

energies of 15 eV, 25 eV, and 35 eV. At all energies, the results display an annular collection region of the same radius of $\sim$2 mm. However, the angular separation of the current density peaks within the ring increases with higher election energies. The loss width of the individual peaks is within the order of magnitude of the electron gyro-radius.

The annular collection area at the cusp was caused by a combination of the non-axial entry of the electrons to the centerline magnetic field and the azimuthal drifts in the cusp region. Unlike the single cusp experiment, the initial electron population was confined from birth to the upstream magnetic field. As illustrated in figure 3.9, they were guided to the cusp region slightly off-axis and underwent a finite curvature and ∇B drift in the azimuthal direction along a "drift shell" that surrounded the centerline. The multiple current density peaks were a result of subsequent mirroring cycles of the less confined population from the electron gun in combination with the finite drift precession of each cycle. The lower current density ring in which the peaks coincide was caused by electrons that have become part of the diffuse background population after several reflections. To do an analysis of the angular precession of the current density peaks, the combined expression for the two drifts can be

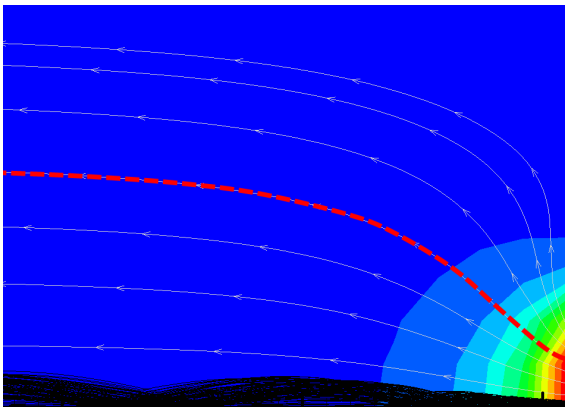

Figure 3.9: Magnetic field contour and field lines of the Helmholtz-cusp configuration. The black lines are simulated particle tracking results for electrons injected at the axis of symmetry. The dotted red line illustrates a guiding center path an electron could follow if injected off-axis.

integrated:

$$\begin{aligned}\Delta\theta_d\left(r,z\right) &= \frac{1}{r}\int\left(v_{\nabla B}+v_{R_c}\right)\mathrm{d}t \\ &= \frac{1}{r}\int\left[\frac{m}{q}\left(v_{\parallel}^2+\frac{1}{2}v_{\perp}^2\right)\frac{\vec{R}_c\times\vec{B}}{R_c^2B}\right]\frac{\mathrm{d}z}{v_{\parallel}},\end{aligned} \tag{3.1}$$

where m is the electron mass, q is the elementary charge, and $v_\perp$ and $v_\parallel$ are its velocity component perpendicular and parallel to the magnetic field, respectively. R_c is the radius of curvature of the magnetic field, and $\Delta\theta_d$ is the integrated drift in the azimuthal direction. The instantaneous velocity components can be related to the magnetic field through the basic equations for magnetic mirroring using $v_\perp \approx v_0 \sin\gamma\sqrt{B/B_0}$ and $v_\parallel \approx \sqrt{v_0^2 - v_\perp^2}$, where γ is the initial pitch angle. Combining these terms give the expression:

$$\Delta\theta_d\left(r,z\right) = \frac{m}{q}v_0\int\left(\frac{\vec{R}_c\times\vec{B}}{R_c^2B}\right)\frac{2+\frac{B}{B_0}}{\sqrt{1+\frac{B}{B_0}}}\frac{\mathrm{d}z}{r}. \tag{3.2}$$

To calculate the actual drift values would require numerical integration along the particle's guiding center trajectory as well as the local magnetic field data. However, electrons emitted from the source are confined to the same initial guiding center field lines regardless of their

energies because the magnetic field is unchanged for each test. Therefore, the value of the integral in Eq. (3.2) is constant and independent of the electron's initial velocity. The total azimuthal precession is then found to be directly proportional to the velocity of the electrons:

$$\Delta\theta_d \propto v_0 \propto \sqrt{\varepsilon}, \tag{3.3}$$

where ε is the total energy of the electrons. This dependency can be readily seen in figure 3.8 through the angular spacing between each subsequent current peaks in the annular rings.

3.4 Multi-Cusp Confinement

3.4.1 Experimental Setup

The experiment shown in figure 3.10 was a 3 cm ring-cusp confinement device designed to examine primary electron collection behavior at a magnetic point cusp. The electron flood gun was spaced a short distance from the chamber as to not exceed the cathode's maximum operation pressure of 10^{-5} Torr at the emission surface. Injected electrons that entered the device were then confined by multiple ring cusp magnets located behind the radial wall and a cylindrical point cusp magnet behind the downstream wall probe. Xenon neutral gas was injected upstream through a gas feed plenum which pressurized the device from the facility base pressure to the desired background pressure.

The permanent magnets were configured to replicate a ring-cusp confinement condition within a miniature discharge device; a point-cusp magnet at the end of the discharge allowed for measurements of electrons loss to a single cusp. The point-cusp was a cylindrical samarium cobalt magnet, while the ring magnets were composed of individual samarium cobalt block magnets stacked and oriented as shown in figure 3.10. In the azimuthal direction, each ring magnet around the chamber and electron gun had 18 blocks and 16 blocks, respectively. Similar to other ring-cusp discharges, discrete block ring magnets were used in

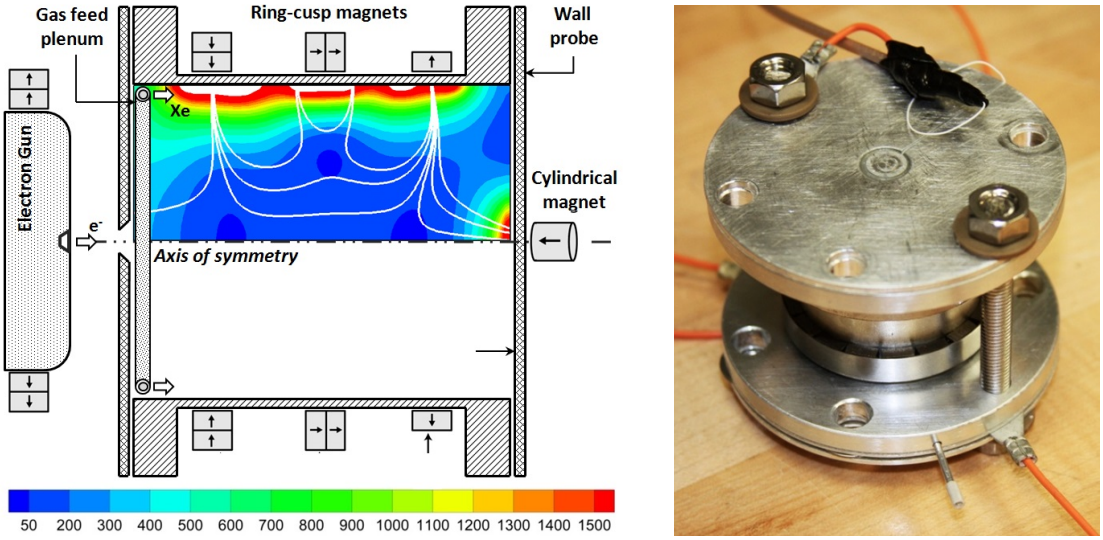

(a) Diagram **(b)** Image

Figure 3.10: Diagram of the experimental setup overlaid with the magnetic field contour (Gauss) and field lines. Current density measurements were taken upstream of the cylindrical point cusp magnet using the wall probe.

lieu of a continuous ring magnet to account for possible thermal expansion of the discharge chamber. The magnetic topology contained 4 ring-cusp of decreasing field strength in the downstream direction to coerce electrons toward the point cusp. The current and spatial location of particles are lost to the point-cusp were measured using the moveable wall probe which also served as the downstream wall of the device.

3.4.2 Results and Discussion

For the data presented in figure 3.11, the electron gun was operated at a constant 35 eV electron energy and 15° divergence angle in absence of magnetic fields. Although the energy is higher than that normally found in an ion thruster, the setting allowed for higher emission currents for better signal-to-noise at the point-cusp. All surfaces in the device including the wall probe's collector plate were kept at ground potential. The current density measurements taken at base pressure (figure 3.11a) exhibited a current density peak close to the center of the cylindrical magnet with an azimuthal pattern of radially aligned ridges. The loss width

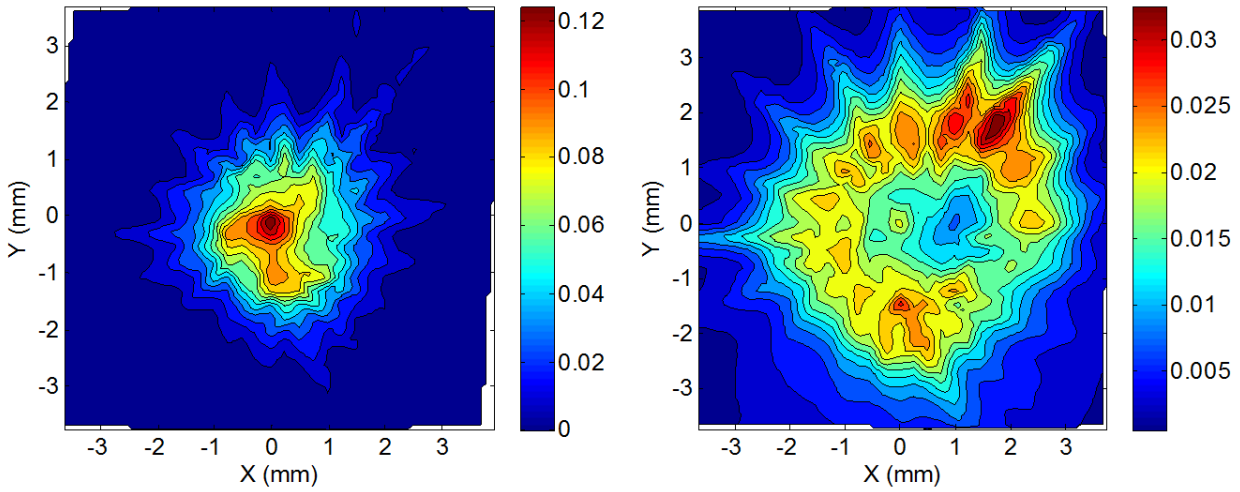

Figure 3.11: Contour plots of the current density (A/m^2) measured 2 mm upstream of the cylindrical magnet face at (left) base pressure of 3×10^{-8} Torr and (right) xenon pressure of 5×10^{-4} Torr. Orientation is from the perspective of the cylindrical magnet viewing upstream.

measures between ∼1.6-2.0 mm Full Width at Half Max (FWHM), depending on whether the fringe of the ridge structures is included. These values are more than an order of magnitude greater than the electron Larmor radius of ∼0.1 mm for the field strength at the collection surface.

Figure 3.11b shows the result with the addition of xenon neutral gas at 5×10^{-4} Torr. These data show a periodic loss structure of coinciding "peaks and ridges" that surrounds the point cusp with a general trend of decreasing current density in counterclockwise direction. Although the azimuthal position and total number of the ridges remain unchanged from the base pressure result, the spatial distribution of current is significantly altered and the highest current density is located off-axis at a radius of ∼2 mm. While the average angular spacing for the 18 block magnets are 20°, the angle between each of the ridges range from 16° to 27°. This angular spacing and the azimuthal orientation of the ridges was similar for experimental conditions over a range of election energies and xenon pressures. The total ion current collected at the point cusp by biasing the probe's collector plate to 40 V is more than two orders of magnitude less than the electron current and has negligible impact to the

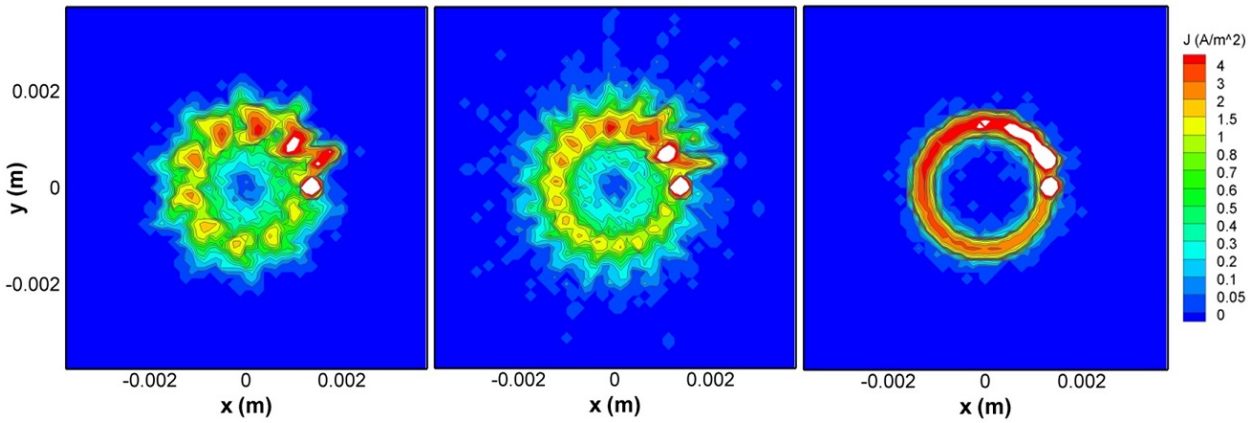

Figure 3.12: Simulation result for current density (A/m^2) for ring magnets composed of 10 and 18 block magnets, and a continuous ring magnet. Within the white contour, the current density values exceed 7 A/m^2.

presented data. Plasma properties calculated based on the discharge condition suggests that the plasma is not quasi-neutral and that the primary electron trajectories remain largely non-collisional and non-diffusive.

The computational simulations were conducted by changing the number of block magnets that form the ring-cusp element immediately upstream of the point-cusp while maintaining constant total magnet volume. The results for the current density at the point-cusp, shown in figure 3.12, were generated for cases where the adjacent ring magnet is composed of 10 blocks, 18 blocks, and a single continuous magnets. They show a similar loss pattern to the experimental data with "peaks and ridges" of current density that surrounds the point cusp center. The correlation of the quantity of ridges to the ring magnet segments suggests that the ridge structure was a result of the discrete magnets used for the upstream ring cusp.

A counter clockwise reduction of the current density around the point-cusp is seen in both the experimental and computational results shown in figure 3.11 and figure 3.12, respectively. This behavior is caused by a combination of guiding center drifts in the azimuthal direction and the continuous electron loss to the cusps upon the localized injection of the particles. Among the various guiding center drifts, curvature and grad-B drifts are found to be the most dominant types of drifts in this experiment. The null region of a ring-cusp created a

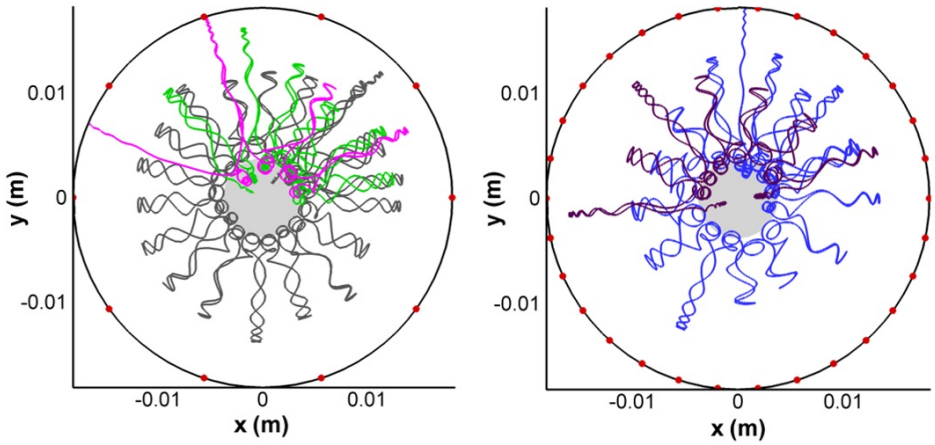

Figure 3.13: Particle trajectories of electrons confined between the point-cusp and the directly upstream ring-cusp comprising of 10 block magnets (left) and 30 block magnets (right). Dots around circumference represent locations of block magnet centers. Particles travel along magnetic field lines and undergo an impulsive turning event near the ring-cusp null region.

region where the field lines had a short radius of curvature with low field strength because of the radially opposing fields. As seen in figure 3.13, confined particles generally travel along the magnetic field lines and only experience a short azimuthal turning event near the null region. Particles that reside radially further and therefore in the regions of lower drift, experience a smaller angular precession per reflection event. For the conditions simulated, the nominal azimuthal precession is not determined by the number of block magnets.

To examine the cause of the peak and ridge structures, an approximate analytical description of the axial drifts of the electrons between the point cusp and the closest ring cusp is discussed. First, there is a strong periodicity of the azimuthal field near the ring cusp produced by the discrete magnets. This asymmetric field gives rise to drifts in the axial direction across the field lines. From the particle trajectories used to generate the results shown in figure 3.12, the electron loss to the furthest downstream ring cusp on the θ-z plane is shown in figure 3.14a. These results show a slight discontinuous zig-zag loss pattern across the face of a ring cusp block magnet. Although the deviations are small, the forthcoming analytical description shows that a shift in the guiding center location can translate to larger

shifts in the particle trajectory further downstream where the field is weaker. Figure 3.14b shows magnetic field lines traced from the simulated loss locations in figure 3.14a onto the r-z plane. These field lines represent the electron guiding center and show a noticeable difference in paths between different azimuthal planes.

Based on the observations from the preceding figures, a simplified analytical description was used to describe the impact of an axial drift on the collection pattern at the point-cusp for an off-axis population of confined electrons between the point-cusp and adjacent ring-cusp. Like the Helmholtz-cusp analysis, the combined curvature and grad-B drift for an individual electron can be integrated along the radial direction by assuming its trajectory is purely radial and adiabatic invariant. The integrated value then represents the total drift in the axial direction for particles reflected at each spatial location. Since the axial drift is greater at the high field cusp region, the drift values are scaled to account for the expansion of the field lines in the radial direction, Δz_w; this is approximated by assuming constant magnetic flux in the z-direction at each radial cross-section.

$$\Delta z_w = \Delta z_d \frac{rB}{r_w B_w}. \tag{3.4}$$

Here, r_w and B_w represent the radius of the chamber wall and the associated magnetic field strength, respectively. As diagrammed in figure 3.15, Δz_w is an effective axial drift displacement across field lines normalized to the condition at the ring-cusp wall. In addition, the total value is doubled to account for the reverse trajectory after the reflection. The final expression can then be rewritten as,

$$\Delta z_w\left(r,\theta\right) = 2\frac{mv_0}{qB_w r_w}\int_{r_0}^{0}\left(\frac{\vec{R}_c \times \vec{B}}{R_c^2 B}\right)\frac{2+\frac{B}{B_0}}{\sqrt{1+\frac{B}{B_0}}} r\mathrm{d}r, \tag{3.5}$$

where r_0 is the radial location of reflection. Figure 3.15 is a contour plot of Eq. (3.2) and represents the normalized axial drift for electrons reflected at each spatial location within the plane. The result indicates the existence of a non-negligible alternating axial drift for

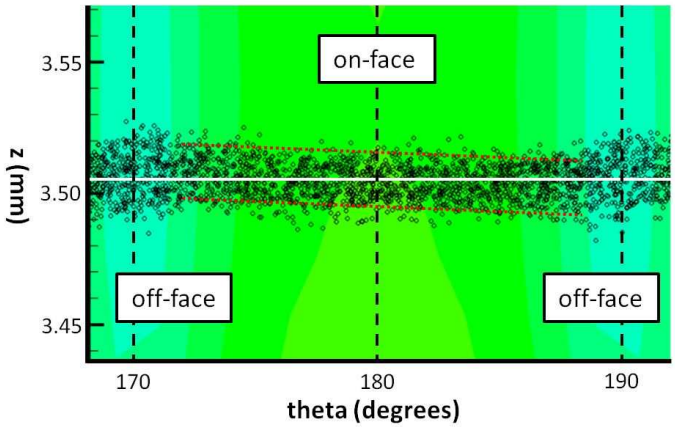

(a) Particle Loss

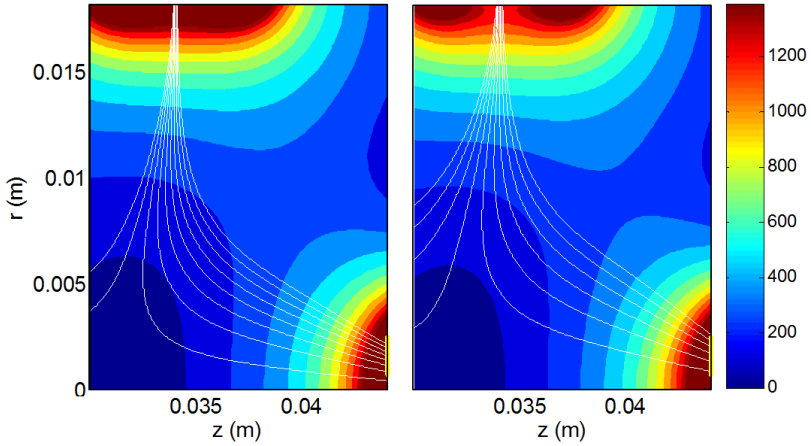

(b) Magnetic Field Lines

Figure 3.14: Computational results of the particles loss to the ring magnet (a) directly upstream of the point cusp for 18 blocks. The loss width is about twice the electron Larmor radius and traces out a slight periodic zig-zag pattern between individual each block magnets, where on-face is closest to the magnet face and off-face is the location between block magnets. The bottom figure is a magnetic field contour (Gauss) and field lines emanating from the region within the ring cusp's loss width at both the on-face (left) and off-face (right) planes.

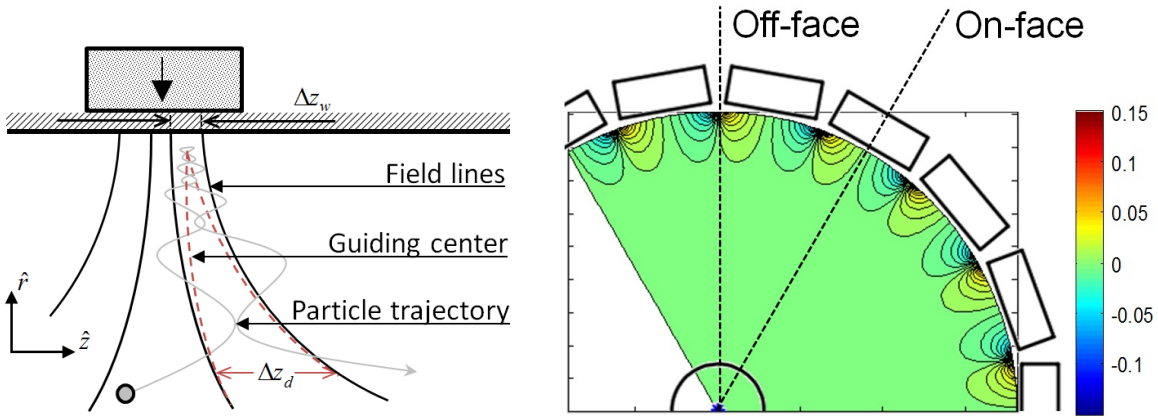

(a) Diagram **(b)** Model Results

Figure 3.15: The left figure is a diagram of the effect of an axial drift to the electron trajectory at the ring cusp as described by Eq. (3.2). Electrons incident to the cusp are reflected out on a different field line. The right figure is the results which shows the scaled axial drift (mm) contour plot of Eq. (3.2) where positive values are drifts towards the point cusp and vice versa.

electrons reflected near the ring cusp. There is a pair of forward and backward drift regions for each off-face block magnet region very near the ring cusp. At the outer edge, the contour values predict half the maximum axial displacement for electrons loss to the ring-cusp, which is consistent with the simulated results shown in figure 3.14a. Although the analysis is inaccurate near the center region where electrons are relatively unconfined, the contribution to the integral is negligible due to the scaling factor.

The overall effect of the axial drift is a slight cross-field transport of electrons that are reflected close to the ring-cusp. These same electrons will have lower magnetic moments and are less likely to be confined — thus are more likely to be lost at the subsequent point-cusp. Electrons that experience a forward axial drift will follow field lines that terminate to larger radii at the point cusp, contributing to the radially extended ridges in the loss structure. A backward axial drift causes electrons to follow field lines that pass further into the null region where their motion becomes more "non-invariant." This leads to higher loss rates of the previously confined electrons to the point-cusp, which contributes to the current density

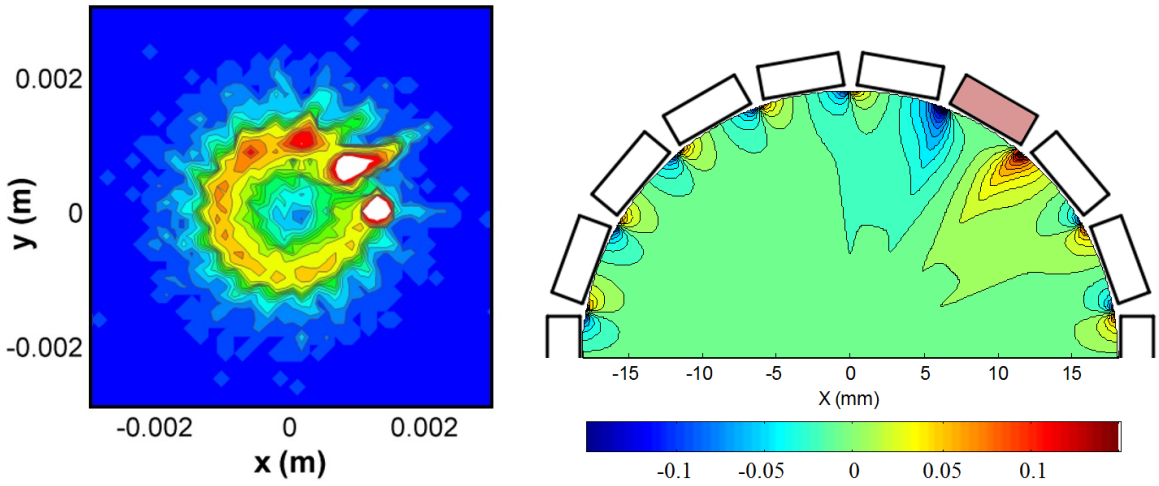

(a) Simulation model **(b)** Analytical model

Figure 3.16: The computational result (a) for 18 block magnets with the magnet in line with the positive x-axis at 75% magnetization. Results show 17 ridge structures similar to the observation in the experiment. The analytical model (b) shows a scaled axial drift contour plot (mm) of Eq. (3.2) but with a single block magnet marked in red at 75% magnetization. The result indicates a large increase of the axial drift and a missing alternating pair at the location of demagnetization.

peaks in the loss structure.

Several possible experimental inaccuracies were investigated to understand the discrepancy between the 18 blocks ring magnet and the 17 ridges measured in the experiment. The most probable explanation is a reduction in the effective magnetic field strength of one of the block magnets at the downstream ring-cusp. As simulated in figure 3.16a, a 25% reduction in the magnetic field of one of the 18 block magnets in the array can result in 17, instead of 18, ridge structures. Using the analytical description from Eq. (3.2), figure 3.16b shows that the presence of a weakened magnet will cause the region very near the magnets to essentially "skip" a pair of forward and backward drift regions near the weakened magnet, which would lead to the loss of a ridge structure at the point-cusp. In addition, the weakened magnet creates much larger drift values that also affect the surrounding cusps and could lead to greater losses at the point cusp in relation to this azimuthal position. The variation of angular separation and length of the ridge structure in the experimental data indicate a

non-uniform spacing and/or magnetization of the block magnets. This uncertainty, coupled with the possibility of a small gap between the block magnet face and the cylindrical chamber, can potentially create a magnetic field deficit that is adequate for similar behavior to the simulation result. This analysis is further evidence of the importance of the upstream field structure.

3.5 Chapter Summary

A combined experimental, computational, and analytical effort was undertaken to improve the understanding of near-surface cusp confinement for small scale discharges. Experimental measurements of the primary electron losses were taken at increasing complexity to the magnetic field upstream of the cylindrical point cusp magnet. For the cases with an imposed upstream magnetic field, the loss structure consistently exhibited an intricate collection pattern that had not been observed by other researchers. This result contrasts the supposition that cusp collection for plasma and electron discharges is primarily determined by the magnetic field strength at the cusp collection surface. From these observations, the primary electron leakage to the cusp can be strongly influenced by the upstream magnetic field structure. This is especially important for miniature scale discharges where most of the plasma volume is magnetized and small perturbations from one cusp is carried over to the following cusp instead of being loss to a low field region. Although these complex loss patterns can be described by the single particle equations of motion, they are generally not captured in many computational models as it requires both high accuracy and resolution with both the particle pushing scheme and the magnetic field evaluations.

The findings from this chapter was also observed in the spindle cusp experiments in appendix A where the plasma leak width at the point-cusp was found to be greater than at the ring-cusp despite the stronger magnetic field strength. In addition, the Axial Ring-Cusp Hybrid (ARCH) Discharge, covered in chapter 6, has two adjacent and concentric ring-cusp

elements at differing radial locations. The 2D discharge maps show that the geometric effects between the two ring-cusps led to higher plasma leak width at the inner ring-cusp.

CHAPTER 4

Analysis of an 8 cm Ring-Cusp Discharge

This chapter transitions from experiments with only primary electrons to a weakly ionized plasma inside a DC ring-cusp discharge. It was demonstrated in chapter 3 that the primary electron leak rate and structure at a cusp can be strongly influenced by the upstream magnetic fields. Furthermore, appendix A and appendix B investigated a spindle cusp discharge which indicated that the same phenomena can affect all charged species. These considerations were found to be important for miniature-scale devices where the majority of the discharge volume is magnetized and the various cusp elements are located at different radii. Therefore, the focus of this research switched towards investigating cusp-confinement at the discharge design level rather than each individual cusp element.

Mao and Wirz published the first and only full plasma structure map of a ring-cusp confined DC discharge [40]. Measurements of the plasma density, electron temperature, and plasma potential were obtained for a 3 cm ring-cusp discharge using a single Langmuir probe. The device featured three repeated and symmetric ring-cusp elements with a hollow cathode electron source. The results indicated that the plasma density distribution correlated closely to the magnetic field topology. A basic Langmuir probe analysis was used to interpret the plasma parameters which assumed a thin plasma sheath relative to the probe size and a generally non-magnetized plasma. However, the strong permanent magnets used in ring-cusp ion thrusters naturally leads to a wide variation of the plasma conditions and magnetization that can have appreciable effects on the charged particle collection. In addition, primary electrons have an important role in DC ion thrusters, particularly at the miniature scale, and obtaining an electron energy distribution function (EEDF) map would be of significant

contribution for model validation and understanding the discharge behavior.

The DC-ION discharge model, developed by Wirz [33], was benchmarked using performance data of the NSTAR ion thruster. The hybrid computational model uses a single-fluid approximation for the discharge plasma while the non-collisional primary electrons are simulated through a Monte-Carlo Collision (MCC) particle tracker. For the MiXI thruster, the model was able to predict performance results similar to those of the measured performance data. However, results of the plasma parameters and internal structure have yet to be compared to experimental data. A particle-in-cell (PIC) with MCC model, developed by Mahalingam and Menart [41], was also benchmarked using the NSTAR ion thruster. The authors also attempted to validate the computational results with plasma parameter maps but was limited to selected regions within the thruster where the data was available [42].

The Ring-Cusp Test Discharge (RCTD) presented in this chapter was developed as a multipurpose experimental platform to: (1) baseline Langmuir probe theories and probe tip orientation in a magnetized plasma, (2) accurately resolve the EEDF and primary electron density, and (3) obtain a detail discharge map of the plasma properties that can be used to validate various computational models for ion thrusters and similar discharges. Although the RCTD is not a miniature device at 8 cm in diameter, the magnetic field topology was such that most of the bulk plasma was magnetized and exhibited features that is present in chapter 5 and chapter 6. Two Langmuir probes at orthogonal orientations were used to obtain two sets of plasma parameter maps which includes: the plasma density, primary electron density, electron temperature, and the plasma potential. The discharge mapping approach developed in the chapter was used to characterize the discharge plasma of various miniature ion thruster configurations in the following chapters. The primary electron maps are then compared to computation model results, developed in appendix B and modified for this experiment.

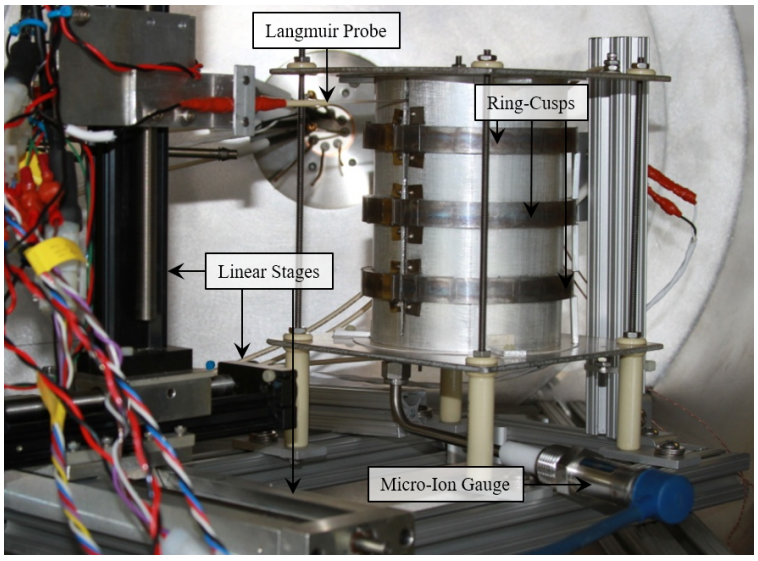

Figure 4.1: Image of the Ring-Cusp Test Discharge (RTCD). The Langmuir probe is mounted onto linear stages and accessed the discharge through a slit along the z-axis of the cylindrical wall.

4.1 Approach

The Ring-Cusp Test Discharge was a simple 8 cm DC discharge with 3 ring-cusp elements similar to the 3 cm device developed by Mao and Wirz [40]. The RCTD was made larger to acquire higher spatial resolution with the Langmuir probe measurements. This section will begin with a description of the experimental setup, including the RCTD design, probes, and the data acquisition system. A basic review of the probe theory will be provided along with a description of the computational model. Note: the plasma potential, V_p, from this chapter onwards will now be defined relative to the discharge cathode potential.

4.1.1 Experimental Setup

The RCTD experiment was conducted in the same Micro-Propulsion facility as the electron dynamics experiment. The device, as diagrammed in figure 4.2, was an 8 cm inner diameter by 14 cm length aluminum discharge chamber. The magnetic field topology was generated with three evenly spaced ring-magnet elements placed in alternating polarity.

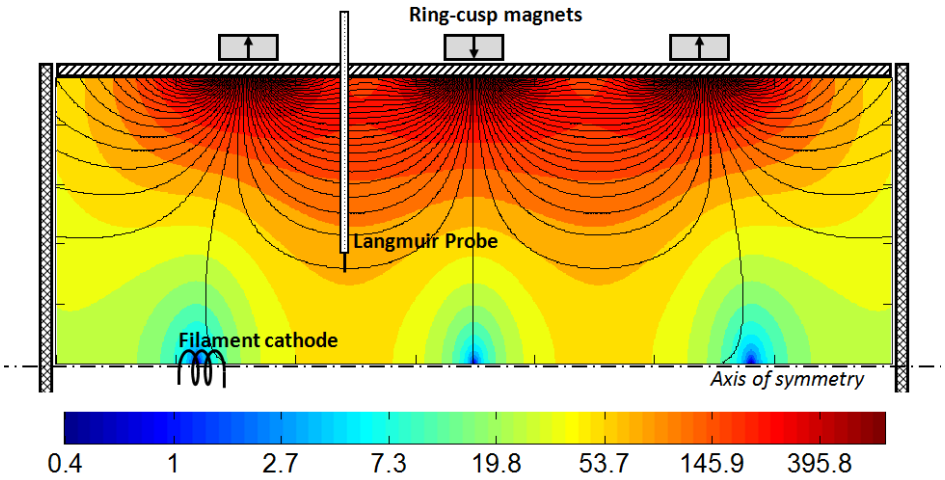

Figure 4.2: Diagram of the RCTD with the magnetic field lines and contour (in logarithmic scale) overlaid. The filament was mounted to the left (upstream) null region and discharge plasma diffused right-ward (downstream) towards the right null region.

Similar to the multi-cusp electron experiment, the ring-magnets were comprised of discrete samarium cobalt block magnets. Neutral gas was introduced through back filling of the entire vacuum chamber rather than using an internal plenum injector. This approach allowed the internal neutral gas density to be measured directly with an ion gauge rather than through calculations based on the flow rate and total open area. An additional micro-ion gauge was used to verify the internal neutral gas density.

As shown in figure 4.2, probe measurements were conducted through the 2.5 mm wide, vertical access slot that spanned almost the entire chamber length. The radial access of the probe allowed for measurements around the cathode source and therefore, an entire azimuthal slice of the discharge chamber. The probes were mounted onto a 3-axis linear stage system with the third stage used to switch between the two probes. Each ring-cusp was comprised of fifteen $0.5 \times 0.5 \times 0.2$ inch block magnets that were held in place by a thin iron strip that was secured on each side of the probe slot. There was an even 2 mm gap between each block magnet that was necessary for the probe access. The cathode source was a 5 mil tungsten wire, coiled and mounted onto a 2.5 mm diameter double-bore ceramic tube from the opposite side of the probe slot. The tube was supported at a diagonal angle relative to

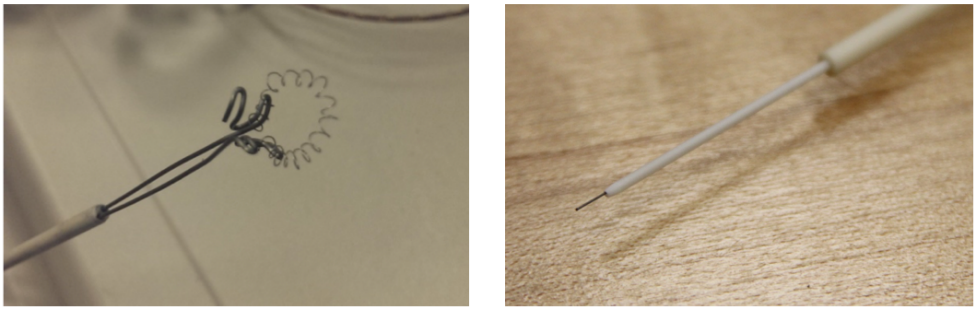

Figure 4.3: Images of the discharge cathode filament (left) and the Langmuir probe (right).

ring-cusps to reduce plasma impingement by the ceramic tube. For higher discharge currents, two filaments were connected in parallel to reduce the filament length and the heater voltage. Each filament was typically heated to under ∼2.4 A and ∼12 V to prevent rapid evaporation.

The dimension of the discharge chamber was designed the balance the trade-off between probing resolution and maintaining a desired cusp magnetic field topology similar to miniature ring-cusp discharges. The magnetic field was configured to generate a repeating cusp domain with three distinct null regions separated by virtual point-cusps. This allowed for investigation into the transport of plasma and primary electrons across each null point and through the point cusps. The Langmuir probe dimension was limited to the available construction materials and the 8 cm diameter allowed for adequate spatial resolution of the cusp structure relative to the size of the probe tip. On the other hand, the diameter also was small enough to generate a point-cusp field of ∼100 Gauss while maintaining a ring-cusp field of ∼1.2 kGauss.

Figure 4.3 shows the radially oriented Langmuir probes (r-probe) used to measure the EEDF and plasma properties. They were both constructed with a 3.2 mm length by 0.4 mm diameter tungsten wire protruding from a 2.4 mm diameter alumina tube. The high aspect ratio reduces the contribution of currents collected at the probe tip and increases the plasma density range in which the cylindrical Langmuir probe theory is valid. The Langmuir probes did not measurably disturb the discharge plasma except when probe tip was very close to the cathode filament while at a bias higher than the discharge voltage; this region is avoided in

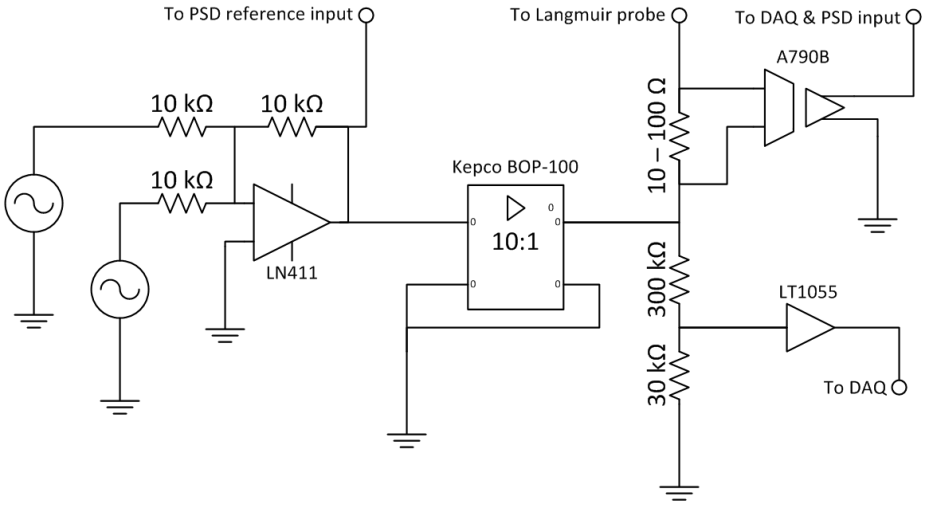

Figure 4.4: Circuit diagram for operation and measurements of a Langmuir probe including a summing amplifier circuit for measuring the EEDF.

the measurements. As shown in figure 4.1, the two probes were mounted with a large lateral offset which allowed for an identical scan pattern that maximizes the measurable domain.

The Langmuir probe circuit is diagrammed in figure 4.4, where the circuit left and right of the Kepco were for signal generation and measurement, respectively. Triangle waves were used to bias the probes instead of a sinusoidal function to reduce the time in which probe was biased above the plasma potential. The TI LF411 op-amp was configured as a summing amplifier that could be used to superimpose a higher frequency, lower amplitude sinusoidal signal onto the base triangle waves. The harmonic response in the probe current could be analyzed using a lock-in amplifier to directly interpret the derivatives of the signal. The Kepco BOP-100 is a 10:1 bipolar operational amplifier that directly supplied the probe voltage; the values of which were measured with a voltage divider and a unity gain buffer. The probe current was measured using a shunt resistor on the high side of the circuit to avoid leakage current from the voltage divider and power supply. Hence, the Avago ACPL-790B optically isolated amplifier was required to differentially measure the voltage across the shunt. The voltage range was set to a maximum of $\sim$5 V above the maximum plasma potential within the discharge and a minimum of approximately -50 V to capture the ion

saturation curve. The probe movements and discharge conditions were actively monitored for thermal drifts throughout the mapping process.

4.1.2 Probe Theory

The Langmuir probe measurements were analyzed using probe theories to account for the small probe size and with consideration of the magnetic fields. A total of 400 I-V curves, each with 500 sample points, were binned and averaged to reduce the noise from the plasma and electronics. An adaptive smoothing cubic spline was used to fit the raw data and calculate the first and second derivative. Care was given to minimize the smoothing in the electron retarding region to prevent flattening of the derivative peaks. Druyvesteyn showed the electron energy distribution function (EDDF) can be extracted from the second derivative of the $I - V$ characteristics [43]:

$$F_e(\varepsilon) = \frac{2}{A_p e^2}\sqrt{\frac{2m\varepsilon}{e}}\frac{d^2 I_e}{dV^2}; \tag{4.1}$$

where A_p is the total area of the probe and ε is the energy in eV which corresponds to the probe's voltage with respect to the plasma potential, i.e. $\varepsilon = V_p - V$. The electron density can then be calculated by integrating $F_e(\varepsilon)$ across the entire energy spectrum:

$$n = \int_0^\infty F(\varepsilon)d\varepsilon. \tag{4.2}$$

The electron repelling region of the standard current-voltage $I - V$ curve can be considerably altered by local magnetic fields, especially near the plasma potential. The electron cross-field transport is inhibited by the magnetic field which diminishes the electron saturation currents and broadens the exponential region. The effect is more significant when the probe orientation is parallel to the field lines. There are two main assumptions for using the Druyvesteyn formula to calculate the EEDF that are of concern:

1. The plasma entering the probe sheath has an isotropic distribution. This condition is likely satisfied for the highly collisional plasma electrons regardless of the magnetic fields. The non-collision primary electrons could be isotopic within the null regions but their velocity distribution become increasingly skewed towards the cusp structures due to the adiabatic invariance.

2. The motion of the electrons once it enters the sheath is uninhibited (ie. its mean free path is much greater than the sheath thickness). This is satisfied in terms of electron-neutral collisions as ion thruster discharges typically operate at relatively low gas pressures. However, the Larmor radii for a considerable fraction of the plasma electrons near the cusp can approach the size of the probe and sheath. The higher energy primaries are relatively unaffected by this interaction.

The second derivative data (ie. the EEDF) was used to calculate the electron temperature using a Maxwellian fit in the region towards the floating point potential. The region near the plasma potential is avoided as the low energy electrons are more affected by the magnetic fields. The primary electron population alters the entire electron-retarding region of the $I-V$ curve and fitting a Maxwellian curve directly to the data will tend to overpredict the electron temperature. The two electron populations are distinguishable in the extracted EEDF and the Maxwellian can be fitted to just the plasma electron population. The primary electron EDF is calculated by subtracting out a fitted Maxwellian curve for the plasma electron from the total EEDF:

$$F_p(\varepsilon) = F_e(\varepsilon) - F_M(\varepsilon). \tag{4.3}$$

The Larmor radii of the primaries were much larger than the probe diameter throughout the discharge domain with the possible exception very near the ring-cusps. Therefore, the primary electron density was calculated by integrating the primary EEDF using Eq. (4.2). The plasma potential was estimated to be at the maximum first derivative of the $I-V$ curve. The magnetic field will lead to a systematic under-prediction of the true value depending

on the field strength. A kinetic probe theory is required to more accurately calculate the plasma potential [44] from the $I - V$ curve.

The Bernstein-Rabinowitz-Laframboise (BRL) theory was used to calculate the plasma density which accounts for the effects of sheath expansion and ion orbital motion [45] for small diameter probes. It is more reliable to interpret the plasma density from the ion saturation curve because the heavy ions species remain unmagnetized. Although it has been shown that a strong magnetic field can deform the ion collection sheath [46, 47], this behavior was not observed in the data presented in this thesis.

Chen has compared BRL with orbital motion limited (OML) and Allen-Boyd-Reynolds (ABR) theories using a laboratory RF plasma and concluded that the BRL analysis can overpredict the plasma density by up to a factor of three in denser plasmas [48]. However, his RF plasma had high background pressure ($\sim$15 mTORR) which would have resulted in a collisional sheath. The scattering and CEX collisions would destroy the orbital motion, leading to an over-prediction of the ion density. Crowley et al. compared the same theories as Chen but in a higher density plasma ($\sim 10^{18}$ m^{-3}), lower background pressure (2.3 mTorr), and with the inclusion of the Boyd-Twiddy (BT) method [49]. The values for the OML and BT method was in close agreement to the BRL method while the values for the ABR method was nearly a quarter of the other ion collection methods.

4.1.3 Computational Model

A fluid computational model was previously developed in appendix B to investigate a spindle cusp plasma in appendix A. This model solved the diffusion equation on a magnetic field align (MFA) mesh. The plasma generation was approximated from the primary electron density which was independently determined from a Monte-Carlo collision (MCC) particle pusher. The model was slightly modified from appendix B to simulate the RCTD in order to roughly validate the experimental data and key components of the DC-ION model or other fluid models. In particular, the merits of using a MFA mesh to resolve the cusp structure and

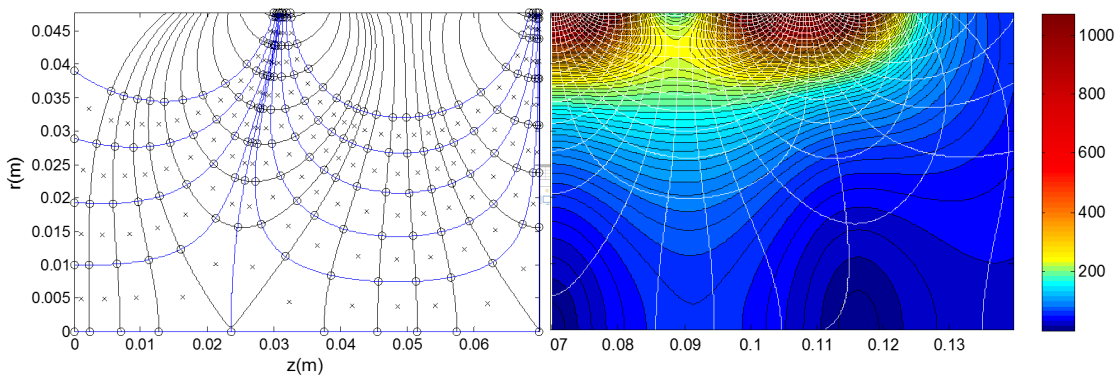

Figure 4.5: Computation domain of the RCTD showing a low-resolution sample of the stitched MFA mesh (left side) and the magnetic fields (right side).

the independent treatment of the primary electrons. More details can be found in appendix B but it is important to reiterate that this model is not rigorous nor self-consistent. The energy equation is not solved and the electron temperature profile from the experimental data was used in part to calculate the diffusion coefficient.

The structured MFA mesh generation described in appendix B.1.3 can only be implemented to a limited range of geometries. It was simple to mesh a spindle cusp geometry because of the highly symmetric magnetic fields and plasma generation. The RCTD field topology has 3 distinct ring-cusps and the primary electrons were injected into only a single null region at the edge of the device. In order to capture the full discharge domain with the rigid mesh generator, a total of 4 individual mesh was stitched together. A low resolution sample mesh is shown in figure 4.5 where the lines along the center of the ring-cusp separates each mesh domain. The system of equations was modified accordingly for the new boundary conditions and a sparse matrix was generated that includes all four domains.

The MFA mesh does not provide sufficient resolution to spatially resolve the primary electron density — they are confined closer to the center-line where grid cells were the largest. Although the generation rates were still calculated based on resident time in the MFA mesh, the visualized primary electron density contours used a traditional Cartesian mesh at much higher resolution. Excitation collisions and thermalization had also since

been implemented; the primary electron density values are now directly calculated based on the discharge current and are not scaled to experimental data.

4.2 Experimental Results

The discharge mapping data was acquired for a 26 V, 1.3 A discharge with a neutral density of approximately 9×10^{18} m^{-3}. The wall on the left axial end was biased to cathode potential to confine the primary electrons and collect the ion current. The discharge current was controlled by adjusting the filament cathode heater power with the discharge voltage was kept constant. Measurements between the two probe orientations were taken back-to-back while the discharge conditions remained essentially constant.

4.2.1 Langmuir Probe Analysis and Orientation Comparison

The final $I - V$ curve was an average of multiple fast voltage sweeps rather than a continuous time-averaged voltage ramp. This reduced the duration in which the probe was biased above the plasma potential to prevent overheating of the probe tip. A portion of the Langmuir probe's current and voltage data is shown in figure 4.6, measured at an arbitrary location. Although not visible in the presented data, there was a vertical offset in the current data between the upward and downward voltage sweep due to capacitance in the diagnostic circuit. This systematic error was nullified when the upward and downward data were averaged because of the symmetry of the triangular voltage sweeps.

The four plots shown in figure 4.7 are sample Langmuir probe data and analysis at an arbitrary location. The top right plot shows the standard $I - V$ trace in a semi-log plot along with the calculated first and second derivative. From visual inspection, the standard $I - V$ sweep would yield a slightly higher electron temperature than that from the derivative curves. In addition, a higher energy electron population can be detected in the second derivative data by the kink in the curve at the higher energies. The bottom left figure shows

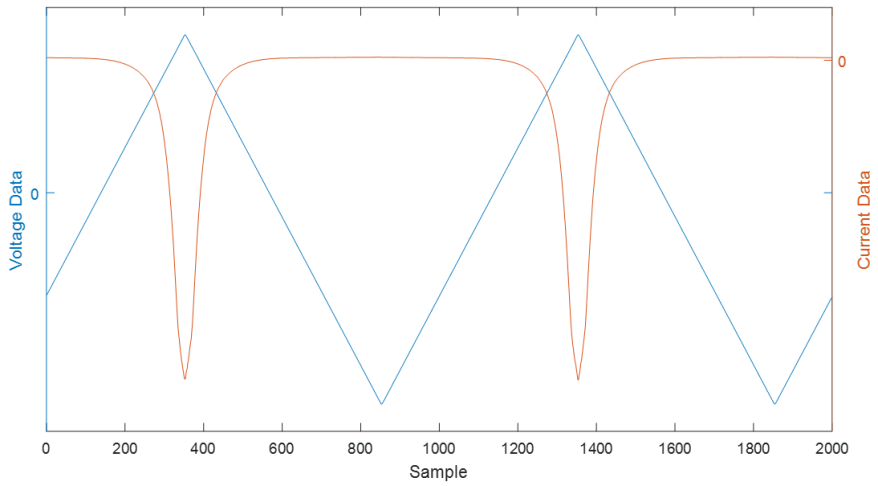

Figure 4.6: Sample raw voltage and current data of the Langmuir probe sweeps. The full dataset includes 200 traces at each spatial location. Data shown here was within the bulk plasma where there was a strong signal and low noise.

the process in calculating the primary electron density. The primary electron population is defined as the difference between the full population and Maxwellian estimate for the plasma electrons. Although the Maxwellian fit may not match the data well at lower energies due to the magnetic field, the higher energy electrons are less confined. The plasma density from electron collection is found from integrating the entire EEDF curve. The bottom right plot shows the ion saturation fit using the BRL theory which iterates to a plasma density based on the sheath size.

Figure 4.8 shows the EEDF curve from the radial Langmuir probe at two distinct location within the discharge. Figure 4.8a was measured within the center null region while figure 4.8b was measured within the inter-cusp region and away from the center-line. Contrasting the two probe data, there is a distinct hump in figure 4.8a at the higher energy region, representing the primary electron population, which is absent in the other figure 4.8b. This is an expected outcome because the primary electrons were injected to the centerline and are en massse, non-collisional, and cannot diffuse far across the field lines.

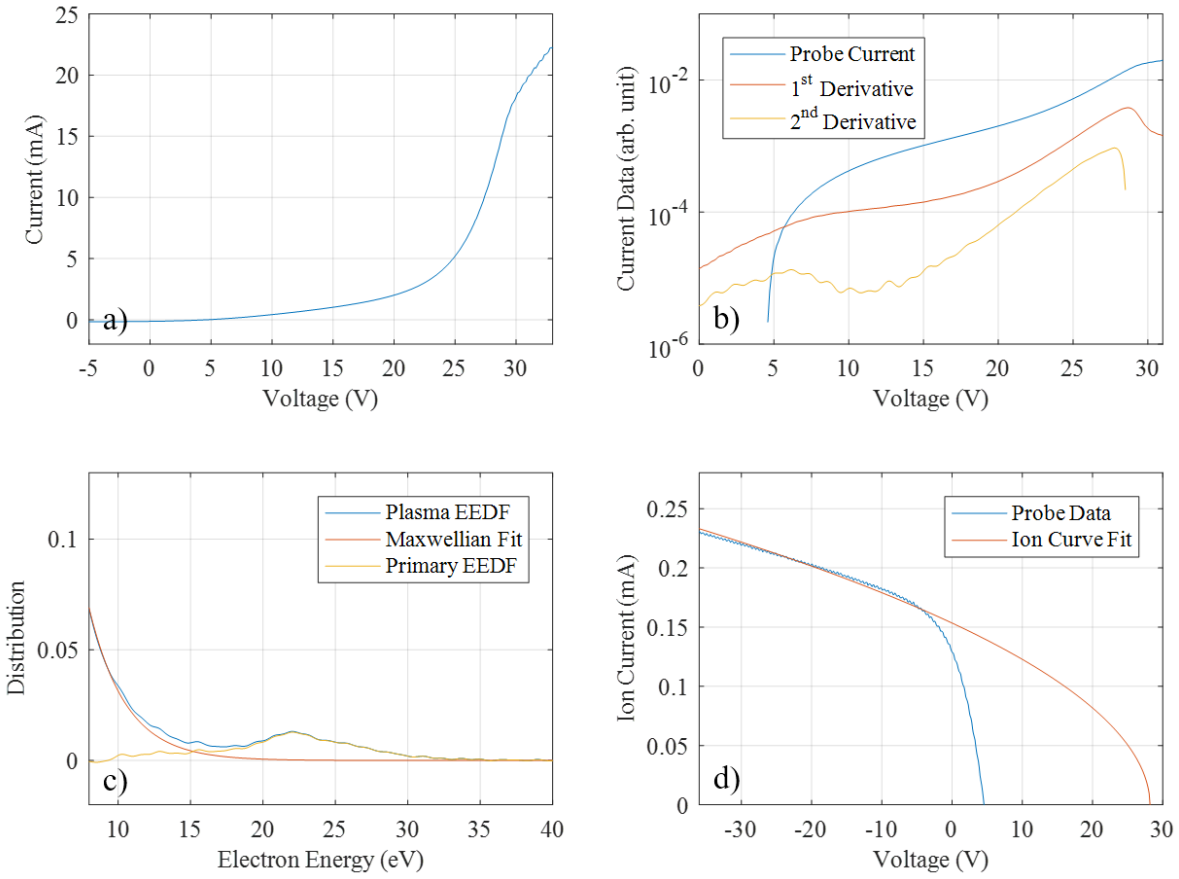

Figure 4.7: Example Langmuir probe data and analysis. (a) The binned, then averaged I-V sweep. (b) The probe sweep and it's derivative plotted in a semi-log scale. (c) Extraction of the primary electron density through subtraction of a Maxwellian plasma electron population. (d) The ion saturation curve fitted using the BRL method.

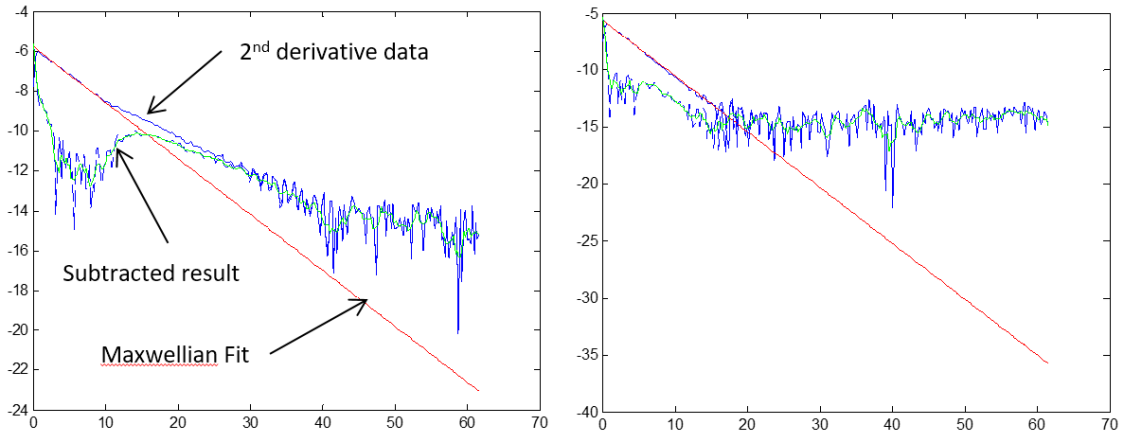

Figure 4.8: Sample EEDF data highlighting the primary electron population at two locations within the RCTD.

4.2.1.1 Plasma Density

The plasma density maps in figure 4.9 show that the plasma structure correlates closely to the magnetic field structure shown in figure 4.2. The plasma was essentially unconfined at either ends of the discharge chamber where the magnetic field strength is less than 20 Gauss. The ions were extracted by the cathode-biased end wall and the plasma density is shown to decrease along the presheath structure as the ions were accelerated to the Bohm velocity. In between each of the subsequent ring-cusps, the plasma density appears to drop across each null region and point-cusp. Figure 4.10 will show that the primary electron density decreases across each point-cusp as a fraction of the population reflected back upstream. There were less ions generated towards the right hand side and the center ring-cusp structure is skewed towards the left hand side.

Figure 4.9 is a comparison between the plasma density obtained from either the ion or electron population. The most apparent difference is that the global plasma densities from the BRL method is about a factor of 2 greater than those obtain using the Druyvesteyn method. Although the electron collection is easily inhibited by magnetic fields, the difference in densities between the two method is consistent even in the null region. The findings are similar to those previously mentioned by Crowley [49], where the plasma density predicted

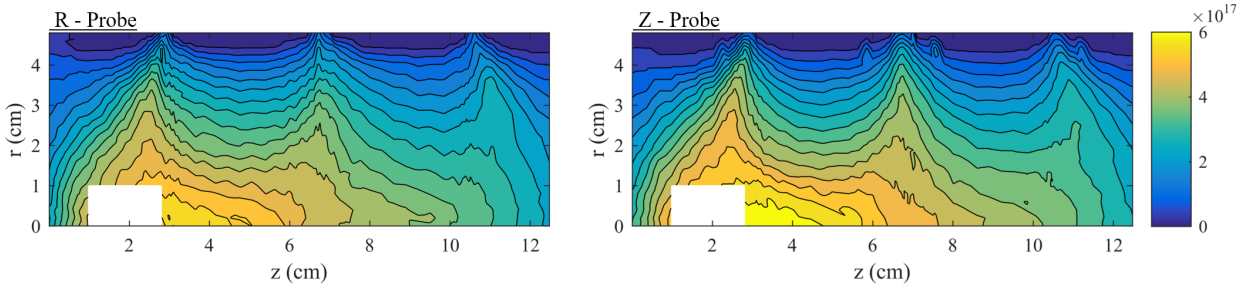

(a) Plasma density (m^{-3}) from BRL

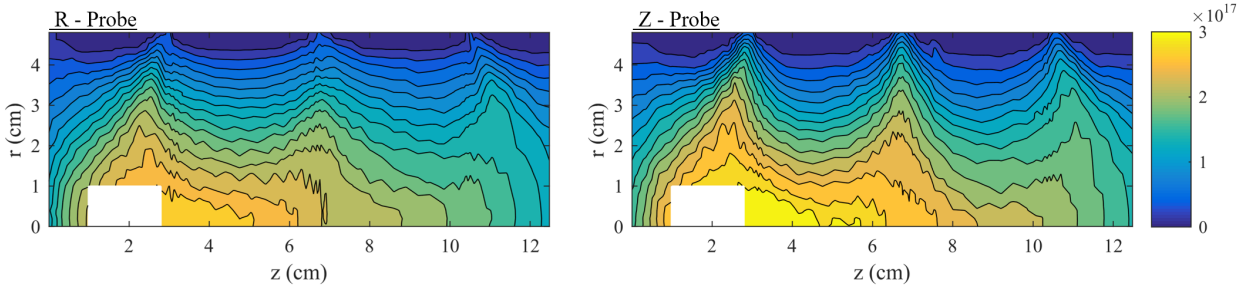

(b) Plasma density (m^{-3}) from Druyvesteyn

Figure 4.9: Comparison of the plasma density values obtained from different probe theories and orientation of the probe tip relative to the magnetic field.

by the Druyvesteyn methods was half of the BRL method. The results from this thesis, presented in chapters 5 and 6, show better agreement with the BRL method. The integrated Bohm current based on plasma density maps from the BRL method was in close agreement to the measured total ion current collected at the chamber walls.

Figure 4.9a shows that the results from the axially and radially oriented probes are in close agreement throughout most of the discharge. The largest discrepancy is at the center ring-cusp where there is a more pronounced cusp structure with the r-probe. The 0.25 mm diameter probe was moved at 1.0 mm increment within this region while the hybrid leak width ranges from 4 mm to 0.4 mm between $r = 2.5$ cm and the cylindrical wall, respectively. It is possible that the r-probe partially or completely skipped over the small region of maximum plasma density in the cusp. This is supported by inspecting the other two ring-cusps where the cusp magnetic fields are not completely parallel to the r-probe. Here, the difference between the two probe orientations are less obvious. On the other hand, the 3 mm long z-probe is perpendicular to the center cusp, which would tend to smear out the width of the cusp structure, especially near the wall.

Shown in Figure 4.9b, the electron collection is more sensitive to the probe orientation relatives to the magnetic field. The two results are very similar within the inner half of the discharge chamber where the magnetic fields are weak. Aside from the absolute values, the plasma structures measured with the z-probe are nearly identical between the Druyvesteyn and BRL methods. However, the r-probe using the Druyvesteyn method was unable to resolve the cusp structure at higher magnetic fields. All three ring-cusp structures are less defined toward the outer half of the domain and the center ring-cusp is almost ambiguous. The magnetic fields strongly inhibit the electron collection when the probe was in a near parallel orientation, especially the lower-energy electrons that constitute the majority of the population.

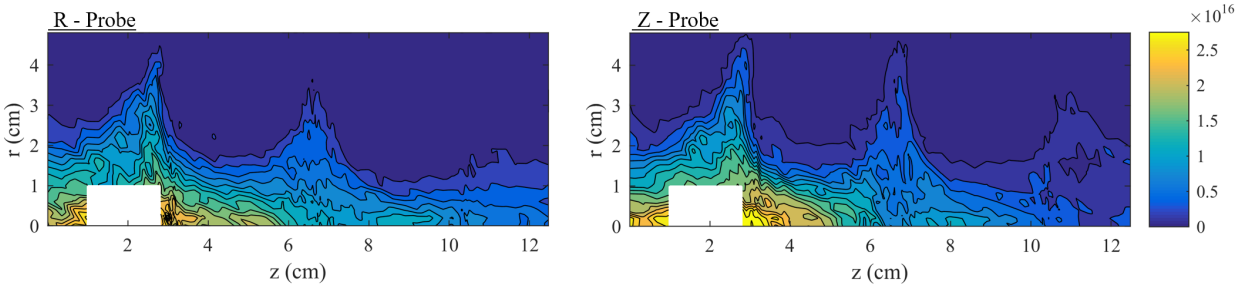

Figure 4.10: Comparison of the primary electron density values obtained from two Lanmguir probes at orthogonal orientation.

4.2.1.2 Primary Electron Density

Figure 4.10 shows the primary electron density comparison between the two probe orientations. The overall contours roughly resemble a skeletal structure of the plasma electron contour. The primary density is approximately 3–5% of the plasma electron density which is normal for the given discharge condition and in a device with sufficient confinement. As previously discussed, the primary electron density drops across each side of the point-cusps due to magnetic mirroring. However, there appears to be a local maximum of the primary electron density at the point-cusps, particularly between the center and right ring-cusps. This is caused by a funneling effect into the cusp and the same characteristic will also appear in the computational model in section 4.2.2.

The Druyvesteyn integration of the EEDF assumes that the population is isotropic which is only true for primary electrons in the null region. Since primaries are non-collisional, the trajectories of those that enter either the ring or point-cusps becomes be adiabatically invariant. The ratio of the velocity distribution perpendicular to the magnetic field increases further into the cusp. Furthermore, the primary electrons were injected only into the left side of the domain and thus there was a net flow of primaries rightward. Thus, the primary population that were able to cross the point-cusps initially had a low magnetic moment entering the cusp and thus, had a parallel bias in its velocity distribution as it exited on the other side. This parallel bias would also be preserved as the primaries cross the subsequent

null region into the next point-cusp.

The difference between the primary electron density profile of each probe along the center-line region reflects the discussed analysis. A velocity distribution biased in the direction of the probe would effectively inhibit primary electron collection and thus, an underestimation of the actual density. Therefore, the z-probe measured a higher plasma density compared to the r-probe at the upstream side of each point-cusp. The opposite trend is seen downstream of each point-cusp where the z-probe primary density rapidly drops. Although the point-cusp reflected the primary electrons with higher magnetic moment, the parallel bias only appears as they exited the point-cusp and the field strength decreases. Therefore, the z-probe data shows an unusually deficiency at the null region of both the center and right ring-cusps. Furthermore, the r-probe data shows a much smaller decrease to the primary electron density across the right side point-cusp than the left side point cusp. A higher fraction of the primary electrons that entered the right side point-cusp partially maintained their low magnetic moment as they exited the left side point cusp and shot straight across the null region.

4.2.1.3 Electron Temperature

Figure 4.11 is a comparison of the electron temperatures interpreted from either the non-derivative $I-V$ data (I) and the second derivative (I''). The electron temperature contour is delineated along the magnetic field lines which imposes a strong anisotropic electron mobility. The bulk electron temperature values are consistent with the discharge conditions in which the bulk plasma is 4–6% ionized. The overall contour maps from the non-derivative data is much smoother due to the inherent noise amplification of calculating the second derivative. Excluding the region where the primary electrons reside, the electron temperature values and structure are very similar between two methods. The high-energy primary electrons will generally skew the $I-V$ data towards a higher electron temperature values. The two electron populations are more distinguishable in the EEDF data as a result of the collection

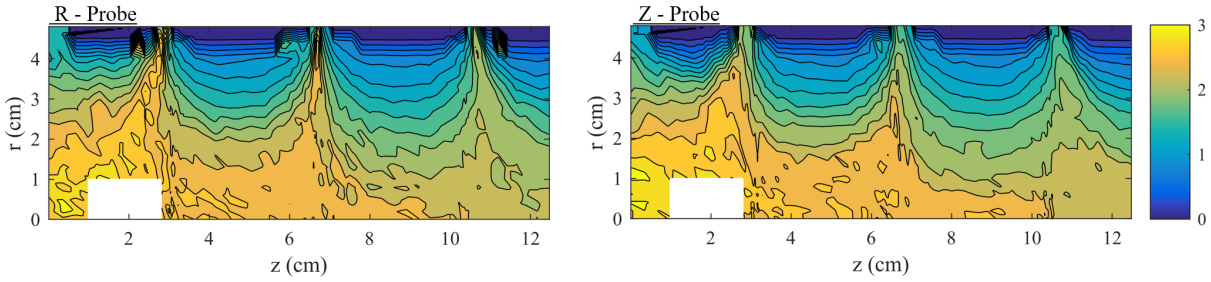

(a) Electron temperature (eV) from raw data

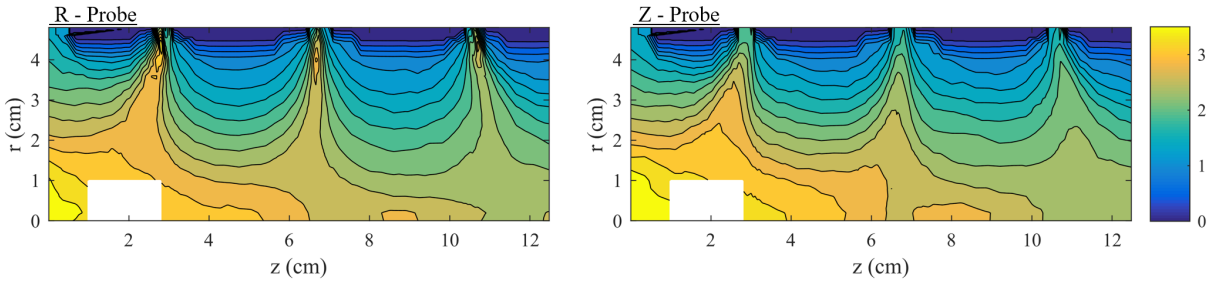

(b) Electron temperature (eV) from 2nd derivative

Figure 4.11: Comparison of the electron temperature values obtained from different probe analysis and orientation of the probe tip relative to the magnetic field.

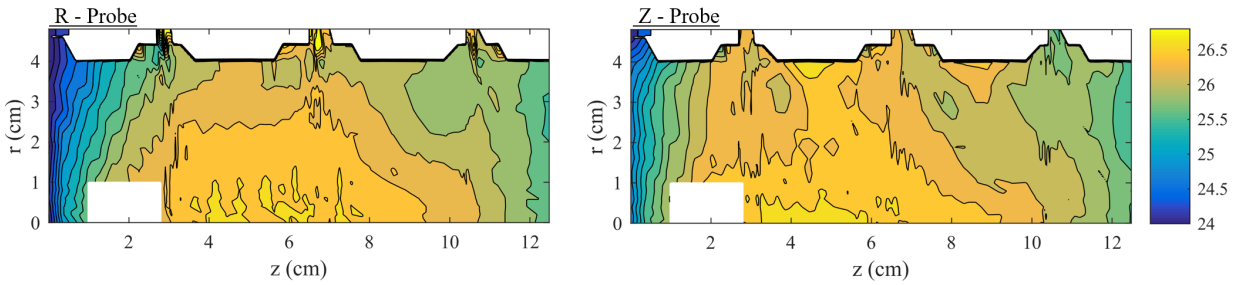

Figure 4.12: Comparison of the plasma potential values obtain from different probe orientation of the probe tip relative to the magnetic field.

mechanism of the Langmuir probe.

Comparing the probe orientation, there is clearly a smearing effect in the z-probe data towards the ring-cusps as the probe extends across isothermal lines. On the other hand, the electron temperature of the r-probe is elevated very near the ring-cusp and local temperature peaks are unlikely to be physical. As previously discussed, the strong magnetic fields inhibit the collection of electrons to the r-probe which would have the effect of widening the EEDF since a higher probe bias is required to collect/repel the electrons.

4.2.1.4 Plasma Potential

Figure 4.12 shows that the average plasma potential of the bulk plasma is near the discharge voltage. The data appears to be noisy because of the small value range of the contour maps. Approaching the left side wall, the data shows the existence of the presheath structure where the plasma potential decreases by about half the electron temperature in order to accelerate the ions to the Bohm speed. The same structure is not visible on the other side because the measurement domain does not reach the right side wall. Nonetheless, the data show a gradual decrease in the plasma potential downstream of the center ring-cusp. The primary electron map indicates that most of the plasma is generated at the left and center ring-cusps. The electrons have high mobility along the magnetic field lines and the potential structure appears to follow the Boltzmann relation.

Although the change is very small and possibly negligible, the plasma potential is seen to slightly drop and then rise again approaching the inter-cusp region. The same potential structure is also present in the MiXI thruster's discharge map in figure 5.12 and was also observed by Mao and Wirz [40]. It is speculated that the cross-field diffusion coefficient of electrons near the center of the cusp is greater than the ion's despite the magnetic confinement. The initially plasma potential decreases in order to extract the ions to maintain quasi-neutrality within the region. However, the electron temperature rapidly decreases across the field lines while the field strength increases, decreasing the electron's diffusion

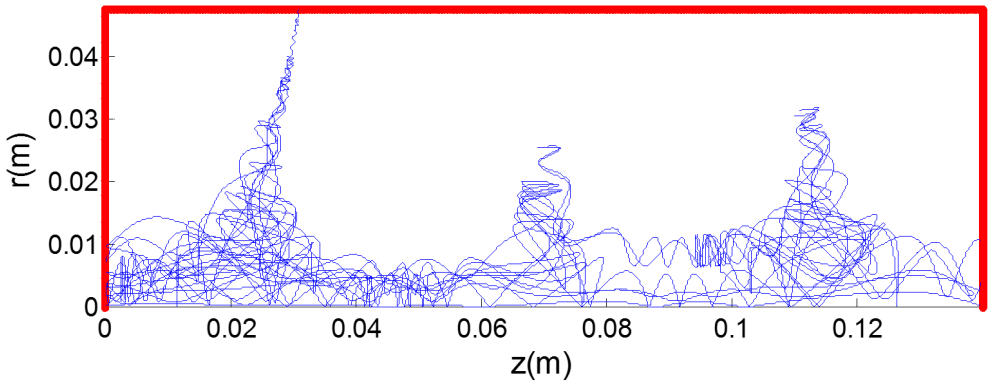

Figure 4.13: Sample primary electron trajectory inside the RCTD. Particles in the cusps have a perpendicular-biased velocity distribution and the point-cusp filters out particles with high magnetic moment.

rate. Thus, the plasma potential rises in order to reflect the ions that were initially heading towards the chamber walls. Therefore, the shape of described plasma potential structure is seen to follow that shape of the magnetic field lines.

4.2.2 Model Comparison

A total of 3000 super-particles representing a discharge current of 1.3 A were tracked to obtain the primary electron density result shown in figure 4.14. They were injected at random velocities and locations within a 1 cm diameter sphere within the left-side null region. The energy spectrum was also randomized between 15 to 25 eV to account for the voltage drop across the filament. The experimental data for the plasma densities and electron temperatures was used to determine the various collision cross-sections. The sheath potential is not considered and all primary electrons incident to the cylindrical wall were assumed to be loss. The plasma potential data suggest that the sheath potential was approximately 1 to 1.5 V and thus the associated error is assumed to be small.

A few sample trajectories of the primary electrons are shown in figure 4.13. Many of the primaries can be seen undergoing magnetic mirroring at the left and center ring-cusps. Their parallel velocity continues to decrease until they are ultimately reflected. This leads

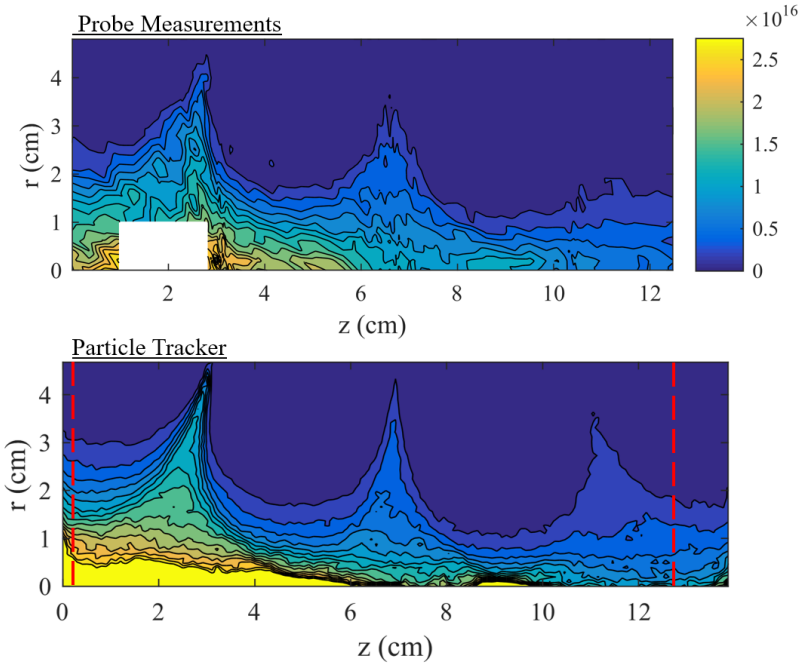

Figure 4.14: Comparison of the primary density values (both on the same scale) obtained from the r-probe measurements and the MCC particle pusher result.

to a longer residence time in the cusp structure which increases the local primary electron density as shown in figure 4.14. The sample trajectories also show that the primaries that crosses the point-cusp has a parallel biased velocity distribution that is preserved through the subsequent null region. These results support the analysis from section 4.2.1.2 for the discrepancy between two probe orientations.

Figure 4.14 is a comparison of the primary electron densities obtained from the r-probe and the MCC particle pusher results. The overall density values are very similar aside from the center-line region near the location of the discharge cathode filament. The disparity in this region is likely due to the perfect center-line alignment of the filament and the cylindrical coordinate system. Near the ring-cusp, the z-probe measurements show better agreement with the model since it is better able resolve the perpendicular-biased population. Both the model and the probe measurements are able to resolve the primary electron behavior in the RCTD: (1) the primary electron density peaks at the point-cusp as a result of the funnel

effect of the cusp structure and the reduced parallel velocity which increases the residence time of the primaries and (2) the transport of primary electrons across the RCTD as they leak across the point-cusps and diffuse across the null regions.

4.3 Chapter Summary

This chapter has developed an 8 cm ring-cusp discharge that was successfully used to baseline the discharge mapping methodology and probe analysis in a cusp magnetic field. It was found that the plasma density interpreted from the ion saturation region of the $I-V$ curve is not considerably affected by the < 900 G fields in the RCTD. However, any plasma parameters interpreted from electron collection can be strongly affected by the magnetic field strength and orientation. In addition, the plasma electron temperature interpreted from the standard $I-V$ is also elevated by the presence of primary electrons. These two populations can be distinguish through analyzing the EEDF data by taking the second derivative of the $I-V$ curve. The primary electron density can also be obtained from the EEDF data — the results of which suggest that the magnetic field does not directly inhibits their collection though confinement, but rather by altering their velocity distribution function (VDF). This work provides the first strong experimental evidence that the primary electron behavior can be treated independently in a DC ring-cusp discharge. Their non-isotropic VDF throughout the discharge, which appears to be in keeping with behaviors of single-particle trajectories, is only possible if the population is essentially non-collisional.

The results from this chapter was helpful in understanding the limitations of Langmuir probes in a magnetized plasma for the subsequent chapters where measurements were obtained for only a single probe orientation. In particular, discharge maps of the Axial Ring-Cusp Hybrid (ARCH) discharge in chapter 6 show unusually high electron temperature values near the cusp that can be attributed to the shortcomings probe orientation and theory used for the analyses.

CHAPTER 5

Plasma and Performance Characterization of Miniature Ring-Cusp DC Discharges

In this chapter, the discharge mapping technique form chapter 4 was used as a tool to investigate the plasma behavior of various miniature ring-cusp ion thruster designs with the intention of optimizing the performance. Ring-cusp ion thrusters typically use samarium cobalt permanent magnets to produce strong and relatively short-ranged magnetic fields for efficient confinement of the discharge plasma. Placed in alternating polarity, these magnets provide strong cusp boundaries near the walls to confine the plasma while the bulk plasma remains effectively unmagnetized, ideal for uniform plasma generation and beam flatness. The cusp magnetic fields can be treated as boundary-only effects. Most design efforts of conventional scale ring-cusp ion thrusters have relied on analytical models [50, 15, 27] and semi-empirical treatment of cusp confinement physics [20, 21]. For example, plasma losses to the cusp are estimated using the semi-empirical hybrid leak width and concepts such as the "highest closed magnetic field contour" are used as a design figure-of-merit and for discharge models [15, 33, 29]. This approach has worked well for larger ion thrusters; however, at the miniature scale, these design principles become difficult to implement as the cusp fields can no longer be estimated as almost entirely at the discharge boundary. In fact, the ring cusps produce complex and strong B-field structures that dominate most of the chamber volume.

Since conventional DC ring-cusp ion thrusters already have the highest efficiencies of any well-developed electric propulsion technology, there have been little motivation to map the internal plasma. To date, only a handful of authors have attempted to acquire a partial or full

map of the plasma structure within an ion thruster's discharge chamber. Many researchers have used various probes to measure the plasma properties at sparse locations to characterize the overall performance. Herman and Gallimore [51] partially mapped the plasma parameters as well as generated EEDF curves inside the 30 cm NSTAR ion thruster in the region near the hollow cathode and the grid system. Hubble, et al. obtained a detailed electron spatial distribution map of an inverted cusp structure with a helium afterglow plasma using laser collisional induced florescence (LCIF) [52]. Tsukizaki, et al. [53] used both Langmuir and optical probes through the grid system to measure a coarse plasma parameter map of the -10 ECR ion thruster. Previous to this work, Mao and Wirz [40] provided the only effort to fully map a miniature (3 cm) ring-cusp discharge and the results showed a highly structured and non-uniform plasma density contours. However, the discharge was not designed as an ion thruster and their results did not include an EEDF map. Previous to this work, a full plasma parameter or EEDF map of a ring-cusp discharge has not been obtained. These results are crucial to resolving the primary electron population within the discharge chamber since they are known to dominate the discharge behavior in such discharges [33]. Computational results from DC-ION have suggested that the MiXI thruster is primary dominated, where the primary electrons are responsible for 95% of the ionization and accounts for 10% of the total electron density [12].

To investigate and improve miniature ion thruster performance, a complete experimental examination of the discharge chamber would provide critical insight into the discharge plasma behavior at these reduced scale lengths. Therefore, the objective of this chapter is to use a complete discharge map of key plasma parameters to understand the discharge plasma behavior and its relation to the performance as an ion thruster or ion source. The 3 cm Miniature Xenon Ion (MiXI) thruster is used as the platform to test several magnetic field and discharge configuration. The performance data are obtained using a simulated ion thruster operation at several discharge conditions. A complete EEDF and plasma parameter map for each configuration is obtained using a Langmuir probe and analyzed in conjunction

with the performance data.

5.1 Approach

Several sets of experimental measurements and analyses were conducted to characterize the performance and discharge structure for three different discharge configurations. This section begins with a description of the test facility and various components of the MiXI thruster. The magnetic field topology for each of three discharge configurations are then discussed along with the design intention of each subsequent configuration. Next, this section describes the methodology used for obtaining the simulated performance and discharge mapping data, including the necessary assumptions and the approached used for the Langmuir probe analyses. The section ends by describing an analysis procedure used to calculate the various species interaction rates based on the plasma properties and the associated collision cross-sections.

5.1.1 Experimental Setup

The miniature ion thruster experiments were conducted inside a 20" diameter by 36" height bell-jar vacuum chamber, shown in figure 5.1 at the UCLA Plasma & Space Propulsion Lab. A 7" cryopump allowed for a base and operating pressure of 2×10^{-6} Torr and less than 5×10^{-5} Torr, respectively. Although the pumping rate was significantly less than the chamber used in chapter 3, the chamber allowed for much better ease of access. Xenon gas was injected into the chamber using an Apex Vacuum 1.0 sccm flow controller through an electrically isolated gas feed line. Probes were fixed onto a set of orthogonally mounted Velmex XSlide linear stages configured to raster along an azimuthal slice of the discharge chamber.

The original MiXI thruster, shown and diagrammed in figure 5.2, was used as a modifiable platform to test various magnetic field configurations. The thruster has a 3 cm diameter

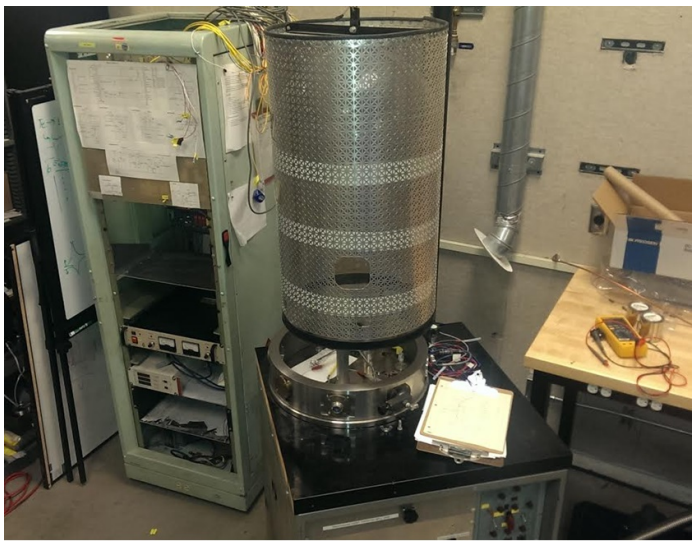

Figure 5.1: Bell-jar vacuum facility used for the miniature ion thruster experiments

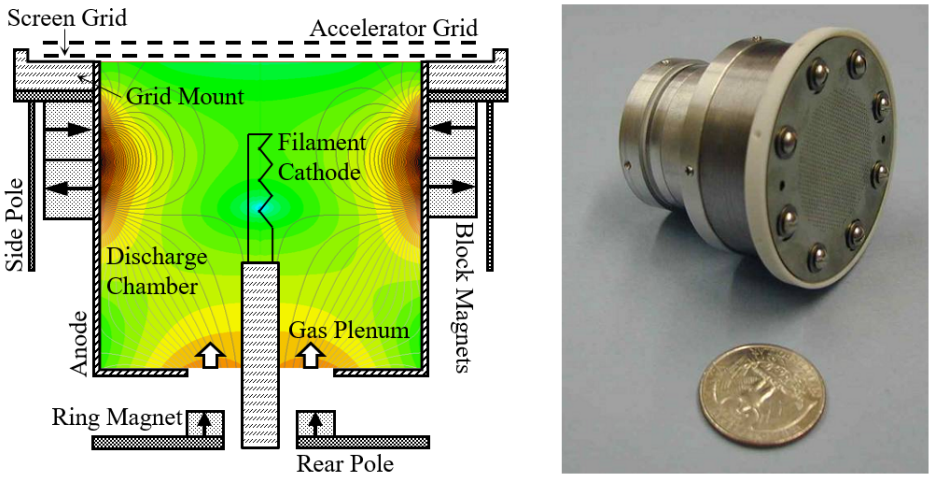

Figure 5.2: Image (right) and diagram (left) of the 3 cm diameter MiXI thruster (not to scale), in the 3-ring (3R) configuration, with the key components labeled and overlaid onto the magnetic field contour (in logrithmic scale).

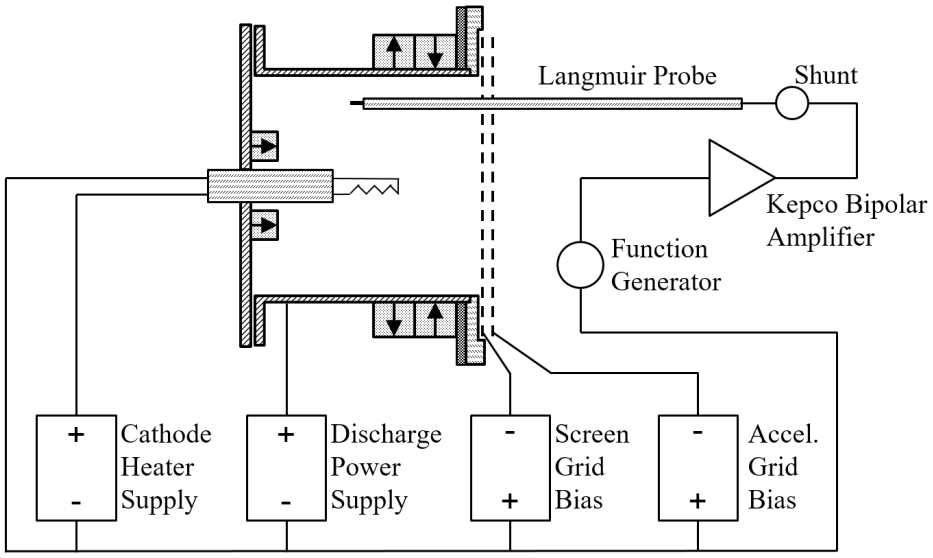

Figure 5.3: Electrical diagram of the discharge test apparatus including power supplies and the Langmuir probe circuit. Since an ion beam was not produced, the beam power supply was not connected and the negative terminal of the discharge supply was grounded.

by ∼3 cm length aluminum discharge chamber; the aspect ratio previously chosen for best discharge performance [12]. Xenon gas propellant was injected through an annular porous-metal gas injector located at the upstream end of the discharge chamber. The smaller overall grid diameter of MiXI mitigates the thermal deflection of the grids and allowed the spacing between the screen and accelerator grids to be tightly controlled. The MiXI grid system uses Small Hole Accelerator Grid (SHAG) optics that improve neutral confinement (∼5%) while maintaining high ion transparency (∼75%). The steel side pole piece improves the downstream ring cusp geometry by pulling the field lines closer to the walls towards the grids. The miniature discharge hollow cathode was replaced with a 5 mil tungsten filament cathode to reduce noise in the probe measurements and to focus on the discharge optimization, independent of the grid design. The filament was ∼2.5" in total uncoiled length and is typically heated with 18 to 20 W of power. A set of trim coils was added to allow fine tune the magnetic field within the center region of the chamber where the fields were weakest. A thermocouple was attached to the outer walls of the side pole piece.

The thruster experiments in this chapter were performed without ion beam extraction which allowed the discharge cathode to be grounded with the chamber. Figure 5.3 shows a simple wiring diagram of the MiXI thruster and power supplies required for plasma generation and measurements of the discharge. All voltage and current sources shown in the diagram are Sorensen DLM series power supplies. For some configurations, a secondary or tertiary discharge power supply was wired to the rear plate or to internally isolated ring electrodes to segment the chamber surfaces. The external trim coils, not shown in the diagram, were current controlled using a TTi Cpx400d power supply. The cathode heater supply provided between 8 to 12 volts across the filament during normal operation which generates primary electrons with much greater thermal spread compared to hollow cathodes. The negative terminal for the cathode heater supply is wired to the discharge supply common to ensure primary electrons do not gain excessive energies relative to the discharge voltage. In addition, the filament is installed in a manner that primary electrons created further upstream have higher energies than those created at the tip of the filament — a characteristic more similar to hollow cathode operation [42].

All measurements were recorded using the NI PXIe 4300 DAQ module that featured a 300 V_{rms} channel-to-channel isolation. Power supply voltage and current values were measured directly and through a shunt resistor, respectively. The Langmuir probe voltage sweeps were generated in LabVIEW and outputted through the NI PXIe 4322 DAQ module; the low voltage signal then sent to a Kepco BOP-100m bipolar amplifier. The Langmuir probe current was measured through a 32 Ω shunt resistor on high side of the power supply to avoid the leakage current in the Kepco supply.

5.1.2 Magnetic Field Configurations

The magnetic field contour in figure 5.4 shows the MiXI thruster configured with the original 3-ring (3R) [1], a 5-ring (5R), and a 4-ring (4R) cusp configuration. The ring-cusp fields were created by an axially magnetized continuous ring magnet upstream of the

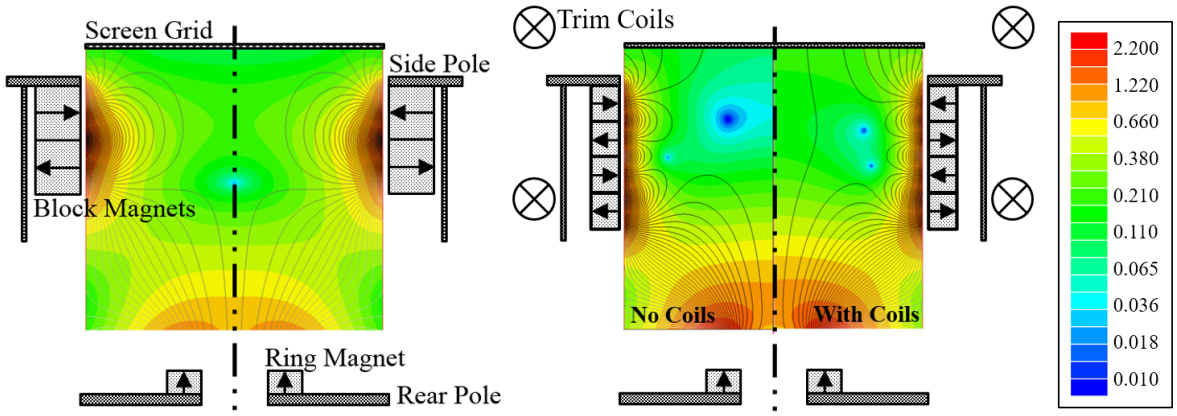

Figure 5.4: Diagram of the MiXI thruster test platform with the default 3-ring (left) and 5-ring (right) configurations. The computed values of the normalized magnetic field are in logarithmic scale and verified using a 3-axis Gaussmeter. Trims coils were placed around the thruster to superimpose an axial field inside discharge chamber.

chamber and radially magnetized discrete block magnets surrounding the cylindrical anode. Samarium cobalt permanent magnets were used for their high field strength and operating temperatures. The B-field geometries were characterized by comparing 2D simulations to measurements from a 3-axis probe gaussmeter mounted onto a 3-axis stage as shown in figure 5.7. The block ring magnets was modeled as a continuous ring magnet and the magnetization was modified to match the partially demagnetized permanent magnets. Figure 5.5 shows a comparison of the Maxwell 2D results and measured data. The actual hall effect measurement area has a finite offset within the Gaussmeter finite probe tip, limiting the actual mappable region of the discharge chamber. In an earlier research effort [1], the MiXI 3R discharge configuration was determined to have the most desirable overall performance compared to a wide range of discharge magnetic field options. The SmCo magnets used in the 3R configuration were originally used in the NSTAR thruster. As a result, these magnets only generate 70% of their original field strength at the face. This was found to provide higher efficiency and stable operation compared to later test that used full-strength NSTAR magnets. This is because the strong field generated by these full-strength magnets led to an impedence shift instability in the discharge due to over-confinement of the plasma electrons

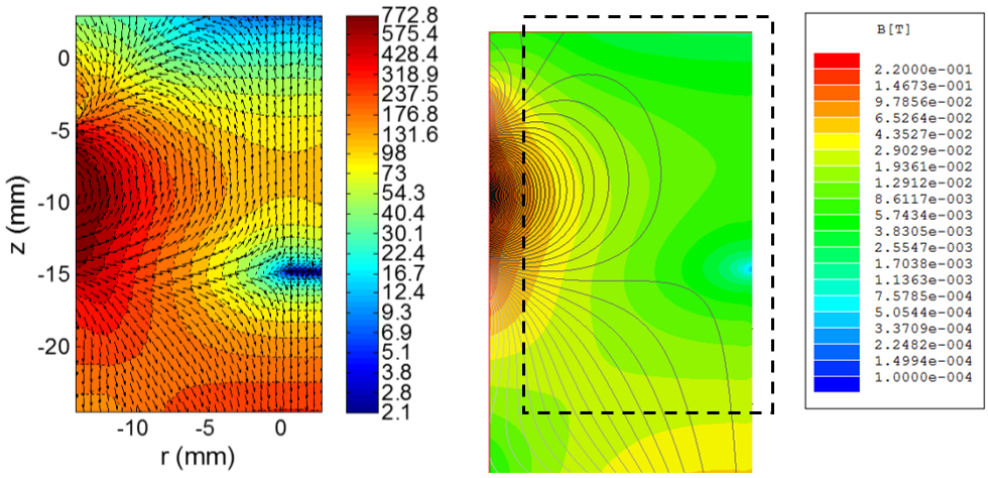

Figure 5.5: Comparison of the magnetic field lines and contour between Gaussmeter measured values (left) and computational results from Ansoft Maxwell 2D (right)

[28, 12].

The intention of the 5R design was to increase the size of the low field region in the chamber to expand the effective plasma volume and improve the beam flatness. The smaller magnets still produced strong magnetic fields but have shorter range compared to the 3R magnets. Preliminary simulations using the MCC particle pusher indicated better overall primary electron confinement despite the greater total cusp area. The expansion of the low-field region in the radial direction led to a squared scaling of the discharge volume. Therefore, primary electrons are able to translate greater distances before encountering a cusp element where they can potentially be lost. The added trim coils were able to manipulate the fields structure within the bulk region where the permanent magnetic fields were weaker. Shown in figure 5.4, the trim fields imposes an bulk axial field near the centerline and pushed the null region towards the edge of the discharge chamber. However, they were power inefficient in this configuration because of the large coil radius and the magnetic side pole piece that partially shielded out the external fields.

Figure 5.6 shows an additional field configuration that was also tested based on findings from the 3R and 5R testing. Full discharge maps for these configurations were not obtained

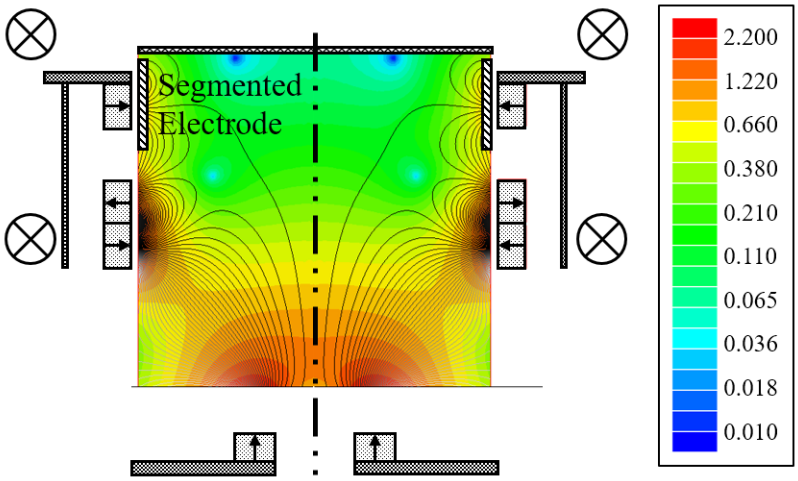

Figure 5.6: Diagram and magnetic field contour (kGauss) of the 4R configuration, which was the next iteration after the 5R configuration. A segmented electrode is installed at the downstream ring-cusp

due to problematic probe measurements caused by the nature of the discharge. However, the performance data and rudimentary discharge maps that was analyzed led to important findings for future discharge design considerations. The magnetic field shape was designed to diverge the field lines downstream from the cathode with the null region near the grid plane; the intention was to improve the beam uniformity. The configuration featured an isolated electrode at the downstream cusp that was biased to cathode potential in order to reflect the primary electrons. This technique has been demonstrated by previous researchers [54] to improve the discharge performance of larger ion thrusters. More details of the 4R design will be given in section 5.2.4 after discussing the 3R and 5R results.

5.1.3 Simulated Ion Thruster Performance

The ion optics for the MiXI grids were designed for a plasma densities typical of the default 3R thruster ($\sim 2 \times 10^{17}$ m^{-3}). In order to focus on discharge design and reduce the design variability of the grids, the discharge was characterized without beam extraction using a simulated ion thruster or "discharge-only" operation. The predicted performance

for the simulated discharge was determined base off a simple model described by Brophy [55]. This methodology has previously been implemented by several researchers on different ion thrusters and have been shown to reliably predict the discharge performance [15, 56]. The model accounts for an equivalent neutral flow rate since beam ions that would normally leave the thruster are instead neutralized at the grids and reinjected back into the discharge chamber as neutral particles; they thus contribute as an additional flow rate. The predicted beam current (I_b) is calculated by multiplying the measured total ion current incident to the grid system (I_g) with the reported ion transparency of the MiXI grid system, $I_b = I_g \Phi_i$. The effective neutral flow rate can then be calculated using:

$$\dot{m}_p^* = \dot{m}_p + \frac{I_b}{\alpha_m} \left(\frac{M}{e} \right), \tag{5.1}$$

where $\dot{m}_p$ is the flow rate as measured by the flow controller, α_m is the doubly charged ion correction factor, and M and e are the electron mass and charge, respectively. This expression assumes that all ions collected at the accelerator grid returns to the discharge as neutral atoms. Although Brohpy determined that only $\sim 45\%$ of the accelerator grid current reenters the discharge chamber in the J–Series thruster, the value is expected to be much greater for the MiXI thruster due to the geometry of the SHAG optics.

The expression for the discharge power must also be modified for the electrical configuration shown in figure 5.3. The beam ions in a flight thruster are neutralized by a cathode external of the discharge chamber. These electrons have negligible power consumption due to the low coupling voltage. In a simulated ion thruster, these ions are loss to the grids and the electrical current is instead balance with the discharge electrons that are extracted at the discharge voltage. Therefore, the beam current must be subtracted from the discharge current when calculating the discharge power and the expression for the discharge loss is written as:

$$\epsilon_b = \frac{(I_d - I_b)V_d}{I_b}, \tag{5.2}$$

Paramter	Values
Beam voltage	1089 V
Beam current	28.3 mA
Discharge voltage	25 V
Discharge current	0.503 A
Flow rate	0.51 SCCM
Discharge loss	444 eV/ion
Propellant Efficiency	0.79
Total Efficiency	0.56

Table 5.1: Performance data for the MiXI thruster calculated from the total extracted ion beam and beam profile [57].

where I_d and V_d are the discharge current and voltage, respectively. The mass utilization efficiency (η_{ud}), electrical efficiency (η_e), and total efficiency (η_T) are calculated using same standardized expressions from chapter 2.

The discharge performance data were measured by keeping the discharge voltage constant and slowing increasing the discharge current by adjusting the cathode filament heater power. The electron emission from the thermionic cathode is described by the Richardson-Dushman equation along with Schotttky effect as a result of the sheath electric field. Performance data were acquired at discrete flow rates and trim coils settings. The performance results were calculated with assumptions based on operational data of the original MiXI thruster with beam extraction shown in table 5.1. This includes: 1100 V beam voltage, grids with 75% ion transparency, no beam divergence, and negligible doubly-charged ion population. The beam divergence in the MiXI thruster was calculated to be $\sim 5^\circ$ based on Faraday probe measurements of the ion beam — this translate to a less than 1% reduction to the total efficiency. The high neutral density of the MIXI thruster (afforded by the SHAG optics), low electron temperature, and low gas ionization results in a doubly-charged ionization rates that are significantly lower than that for single ionization and thermalization of the primary electrons. The performance figures shown in section 6.2 will not include possible trim coil power and additional power usage and/or gas flow from the discharge and neutralizer cathode.

The beam flatness parameter (Eq. (2.6)) is generally calculated from the ion beam current-density profile, measured directly downstream of the accelerator grid. In order to predict the beam profile and flatness parameter in the simulated ion thruster, the ion current-density was instead calculated using the internal plasma maps that is described in the following section. The extraction for each individual beamlet was approximated as a flat planar sheath and the ion beam current-density can be described by multiplying the Bohm ion current [58] with the ion transparency:

$$j^*_{beam} = 0.6en_i\sqrt{\frac{kT_e}{m_i}}\Phi_i, \tag{5.3}$$

where the ion density (n_i) and electron temperature (T_e) are extrapolated from the discharge maps along the extraction plane. In reality, local plasma properties affect the ion transparency of each beamlet which would slightly alter the beam profile and divergence angle.

5.1.4 Discharge Mapping

The discharge mapping in this chapter uses a similar approach outlined in chapter 4. Unlike the 8 cm discharge experiment where the cathode filament was installed at a null region away from the chamber walls, ion thruster cathodes are mounted from the back of the chamber. Therefore, the probe slit was at the grid plane rather than the cylindrical walls which bypasses the complication of probing between the magnets in the previous chapter. A set of 0.75 mm thick stainless steel probing grids were fabricated and installed in lieu of the original MiXI grids. The probing grids feature a 1.5 mm thin slit across the chamber diameter which allowed for full probe access. The additional perpendicular slit was originally designed to match the total open area of the MiXI grids but later proved unnecessary due to the cutting resolution if the water-jet. To account for the increased neutral transparency, the gas flow rate was increase by a factor of 2.5 times to match the performance curves when

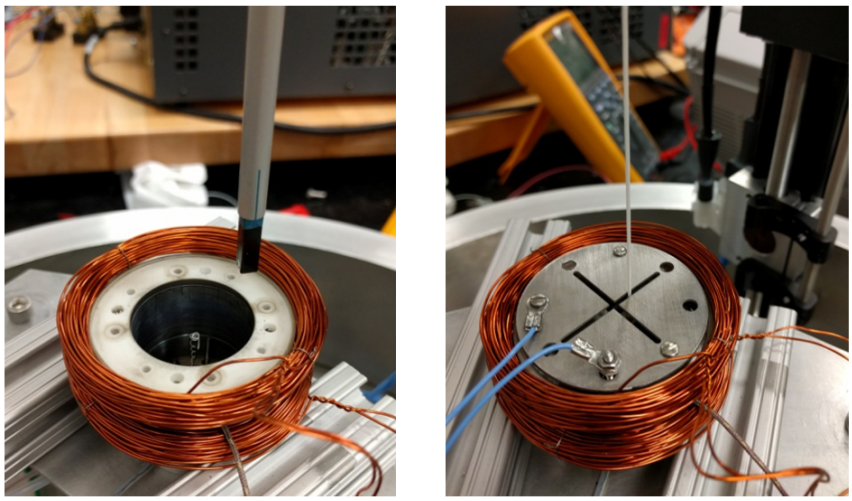

Figure 5.7: Left: The MiXI thruster platform without screen and accelerator grids. Also shown, the Gaussmeter probe used to map the magnetic fields. Right: Probing grids installed with slots to allow 2D Langmuir probe mapping of the discharge during operation.

operated using the MiXI grids. The set of probing grids are spaced roughly 3 mm apart to minimize the escape of charged particles. The Langmuir probe was able to access an entire azimuthal slice of the discharge chamber sans the region very near the cathode filament.

Figure 5.8 is a diagram of the MiXI 3R configuration overlaid with a typical raster scan pattern used in the discharge maps. Each scan generally includes over 500 data points with smaller step sizes near the cusps to obtain higher resolution in the high B-field regions of the discharge. A unique pattern was generated for each configuration to balance the data acquisition time and contour resolution. All probe movements and data acquisition was automated using a custom LabVIEW VI. Plasma properties were measured using a cylindrical Langmuir probe, constructed with a 1.2 mm length by 0.2 mm diameter tungsten wire protruding from a 1.1 mm diameter alumina tube. Preliminary tests were used to confirm that the Langmuir probe did not significantly disturb the discharge plasma during operation. There is at most a 2% effect on the discharge current and estimated beam current when the probe was scanning near the center-line upstream region inside the discharge chamber. The output DAQ generated a triangle wave voltage sweep at 200 Hz and acquired 1 second of

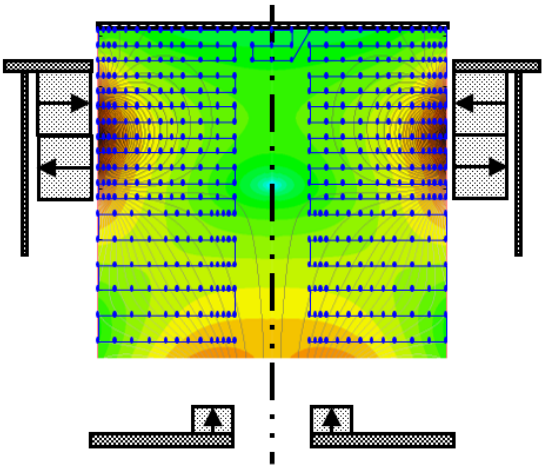

Figure 5.8: Example Langmuir probe scan pattern used to generate the discharge maps overlaid onto the magnetic field contour. Center region is empty to avoid contact with the discharge filament cathode.

data at each spatial location. The NI PXIe 4300 DAQ module is capable of 16 bits analog input resolution which allowed us to resolve the ion and electron saturation curves in a single sweep.

5.1.5 Ion Generation Rates and Primary Electron Loss

From the plasma parameter maps, we can examining the ion generation rates and primary electron loss behavior throughout the discharge chamber. The doubly-charged ion population have been shown to be the dominate internal erosion mechanism in certain ion thruster designs and/or discharge conditions [59]. Ion thrusters typically operate between 23-27 V discharge as the sputtering threshold energy for singly-charge ions is ~25 eV for most materials used inside the discharge chamber [60]. However, the doubly-charged ions impact the screen grid and the discharge cathode at a square-root of two greater velocity than the singly-charged ions. The generation rates of singly (I_R^i) and doubly-charged (I_R^{ii}) ions are estimated through probabilistic collision calculations using differential collision

cross-sections [61, 62, 63] for the corresponding interactions:

$$I_R^i = n_0 n_e \langle \sigma_i v_e \rangle \, V + n_0 n_p \langle \sigma_i v_p \rangle \, V, \tag{5.4a}$$

$$I_R^{ii} = n_i n_e \langle \sigma_{ii} v_e \rangle \, V + n_i n_p \langle \sigma_{ii} v_p \rangle \, V, \tag{5.4b}$$

where n_0, n_e, n_i, and n_p are the neutral, plasma electron, ion, and primary electron densities, receptively, V is the volume, v is the velocity of the incident particle, and σ is the collision cross-section of the interacting particles. The cross-sectional values have been experimentally tabulated over a wide range of incident electron velocities [61] and a piece-wise polynomial curve fit was used for integration over a range of electron energies. The angle bracketed terms represents reaction rate coefficients that can also be expressed as the particle's velocity multiplied by the reaction's collision cross-sections. The reaction rates for plasma electrons were then calculated by integration with the Maxwellian distribution for a given plasma electron temperature. The voltage across the filament heater lead a significant energy spread for the primary electrons, therefore, their reaction rate coefficients are calculated by integrating the primary EDF determined from the probe data:

$$n_p \langle \sigma_i v_p \rangle = \sqrt{\frac{2}{m}} \int_0^\infty F_p(\varepsilon) \sigma(\varepsilon) \sqrt{\varepsilon} d\varepsilon, \tag{5.5}$$

where ε is the electron energy relative to the plasma potential, $\sigma(\varepsilon)$ is the differential cross-section, and $F_p(\varepsilon)$ is the primary EEDF.

All the ions produced are ultimately loss to the chamber walls as no beam was extracted and the ion-electron recombination time is much greater than the its confinement time [64]. For all discharge conditions presented in this paper, there was a negative-going sheath to all surfaces within the chamber walls. Therefore, the ion wall loss can be estimated by integrating the Bohm current at the edges of the discharge map. The remaining ion loss to the filament, filament holder, and upstream cathode surface near the centerline was estimated through a current balance between the total ion production and loss to other surfaces.

In addition to the primary electron loss to ionization, they were also loss to the chamber walls, excitation collisions, and thermalization through collisions with the plasma electron. The excitation loss was calculated in an identical manner to ionization using the corresponding cross-sections. The reaction rate for thermalization was calculated using the Spitzer [64] slowing down time (τ_s) where $n_0\langle\sigma_s v_p\rangle = \tau_s^{-1}$. The primary electrons wall loss cannot be reliably calculated in the same manner as the ions. The magnetic fields and the negative-going sheath reflects an unquantifiable portion of the primary electrons propulsion incident to the walls. However, the primary electron power wall loss (P_w) can be estimated using a power balance with the discharge power (P_d) by integrating over the primary EDF:

$$P_d = \int_V (R_i E_i + R_{ii} E_{ii} + R_{ex} E_{ex} + P'_{pl}) dV + P_w, \tag{5.6}$$

where R_* is the local reaction rate, $R_* = I_R^*/V$, and E_* is the energy required for each corresponding interaction [61, 62]. The subscripts ex represents the combined excitation collisions of both the primary and plasma electrons with the neutral gas. The P'_{pl} is the primary electron power per volume deposited into the plasma electron population which can be estimated by:

$$P'_{pl} = R_{iz}(E_p - E_{iz}) + R_{iiz}(E_p - E_{iiz}) + R_{ex}(E_p - E_{ex}) + \frac{n_p}{\tau_s}\bar{\epsilon}_p, \tag{5.7}$$

where $\bar{\epsilon}_p$ is the average primary electron energy calculated from the local primary EDF data. This Spitzer term accounts for the thermalization of primary electrons that do not encounter an ionization or excitation collision. In this calculation, it is assumed that all remaining primary electron energy after an inelastic collision is transferred to the plasma electrons. The Spitzer slowing rate is higher for lower energy electrons and their confinement time is longer. However, the error associated with this assumption will depend on the loss characteristics of the discharge design.

5.2 Results & Discussion

This section compares the 3R, 5R, and 4R configurations via discharge performance and simulated thruster performance metrics. These performance trends are used to assess macroscopic discharge plasma behavior. The results of the discharge plasma parameter are then used to estimate species reaction rates within the discharge and are used to understand the overall performance behavior.

The performance and discharge mapping data were all acquired at the same relevant discharge operating conditions. The screen and accelerator grids were biased to 5 and 20 volts below the cathode potential, respectively. An additional collector plate downstream of the thruster confirmed that there was negligible ion current leaving the thruster. Unless stated otherwise, the discharge voltage is kept at 25 V despite certain field configurations showing better performance at lower or higher voltages. The discharge current was controlled through adjusting the filament cathode heater power. Measurements were acquired once the discharge performance stabilized when thermal equilibrium was reached.

5.2.1 Performance Data Analysis

The simulated performance data at different specified flow rates and discharge voltages are shown in figure 5.9 for the default MiXI 3-ring (3R) configuration. It is important to note that the efficiencies in figure 5.9c, figure 5.9d, and table 5.1 does not include many possibly important factors such as the thrust correction factor and contributions from the discharge or neutralizer cathodes. These values only serve as a comparison metric between the beam extracted and simulated performance data for the 3R configuration and as a baseline performance for comparison between the 3R and subsequent designs presented in this thesis.

Although it appears as if the discharge performed universally better at higher flow rates from the figure 5.9a, the beam current was not constant along each curve, unlike standard

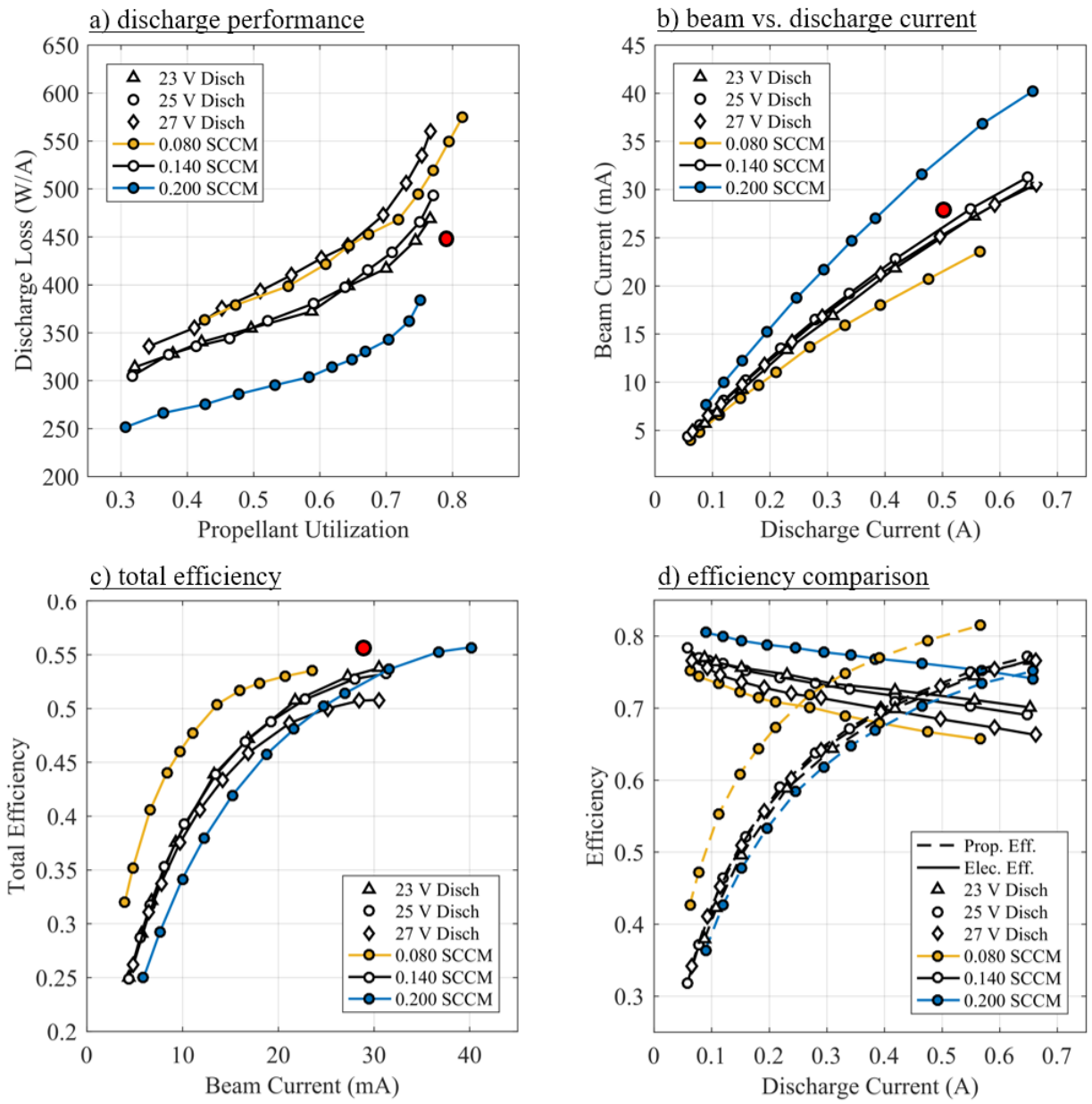

Figure 5.9: Performance assessment of the default 3R configuration at a range of base neutral gas flow rates. The curves were generated by adjusting the heater power to increase the discharge current while keeping all other power supplies constant. Red circle represents the discharge condition shown in table 5.1.

performance curves shown in figure 2.3. Both the simulated beam current and effective gas flow rate increases moving right-ward along each curve. Figure 5.9c shows that the discharge was more efficient at lower flow rates when extracting lower beam currents and vis-versa. At 0.70 A discharge current, the device was already operating at >260°C measured on the side pole piece. In large part, this was due to the additional heat load from the tungsten filament that would be absent when replaced with a hollow cathode. Therefore, the data points were limited to those shown to prevent demagnetization. Collectively, the performance curves provided an adequate evaluation of the achievable discharge performance at various throttle conditions.

The performance estimates are similar to those previously obtained by Wirz [14] when using MiXI in full thruster configuration with beam extraction, as summarized in table 5.1. Inspection of the 0.140 SCCM flow rate condition at the 25 V, ∼0.50 A discharge condition shows that the beam current, discharge loss, and total efficiency values are within 5% of those obtained by Wirz. The slight differences are possibly attributed to the cathode filament placement and extraction characteristics of the grids. The close agreement provided confidence with using the simulated operation to obtain reasonably accurate performance data for the other magnetic field configurations and discharge conditions.

Figure 5.9b shows the simulated beam current in relation to the discharge current at a range of specified flow rates. Since there is no beam extraction, the dominate mechanism of particle escaping the discharge chamber is the thermal motion of neutrals through the openings of the grids. A majority of the neutral gas heating was indirectly through radiation from the filament cathode and the chamber temperature remains relatively constant throughout the discharge current sweep. Therefore, each specified flow rate curve roughly corresponds to a constant neutral density inside the chamber despite the changing discharge power. The ionization path length is inversely proportional to the neutral density while the confinement time remains relatively constant for a given discharge design. The results show that for any given discharge power, the 3R beam current increases with with the neutral gas

density as more primary electrons are able to encounter an inelastic collision before being lost to the walls.

Figure 5.9d shows a breakdown of the total efficiency. At higher specified flow rates and neutral densities, the electrical efficiency is higher because of the shorter ionization mean-free-path while the propellant utilization is lower as more neutral particles are loss through the grids. For a given curve, the propellant efficiency initially increases rapidly with the discharge current and plasma density. The total grid current scales about proportionally to the plasma density while the neutral grid loss remains relatively constant. At increasingly higher discharge currents, the propellant efficiency curves begin to taper off as the plasma density rises and the neutral density depletes. However, there is higher collisionality between the primary and plasma electrons and more of discharge energy is thermalized into the plasma electron population. The plasma heating leads to higher electron temperatures that directly increases the loss mechanism for all charged species and thus, the electrical efficiency decreases.

Focusing on the performance comparison between the various discharge voltages in figure 5.9a shows an uncommon trend in the 3R configuration. For discharges with good primary confinement (e.g., most larger discharges), raising the discharge voltage directly increases the primary electron energy and ionization rate which would typically result in a lower discharge loss. This trend was ambiguous within these performance data and in some cases, the opposite trend was observed. The behavior is a result of the poor primary electron confinement of the 3R discharge as a majority of the primary electrons were loss to the walls before ever colliding with a neutral atom. Therefore, most of the added discharge energy has a negligible effect to ionization and instead contributes as an additional electrical loss. This analysis is supported by inspecting the efficiency curves at the different discharge voltages. Figure 5.9b shows that the beam current at a given discharge current is unaffected by the increase in discharge power. Thus there is an overall drop in the electrical efficiency while the propellant utilization remains unchanged in figure 5.9d.

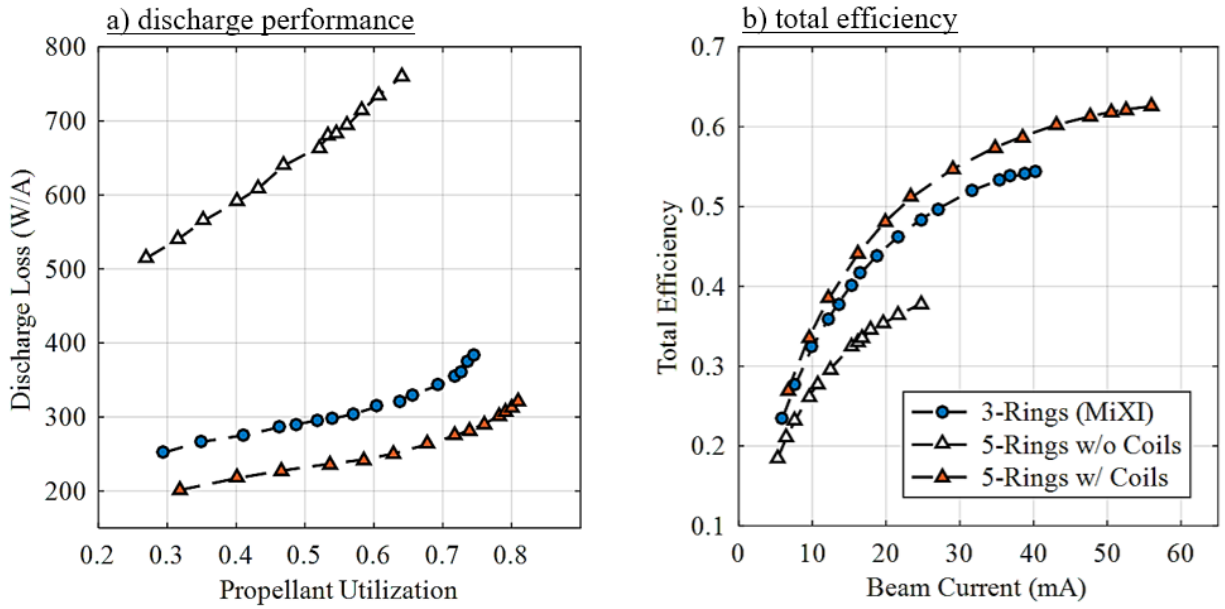

Figure 5.10: Performance comparison of the default 3R and modified 5R configuration. Results show high discharge loss for the 5R configuration without trim coils and a substantial increase in the estimated performance with the trim coils.

Figure 5.10 is a performance comparison between the 3-rings and 5-rings magnetic field configurations. The performance curve chosen for each configuration represents a flow rate that showed the highest total efficiency near 0.50 A of discharge current. The results show that the default 3R outperforms the non-trimmed 5R configuration. The 5R performance was much closer to the 3R configuration near the start of testing and gradually decreased as thermal equilibrium was reached. This performance loss was caused by demagnetization of the permanent magnets (up to 40% reduction at the magnet face) due to excessive temperatures which was also confirmed with the Gaussmeter. The performance of the partially demagnetized 5R configuration increased gradually with increasing trim coils currents, reaching a maximum with an additional ∼60 Gauss of trim B-field. The trim coils allow the 5R estimated performance to exceed the 3R configuration by notable margin, achieving higher propellant utilization and lower discharge loss at a given beam current. However, these performance values do not factor in important parameters such as beam flatness. Measurements of the internal plasma structure are required to understand the mechanism for

the performance increase with the trim coils.

The 4R configuration was developed after analyzing the first discharge maps for the 3R and 5R configurations. The performance and efficiency measurements shown in figure 5.11 was very promising but as previously mentioned, discharge mapping data for this configuration shows an undesirable plasma structure for ion thruster operation that is later discussed in section 5.2.4. However, the 4R confinement mechanism is similar to that achieved by the 5R configuration and a more extensive performance data was acquired that is useful for the purpose of discussion.

Comparing the performance data trends between the 3R and 4R configuration gives insight to the confinement behavior of each discharge. As previously discussed, increasing the discharge voltage in the 3R configuration reduced the performance due to the poor primary electron confinement. The opposite trend is noted in all of the plots in figure 5.11. With increasing discharge voltage and power, figure 5.11b shows that there is a roughly linear increase to the beam current. Shown in figure 5.11, this increases the propellant utilization with relatively no change to the electrical efficiency (which dropped in the 3R configuration).

Inspection of figure 5.11b between the various specified flow rate shows an interesting trend. As recently discussed, each curve corresponds to a discrete neutral density and thus the beam current curves for the 3R data each have a distinct slope. The 4R discharge exhibits a slightly different trend since, where for lower discharge currents (i.e. below 0.2 A), increasing the neutral gas density does not noticeably increase the beam current. This indicates that the primary electrons loss was independent of the collisional mean-free-path at the tested flow rates and that there was essentially no primary electrons loss to the walls at the lowest neutral density tested. Therefore, the plasma generation was only limited by the available discharge energy and increasing the flow rate only reduces the propellant efficiency. At discharge currents greater than 0.2 A, the data shows that the beam current plateaus off quicker at lower base flow rates. The plasma was more highly ionized with higher electron temperatures at lower specified flow rates and thus, there is more plasma loss to the walls.

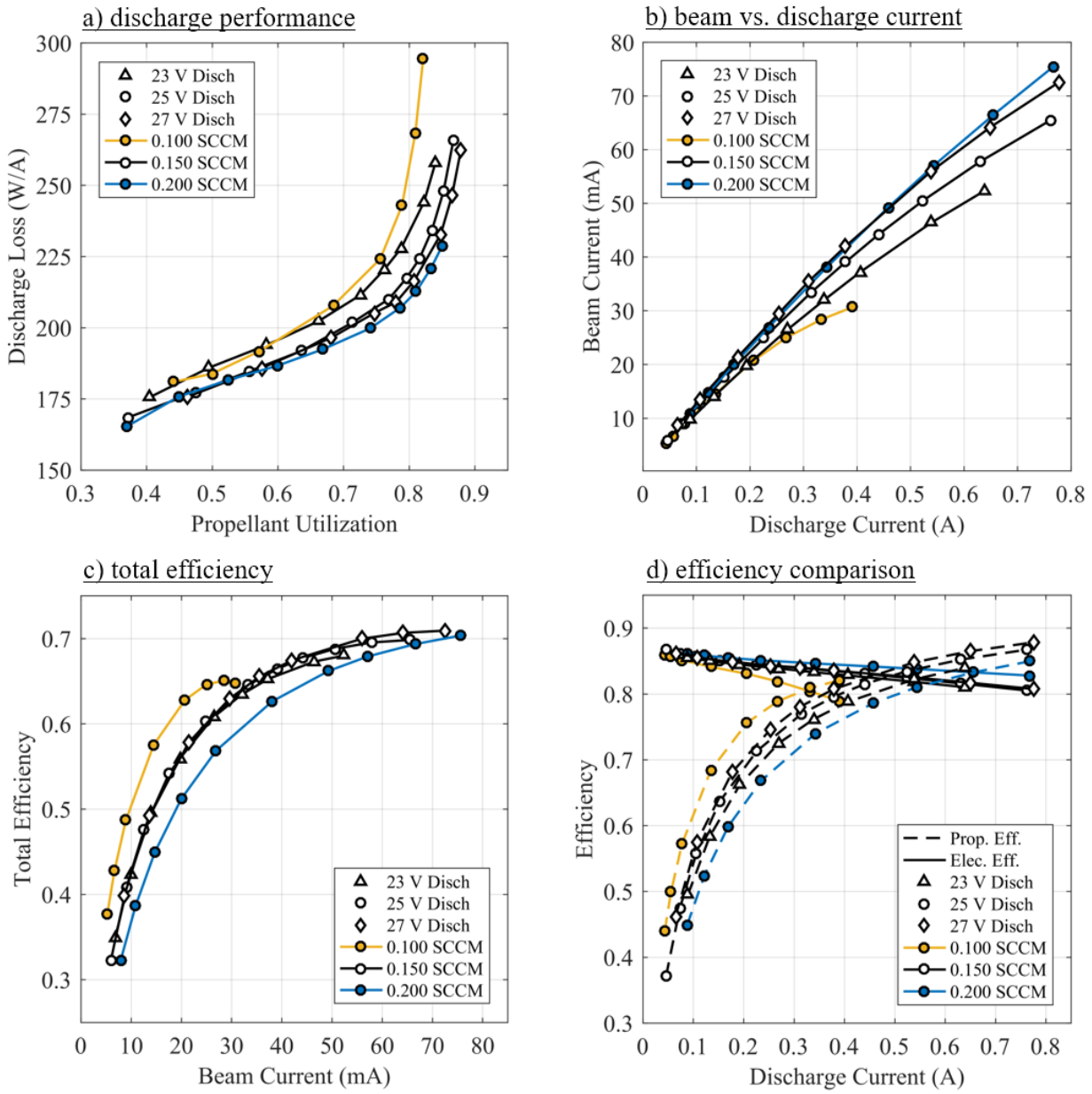

Figure 5.11: Performance assessment of the 4R configuration at a range of discharge voltages and specified neutral gas flow rates.

5.2.2 Discharge Map Analysis

The results shown in figure 5.12 are interpolated contour plots of the plasma parameters for the 3R configuration measured at 0.35 A discharge current and 0.140 sccm flow rate. The plasma density structure shows strong correlation with the magnetic fields structure shown in figure 5.4, an attribute similar to the results found in chapter 4. The primary electron contour coincides within the plasma density structure and the population accounts for more than $\sim 10\%$ of the total electron density within the bulk region. The electron temperature ranges between 2.5 to 3.0 eV and exhibits a more gradual delineation compare to the density contours. The plasma potential is, by and large, uniform at ~ 28 V relative to the cathode potential throughout the entire discharge chamber.

The 3R configuration shows a notably flat projected beam profile similar to the extracted beam measurements reported by Wirz. Figures 5.4 and 5.12 show that the 3R discharge field topology aligns the cusp and plasma structure across the extraction plane. This topology was generated by the two closely spaced ring-cusps, which pushes the null region of the downstream ring-cusp past the grid plane. The primary electrons were then confined in between the magnetic cusp and the screen grid at cathode potential. This is important in the MiXI thruster due to design of the grid mounting fixture which limits the proximity of the downstream ring-cusp to the extraction plane. However, the two ring-cusps also produces a relatively strong point-cusp in between the two null regions. The plasma and primary electron densities are shown to peak at the upstream ring-cusp null region — hence they are partially confined by the virtual point cusp in between the ring magnets and cannot freely diffuse to the extraction plane.

The overall low electron temperature is an indication of poor primary electron confinement as most of the discharge energy is lost directly to the chamber walls rather than to ionization or thermalization with the plasma electrons. As a consequence, the majority of the ionization is directly from primary electron ionization rather than the high energy tail of the plasma electron population. Therefore, the primary electron density is higher

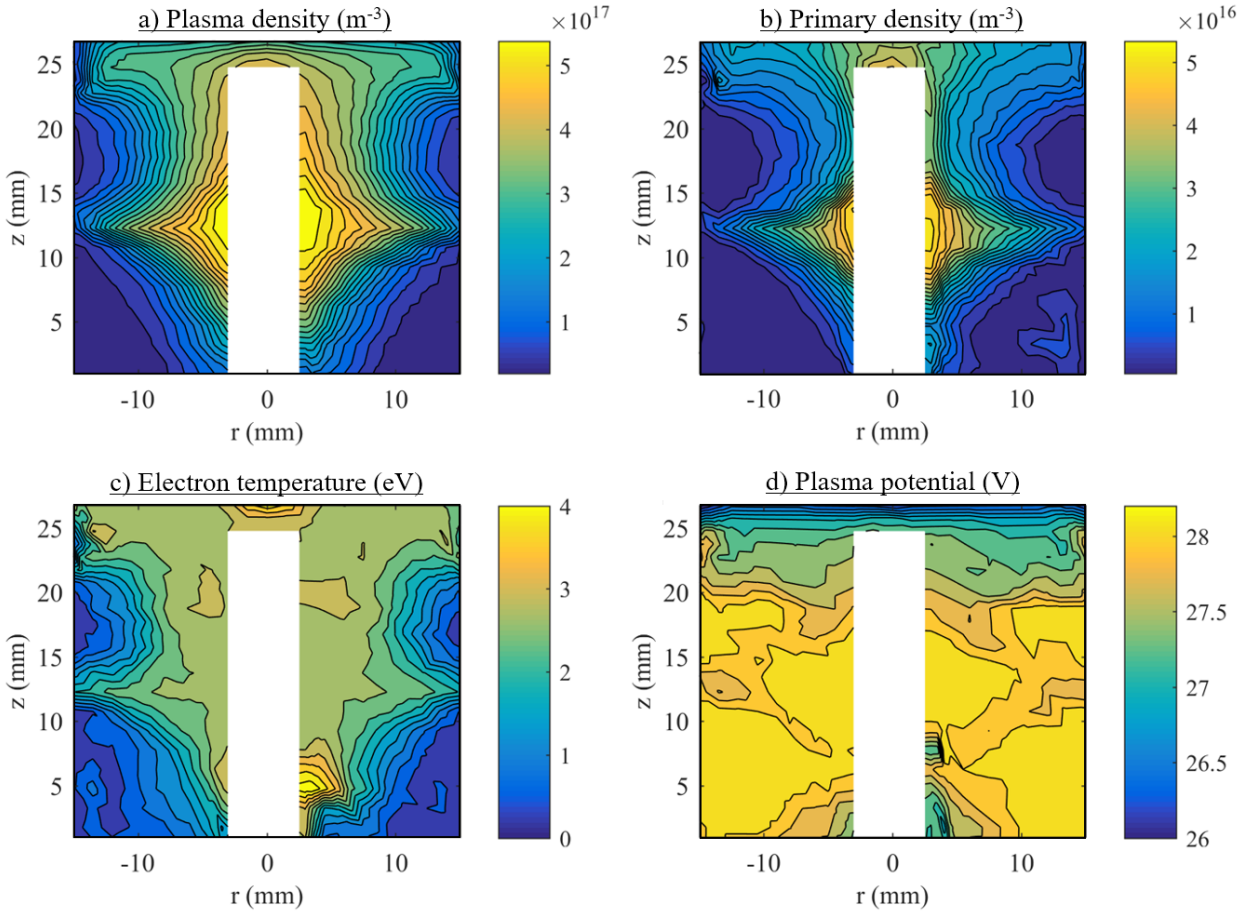

Figure 5.12: Plasma parameter maps for the MiXI 3R discharge for a 25 V, 0.30 A discharge and 0.140 SCCM specified flow rate. The bulk plasma structure parallels the magnetic fields shown in figure 5.4 and the overall values indicates high primary loss.

than conventional sized discharges and the structure resembles a "skeleton" of the plasma density contour. In addition, the plasma potential values indicate a strong negative (electron-repelling) sheath of about one electron temperature. The sheath potential is self-consistently established to maintain charge quasi-neutrality within the plasma. The high sheath potential indicates insufficient confinement of the electrons. The negative sheath is a poor mechanism for electron confinement because the electrostatic field mostly reflects only the low energy electrons while the high energy electrons are disproportionally lost.

The contour plots in figure 5.13 are a comparison of the plasma parameters for the 5R configuration, measured at the same discharge and flow conditions, with and without the

trim fields. The discharge plasma without trim coils exhibits characteristics similar to the 3R configuration but with worse confinement. The plasma density, primary density, and electron temperature are lower throughout the discharge chamber. The bulk plasma extends almost entirely to the chamber walls due to larger low B-field region and weaker cusp fields. With the addition of the trim coil fields, there is a large increase to the plasma density, primary density, and electron temperature. As shown in figure 5.5, the trim coils generate a predominately axial magnetic field in the bulk plasma which obscures any direct path for the primaries to reach the anode wall. Therefore, the primary electrons are confined to the center-line of the discharge where the primary density is over 4 times greater than without any trim fields. Subsequently, the electron temperature is almost twice as high near the center-line region and higher throughout the discharge chamber. The more pronounced gradient along the radial direction is expected as electrons must now diffuse across axial magnetic fields to reach the anode. The higher center-line primary density and electron temperature leads to a local increase to the ionization rate and plasma density values that are up to 2.5 times greater than the non-trimmed condition. The plasma potential, although lower than the non-trimmed results, is still almost an electron temperature above the discharge voltage and indicates that the there is still high plasma electron loss to the chamber walls.

The strong center-line densities are traits similar to earlier Kaufman thruster designs, which also had a predominately axial magnetic field. Floating point voltage and ion saturation oscillations were detected in the Langmuir probe measurements for the 5R trimmed condition. The oscillation frequency ranged from 1 kHz to 20 kHz and was strongly correlated to the trim coil currents. No detectable oscillations in the discharge current suggests that the probe oscillations are azimuthal in nature. This is similar to some Kaufmann thrusters where $E \times B$ driven instabilities increase the radial transport of electrons.

The mapping results show that the performance leap in the 5R trimmed configuration is almost entirely attributed to the improved primary electron confinement. Comparing the primary electron density contours between the 3R and 5R configuration show significant

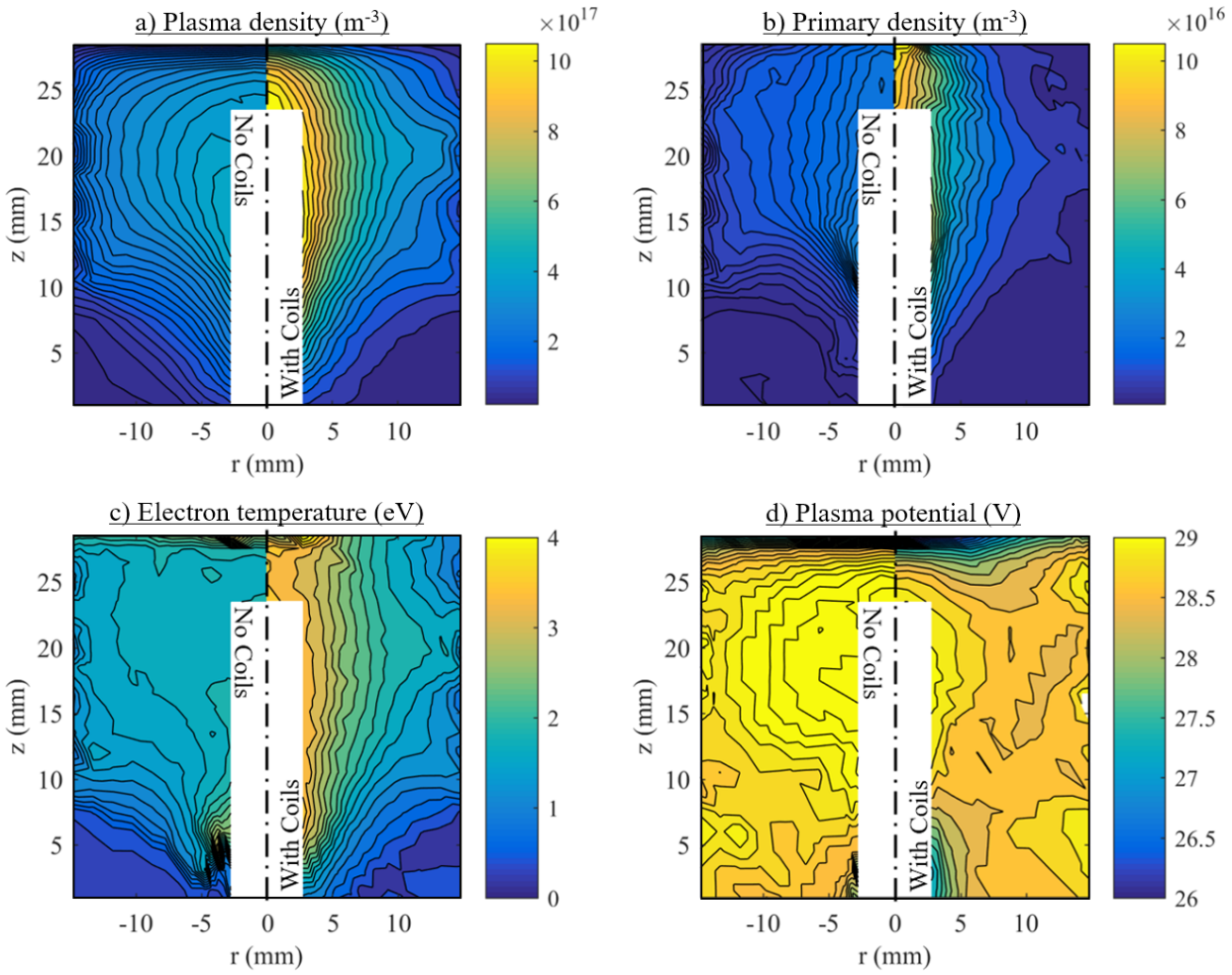

Figure 5.13: Discharge mapping results of the 5R configuration. The left and right side of each contour map shows the plasma structure with and without the trim coil magnetic fields.

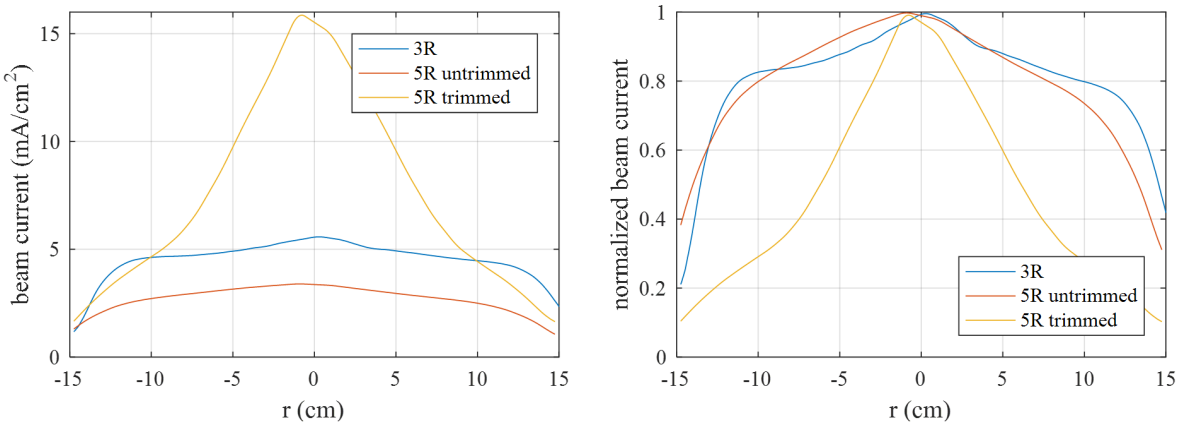

Figure 5.14: Non-normalized (left) and normalized (right) beam current profile for each configuration, estimated from the plasma parameters from the mapping data near the exit plane of the discharge. Note: the beam current estimates are based on an ion transparency of 75% was assumed across the grid plane and grid perveance considerations are not included.

difference between the losses to the anode wall. The plasma and primary electrons losses are coupled together for conventional ring-cusp discharges, leading to high primary loss at the smaller-scale. The weak axial fields in the 5R discharge establishes a "magnetic filter" or "shield" in front of the cusp element to prevent primary electron loss without substantially impeding the collection of the discharge current.

Figure 5.14 shows the projected beam profile for each configuration, calculated from the plasma density and electron temperature values along the extraction plane. Although the 5R trimmed configuration theoretical operated more efficiently, as measured by the greater total ion current collected at the grids, the beam profiles show that it also has the worst beam flatness. With the MiXI grids, the 5R trimmed performance is strongly overstated as the beamlet current surpasses the perveance limit of the grid design. In addition, the very non-uniform beam would lead to faster and uneven erosion of the ion optics and poor extraction characteristics. In addition, the center-line primary density may lead to high local generation of doubly-charged ions. The NSTAR thruster also had axially confined primary electrons, albeit less severe, which was found to have depleted the neutral population, increased the

local ionization, and elevated the generation of doubly-charged ions.

5.2.3 Ion and Primary Electron Rate Analysis

The singly and doubly-charged ion generation rate contour maps for the 3R and 5R trimmed configuration are shown side-by-side in figure 5.15. The primary electron excitation and thermalization contour maps are shown in figure 5.16. The contour map for the untrimmed 5R configuration are qualitatively similar to the 3R analysis and are not presented here. The volume averaged rates are tabulated on table 5.2 but have high expected errors because of the following factors:

1. The plasma density at the extraction plane is expected to be lower than when operated with a proper grid system due to the high local neutral transparency.

2. The local depletion of the neutral density in the bulk plasma generation region and overall gradient in the axial direction is not accounted for.

3. The plasma parameters in the filament region must be interpolated as well as charged particles loss to the cathode filament.

4. The error in the electron temperature has a non-linear effect on the reaction rates for plasma electron ionization.

Regardless, the following results are still informative for relative comparison between the various interactions.

For the 3R configuration, the results are consistent with a weakly ionized, low electron temperature plasma. The low plasma-to-neutral density ratio and high wall loss results in low transfer of energy between the primary and plasma electrons. This is evident in the low thermalization rates shown in figure 5.16b and quantified in table 5.3, which leads to the overall low electron temperatures. The low plasma density also means that there is a negligible double ion generation rate ($< 1\%$) since electrons are much more likely to

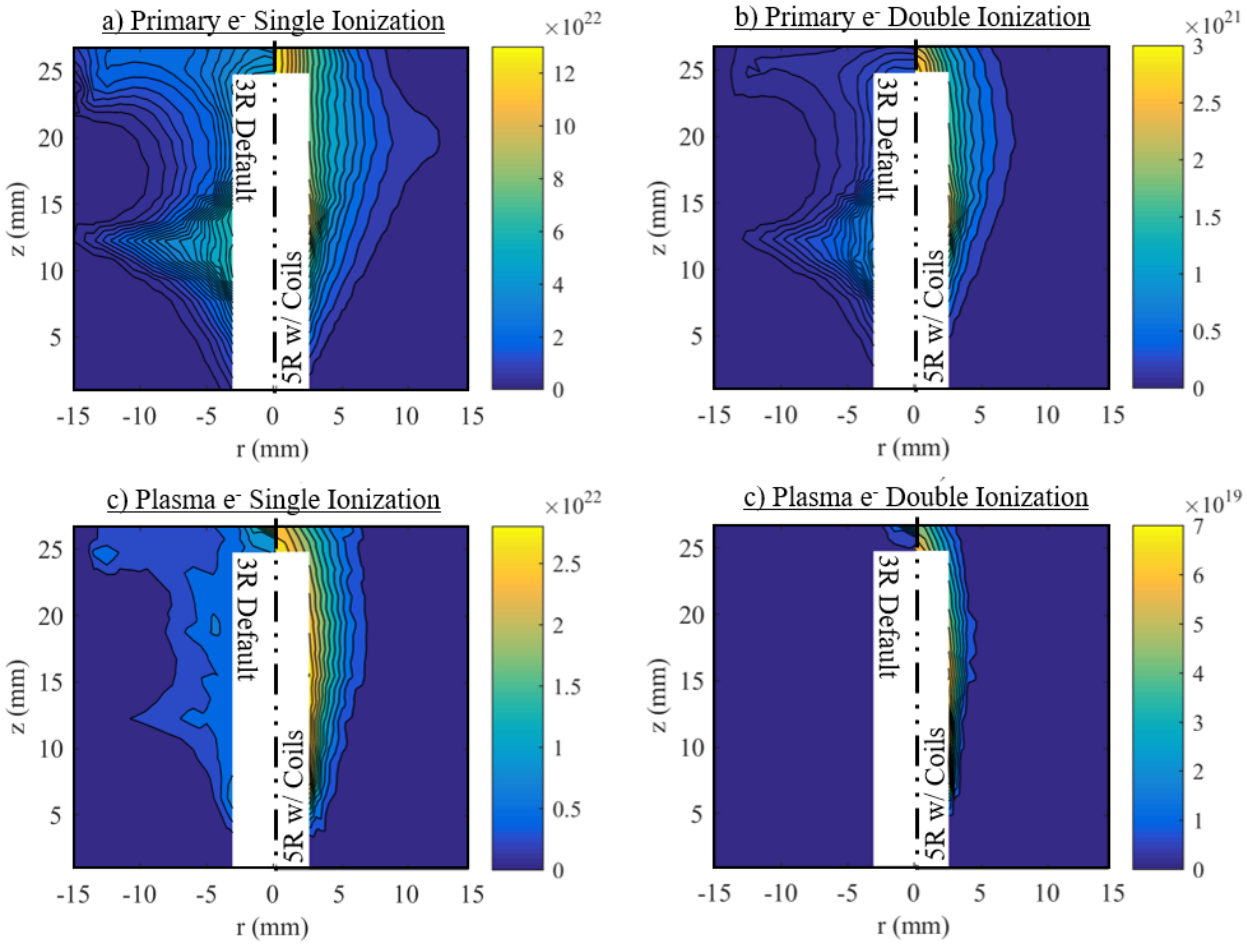

Figure 5.15: Contour maps of the local reaction rates ($m^{-3} \cdot s^{-1}$) for singly and doubly-charge ion generation through ionization collision by primary and plasma electrons. The left and right side of each map represents the 3R and 5R trimmed configuration, respectively.

Configuration	P_p^+	P_e^+	P_p^{++}	P_e^{++}	P_{total}	L_{Grid}	L_{Side}	L_{Rear}	$L_{Cath.}$
3R Default	68.9	10.4	0.45	∼0	79.7	22.6	9.4	1.3	46.5
5R w/o Coils	37.5	0.14	0.20	∼0	37.8	17.0	18.9	1.00	1.90
5R w/ Coils	66.2	12.5	0.9	∼0	79.6	26.4	25.8	1.2	22.4

Table 5.2: Ion generation (P) and loss (L) rates (mA) for the various discharge configuration. The generation terms are calculated from volume integration of the generation rates and the loss terms from surface integration using the plasma parameter maps.

collide with a neutral atom than an ion. As previously surmised, most of the ions are generated directly from primary electrons due to the low electron temperatures. Figure 5.15 and table 5.2 supports these findings and those by Wirz [33] that the MiXI discharge is a "primary ionizer," which accounts for over 80% of the total generated ions. The excitation rates are similar to the ionization rates due of their similar cross-sections and interacting particles. Shown in table 5.2, there is estimated to be high ion loss to the filament and upstream cathode surface. As discussed in previous section, the peak ion density is at the upstream null region. It is suspected that a large portion of the ions generated in this region are collected by filament and filament holder. These components reside along the virtual point cusp, in which the ions must diffuse across to reach the extraction plane. Table 5.3 also supports the simulated performance data analysis which indicated that a majority of the primary electron energy is deposited directly to the anode walls.

The 5R trimmed contours show that there is elevated ion generation along the centerline region. The axially confined primary electrons lead to a higher thermalization rates, plasma densities, electron temperatures, and ionization rates from plasma electrons along the centerline. In contrast, the total volume generation is estimated to be similar to the 3R discharge because the centerline region accounts for only a small portion of the total volume. Table 5.2 indicates that there is higher ion loss to the cylindrical walls compared to the 3R discharge. The weak axial magnetic field of ∼60-100 G is adequate for primary electron confinement, but are insufficient to confine the diffusive plasma electrons as the hybrid Larmor radius is on par with the radius of the discharge chamber. There is expected to be high ion loss to

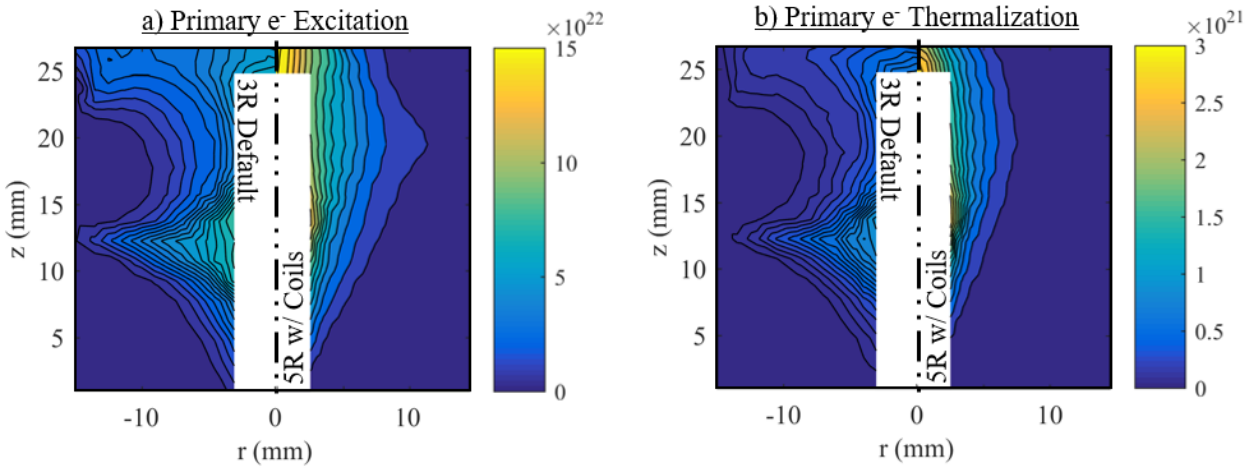

Figure 5.16: Contour map of the local reaction or loss rates ($m^{-3} \cdot s^{-1}$) for the primary electrons through excitation and thermalization. The primary electron loss rates for ionization collisions are identical to the ion generation rate in figure 6.11.

the filament due to the axial generation but still lower than the 3R discharge as the plasma is not confined by the weak axial B-fields. Although the doubly-charged ion generation rate is slightly higher than the 3R discharge, the localized and volume rates are still negligible. However, the plasma mapping alone is insufficient to estimate the double ion generation, particularly when it is caused by localized neutral depletion. A neutral model is required estimate the neutral density distribution rather than using a volume average based on the total flow rate and grid transparency.

Table 5.3 suggests that there is still high primary electron loss in the 5R trimmed condition despite figure 5.13 showing low primary electron densities along the anode walls. It is suspected that the primary electrons are being collected by the ceramic filament holder and the cathode surface upstream. Despite the 25 V discharge and the plasma potential of ~28 V at the filament, the sample EEDF shown in figure 4.7c seems to indicate the presence primary electrons with energies greater than what could be obtained by electrostatic acceleration through the filament sheath. This anomalously high energy primary population, which is outside the error of the analysis, would be able to overcome the negative-going sheath at upstream cathode surface. Although unsubstantiated in this experiment, it has

been shown that a bump-on-tail two-stream instability can lead to phase-space oscillation of the non-collisional beam (primary) electrons [19, 65]. This would cause an energy spread to the primary population while the calculated volume averaged primary electron energy is at a reasonable 21 eV.

5.2.4 4R Configuration

The 4R configuration was the first iteration after the 5R configuration, designed to radially expand the center-line plasma towards the grid plane to achieve better beam flatness. The bulk axial magnetic field is maintained but designed to diverge downstream with a null region near the grid plane. The furthest downstream ring-cusp is necessary to define the bulk plasma boundary and an isolated electrode was installed to prevents loss of primary electrons to the cusp. As previously stated, the performance data from figure 5.11 shows that this configuration was able to achieve the highest ion current to the grid plane at a given discharge power compared to the 3R and 5R configuration. The segmented electrode at cathode potential was crucial to the high performance of the 4R discharge; biasing it to anode potential led to performance values more similar to the 3R configuration. An additional trim field of ∼50 Gauss was also necessary to reach peak simulated performance. The coils pushed the null region past the extraction plane for a flatter beam profile, similar to the mechanism found in the 3R discharge.

Figure 5.17 reveals that the plasma potential suddenly falls approaching the extraction plane. This plasma structure made it impossible to extract the other plasma parameters

Configuration	P_d	P_{ion}	P_{ex}	P_{spz}	P_{th}	P_{wall}
3R Default	6 W	0.84	0.84	0.42	1.62	2.70
5R w/o Coils	6 W	0.48	0.48	0.24	0.93	4.11
5R w/ Coils	6 W	0.84	0.78	0.66	1.63	3.46

Table 5.3: Breakdown of the estimated primary electron power loss mechanisms. The Sptizer term (P_{spz}) is also included into the power loss to thermalization (P_{th}).

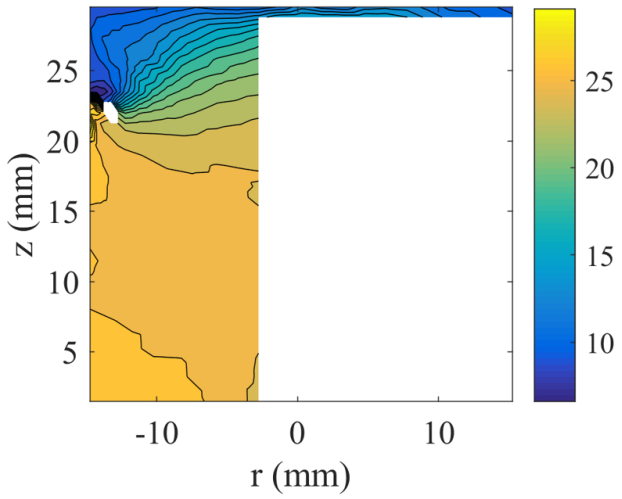

Figure 5.17: Plasma potential map of the 4R configuration. The segmented downstream electrodes leads to a internal axial electrostatic field that accelerates the ions from the bulk region to the extraction plane.

from the Langmuir probe sweep. The potential drop was accompanied by a sudden decrease of electron temperature, reducing the voltage resolution of the data. The established electric field would lead to a spatially dependent accelerated ion population that alters the $I - V$ sweep in an unaccountable manner. The plasma potential delineation was a result of the cathode-biased isolated ring electrode and the predominately radial magnetic fields. All magnetic field lines downstream of the null region were bounded by cathode bias surfaces that inherently confines the electrons. Therefore, an electric field must be established in order to transport the ions across the field lines to maintain relative quasi-neutrality. The radially dependent ion velocity distribution could dramatically affect the extraction characteristic of the ion optics as they were designed for low-temperature isotropic ions. The accelerated ions may have led to impingement of the ion beam against the accelerator grids, causing uneven grid erosion and reduce thruster lifetime.

5.3 Chapter Summary

The performance and discharge mapping measurements presented in this chapter provided crucial insight into the discharge behavior of miniature DC ion thrusters. Simulated performance measurements of the original MiXI thruster were similar to those obtained through beam extracted measurements. Comparison between the performance data for discharge design with poorly and well-confined primary electrons revealed performance trends that can be used to rapidly assess the various magnetic field configurations. The newly implemented discharge mapping technique allows researchers to resolve and understand the plasma structure of miniature cusp devices with unprecedented speed and accuracy.

The discharge maps for all tested configurations show that the entire plasma structure is governed by magnetic field topology and that the discharge design is limited to topologies that would allow for uniform beam extraction. The results for the default 3R configuration confirmed previous descriptions on the nature of the MiXI thruter's discharge plasma. For example, the high loss of primary electrons limits the energy transferred to the plasma electrons and ions are exclusively generated from direct primary electron ionization.

Findings from the 5R configuration indicated that it was possible to better confine the primary electrons in a miniature discharge without encountering the discharge stability tradeoff that has traditionally been considered a driving limitation of ring-cusp ion thruster design. The 4R configuration expanded on findings from the 5R configuration and demonstrated very promising improvements to the discharge performance. The use of a isolated ring electrode was found to be an effective approach at mitigating the primary electron lost at the cusp but also lead to an undesirable electric fields within the internal plasma that must be considered in future iterations.

5.3.1 Miniaturization Challenges

The results and analysis in this chapter ultimately led to a better understand of the plasma behavior and the design difficulties of miniature-scale discharges. The following is a discussion of the key challenges with miniaturization:

1. The radially magnetized ring-magnets that are arranged around the cylindrical walls inherently generate strong magnetic field gradients along the radial direction. This usually results in a strong plasma density gradient along the extraction place that can be detrimental to the thruster's performance and lifetimes. This effect was mitigated in the 3R configuration through alignment of the cusp structure with the extraction plane.

2. It was found that almost any ring-cusp directly exposed to the plasma will lead to high primary electron loss to the walls. Even if the discharge can be configured in a 2-ring configuration with the demagnetized NSTAR permanent magnets, conservative probabilistic loss calculations still indicates that 40% of the primary electrons will be lost directly to the chamber walls.

3. Attempts to increase the permanent magnet field strength for the MiXI 3R configuration to improve the primary electron confinement led to lower performance values. High discharge voltages were required to extract any meaningful discharge current from the filament within a reasonable heater power.

Although each of these challenges can be addressed individually, the challenge remains to address all three challenges with a single design. The main scaling limitation of conventional ring-cusp discharges is that the primary and plasma electrons are collected at the same cusps, which requires that miniature discharge must carefully consider the stability vs. efficiency trade-off discussed in section 2.4. The results from this chapter also led to methodologies and tools, such as the electrostatic "plugging" of cusps (similar to a Kaufmann of Magneto-Electrostatic design), that can be used to better confine both electron species. Each of the

tested configurations demonstrated important insight for a new discharge design that can address the challenges listed above.

CHAPTER 6

Axial Ring-Cusp Hybrid (ARCH) Discharge

The knowledge and experience gained from testing several discharge configurations, along with the insight into the plasma behavior of each design, led to the development of the Axial Ring-Cusp Hybrid (ARCH) discharge concept. Traditional ring-cusp design principles have an inherent design limitations at the miniature-scale because cusp fields dominated discharge and more importantly, the plasma and primary electrons loss are indelibly coupled. This chapter details the design and approach of the ARCH discharge. The same performance and discharge map measurements outlined in the previous chapter were acquired and analyzed. These results show a significant improvement to the discharge performance and internal plasma properties where both are more similar to efficient conventional-scale ion thrusters.

6.1 ARCH Discharge

The ARCH discharge is a design concept that combines the advantages of conventional Kuafmann and ring-cusp magnetic field design in a manner that is particularly effective for smaller-scale DC discharges. Figures 6.1 and 6.7 show that the magnetic field lines and the discharge plasma of this device resemble an arch structure. The "axial ring-cusp" part of the acronym refers to placement and magnetization of the permanent magnets while the "hybrid" refers to the mechanism in which the discharge current is collected. There are 3 key aspects to the ARCH discharge design which addresses all of the miniaturization challenges discussed in section 5.3.1:

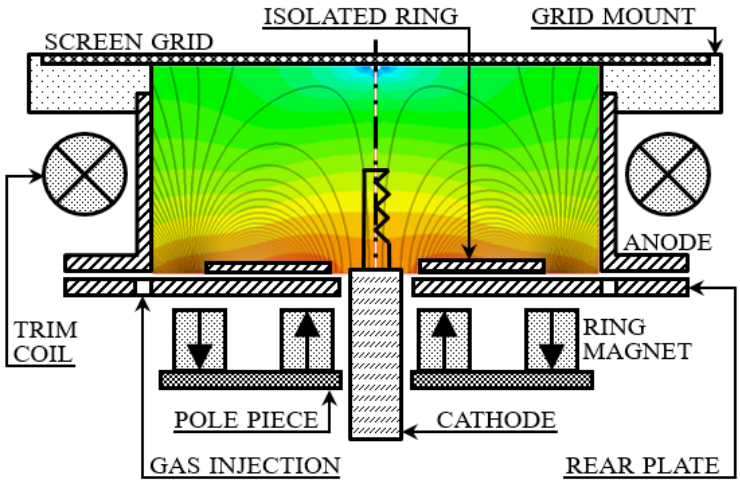

Figure 6.1: Diagram of the 3 cm diameter ARCH discharge with the key components labeled and overlaid onto the magnetic field contour (in logarithmic scale).

1. The permanent ring magnets are positioned upstream of the discharge chamber and magnetized in the axial direction. The same principle can also be accomplished with a different magnet configurations but the overall principle is a strong negative magnetic field gradient in the downstream axial direction. In this way, the design provides a low and uniform magnetic field strength across the entire extraction plane.

2. The concentric ring-cusps both terminate at an electrode that is biased ∼5 V below cathode potential. The non-collisional primary electrons are electrostatically confined at both ends of the arch-shaped fields and are also unable to diffuse across the edge field lines to reach the anode. In addition, the center-line injected primaries are easily distributed in the radial direction by the highly divergent inner-cusp magnetic field. The segmented electrode was demonstrated to be a useful tool in the 4R configuration for preventing primary electron loss to ring-cusps that were exposed to the bulk plasma.

3. The anode is shielded by an edge magnetic field that runs parallel to the cylindrical wall, avoiding direct leak paths for the primary electrons. The weak to moderate field strength and the short diffusion path length allows the collisional plasma electrons to be collected at the anode. The diffusion rate increases with the plasma density and

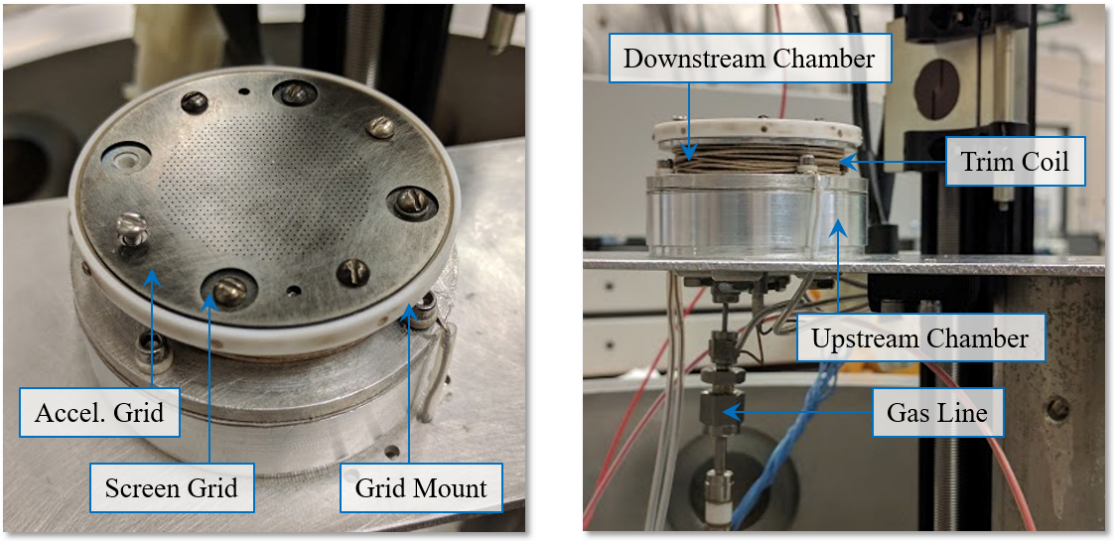

Figure 6.2: Images of the ARCH discharge prototype. Left: the MiXI ion optics and grid mount are used for the simulated ion thruster testing. Right: the rear plate separates the upstream magnet chamber and downstream discharge chamber.

the device can extract a wide range of discharge currents at low discharge voltages. This confinement mechanism was first demonstrated with the 5R and later the 4R configuration where the trim coil fields were used to shield to anode from the bulk plasma.

6.1.1 Prototype Design

The ARCH discharge prototype shown in figure 6.2 was designed as a test platform for a new cusp confinement approached based on results from the previous chapters. The design allowed for easy adjustments of key features: the discharge chamber height, the placement of the ring magnets, and the location and type of cathode used. The discharge chamber was kept at 3 cm in diameter to use MiXI's grid system and for baseline comparison with the MiXI discharge. Therefore, performance measurements and the discharge maps were acquired using the same extraction grids and probing grids from the MiXi testing. The electron source was the same 5 mil tungsten filament cathode that typically operates between

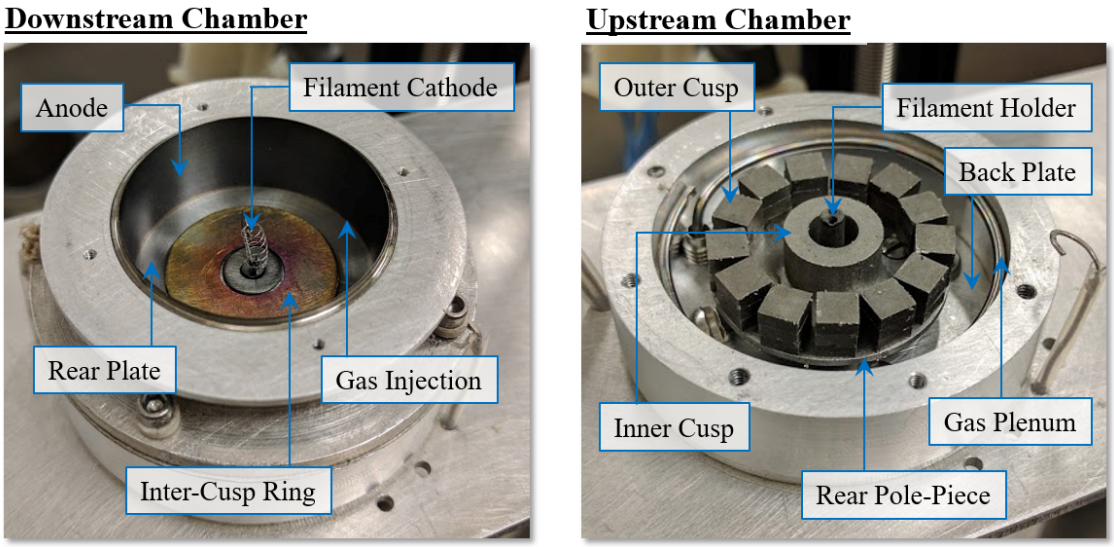

Figure 6.3: Images showing the internals of the upstream and downstream chambers. The downstream discharge chamber surfaces are stainless steel to reduce erosion while the upstream magnet chamber is mostly aluminum for better thermal conduction.

18 to 25 W of heater power.

The test platform featured an upper and lower chamber where the propellant was injected and ejected, respectively. The lower chamber walls were machined from aluminum as they were not in contact with the plasma and the material has good thermal conductivity. This chamber contains the magnet assembly that was mounted to the back plate where the proximity of cusp to the discharge chamber was adjusted using spacers of various lengths. The permanent magnets were sufficiently attracted to the steel pole piece and attached without the need of additional mounts. The height of the lower chamber was roughly chosen to accommodate the miniature hollow cathodes designed for the MiXI thruster; the exact axial position of the cathode orifice can be adjusted by using ring spacers. Neutral gas was injected through a ring plenum that jetted gas in an inward radial direction at discrete azimuthal locations.

The upper chamber contained the discharge plasma and was fabricated using stainless steel because of the higher temperature limits and lower sputter yield of the material. The upstream surface of the discharge chamber (rear plate) featured 8 gas ports underneath the

cylindrical walls for a uniform and predominately radial gas injection. For easy adjustability, the upper chamber was composed of 2 parts: the cylindrical anode wall with an outer lip at the bottom and the collar mount. The upper chamber, rear plate, and lower chamber were all electrostatically isolated using a 0.2 mm Kapton semi-conducting sheet. The insulator was recessed between the upper chamber and rear plate to create a "shadow shield" to prevent local electric arcs as well as to accommodate the gas injection ports. High temperature trim coils with fiberglass insulation were wrapped directly around the discharge chamber and operated more efficiently due to their proximity. Lastly. thermocouples were attached to the rear plate and the upper chamber collar mount.

In the most recent iteration, there was also a stainless steel isolated inter-cusp ring in between the two concentric ring-cusps that prevent a "short-circuiting" in the upstream direction that is later explained in section 6.2.3. The ring has a 24 mm outer and 8 mm inner diameter that were sized based on the initial discharge map results shown in figure 6.9. The ring was meant to span the entire inter-cusp region without extending into the bulk discharge and collecting the primary electrons. Currently, the ring is only gravity mounted, placed on top of a thin Mica insulating sheet.

An advantage of ARCH design is that the discharge current was collected only at the cylindrical walls which was electrically and thermally isolated from the rear plate. During normal operation with 20 W heater power and 15 W discharge power, the cylindrical walls reaches a temperature of up to 380°C while the rear plate remains below 200°C. In addition, the permanent magnets were not in contact with the rear plate and there should be minimal heater power when the filament cathode is replaced with a hollow cathode for thruster operation. Therefore, the ARCH discharge should be able to operate at relatively high discharge power without the risk of demagnetization of the permanent magnets.

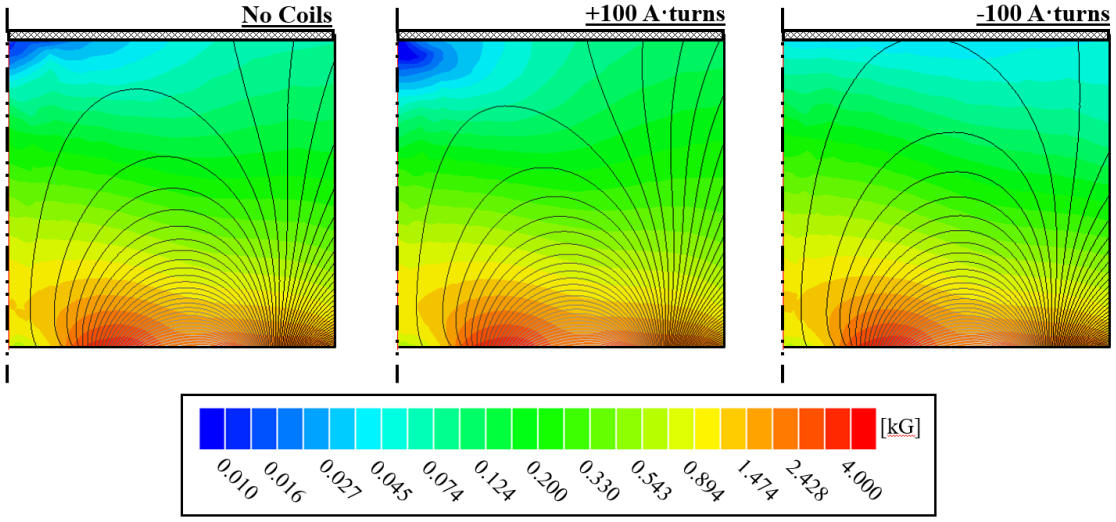

Figure 6.4: The magnetic field contours and lines for the ARCH V0 discharge at a range of trim coil currents. The trim fields strongly effect the plasma structure near the extraction plane and the plasma electron confinement across the edge fields that shields the anode.

6.1.2 Magnetic Field Configuration

The magnetic fields in conventional ring-cusp ion thrusters must be configured to attain a sufficient primary electron confinement path length — a criterion that is directly proportional to the discharge chamber volume and aspect ratio. In the ARCH discharge, the primary electron confinement was relatively independent of the effective plasma volume. Therefore, the chamber was designed to concentrate the ionization region near and evenly across the extraction plane. Increasing the discharge volume reduces the electron temperature. For a given beam current, the ion generation would be more spatially distributed which would reduce the local electron energy density. The lower loss rates associated with the lower electron temperature may or may not have a net benefit with the greater surface area of the discharge chamber. Therefore, the ARCH chamber dimensions can be instead driven by the desired beam current and the shape of the magnetic fields for the available permanent magnets.

The magnetic field contours for the ARCH discharge at a range trim coil currents are

shown in figure 6.4. They are computationally generated but have been verified through Gaussmeter measurements at various trim coil currents. The inner ring-cusp uses the same axially magnetized, continuous ring magnets from the MiXI thruster. The outer ring-cusp was composed from 5 mm $\times$ 5 mm block magnets, positioned as diagrammed in figure 6.3 and oppositely polarized in relation to the inner-cusp. The block magnets allowed for simple adjustments of the outer-ring cusp dimensions without the need to fabricate several custom ring magnets. However, the azimuthal gaps within the ring-cusp meant that several iterations using a Gaussmeter were required to obtain the desired magnetic field topology since the version of Ansoft MAXWELL used only allowed for 2D axisymmetric simulation. The inner and outer ring cusp were configured to obtain an inter-cusp field lines of roughly constant curvature. In addition, the outer-cusp was adjusted to obtain axial fields of 60 to 100 G near the upper portion of cylindrical walls. These are approximate axial field values were found to achieve the best discharge efficiencies in the MiXI 4R and 5R configuration. The ring magnets was spaced about 1 mm upstream of the rear plate to position the magnetic null region at the grid plane.

The weak magnetic fields near the extraction plane in conjunction with the close proximity of the trim coils allowed the performance to be efficiently tuned. The simulated magnetic field contours, shown in figure 6.4, illustrates how less than a couple watts of coil power can have large affect the field topology. The results show that increasing the edge fields will improve the plasma electron confinement but will lead to poorer beam uniformity as it also pushes the cusp field structures radially inward. Reversing the trim current will reduce the near-wall fields and will start to pull the null region radially outwards and towards the outer-cusp. This can potentially lead to semi-direct leak path to the anode wall and thus, significant primary and plasma electron loss.

6.1.3 Discharge Start-Up

The ARCH discharge required a start-up procedure to light the discharge plasma since there was no direct anode path at the nominal operating condition. The MiXI 4R and 5R configuration both operated in the lossy configuration by default and required the axial trim fields to obscure the leak area to reach peak efficiency. However, the shielded anode in the ARCH discharge is generated by the strong outer-ring cusp that cannot be reasonably canceled with the trim coils. There were currently two methods known to reliably light the discharge plasma:

1. The first method was to first biased the anode to >30 V at a typical operating flow rate. The rear plate was then biased positively towards ∼25 V or until a discharge current is measured at the anode, indicating the presence of plasma. Afterward, the rear plate was bias back down to sub-cathode potential and the anode to a nominal operating voltage. The filament heater was then adjusted to obtain the desired discharge current.

2. The second method required a rear plate bias to the nominal discharge voltage. It was found that suddenly powering the trim coils, regardless of the steady-state current settings, would strike the discharge. The process only worked when the resulting magnetic field change is in a specific direction. Therefore, it is suspected that an induced electro-motive force (EMF) in the azimuthal direction was generated by the time-varying coil fields. The azimuthal electric fields would have then generated an $E \times B$ drift across the predominately radial magnetic fields and towards the rear-plate.

6.2 Results & Discussion

The ARCH discharge was tested at the same discharge conditions as the MiXI 3R discharge with the discharge voltage, screen grid, and accelerator grid biased to 25 V, -10 V, and -20 V, respectively. Unless stated otherwise, the discharge voltage was kept at 25 V

for all tested conditions despite better performance at higher voltages. Measurements were acquired once the discharge performance stabilized when thermal equilibrium was reached. The results of two iterations of the ARCH discharge is presented in this chapter:

1. ARCH V0: The first tested configuration was without the isolated inter-cusp ring. A slight trim field was required to reach peak efficiency at the expense of a slight reduction to the beam flatness.

2. ARCH V1: The inter-cusp ring was installed to reduce upstream ion loss. The outer ring-cusp was strengthened to increase the edge fields based on the optimal trim condition of the ARCH V0 discharge. The discharge operated at peak efficiency without additional trim fields.

6.2.1 Performance Data

The simulated performance data for the ARCH V1 configuration at a range of specified flow rates and discharge voltage are shown in figure 6.5. It should again be noted that the total efficiency does not include many important factors previously discussed in section 5.2.1 — the total efficiency only serves as a comparison metric with the MiXI thruster. Regardless, these results indicate that the ARCH V1 discharge was able to achieve a discharge performance on par with efficient conventional-scale ion thruster discharges.

Besides the higher performance, the overall trend in figure 6.5 are very similar to the 4R configuration shown in figure 5.11. All aspects of the performance are shown to increase with higher discharge voltages — a previously discussed characteristic of a well-confined discharge design. Increasing the specified flow rate is again shown to improve the total efficiency at higher beam currents due to the simulated operation. Figure 5.11b shows the same trend as the 4R performance data where the slope for different specified flow rates all have similar slopes at lower discharge currents — an indication of the high primary electron confinement. However, the slopes in the 4R configuration does appear to coincide close together compared

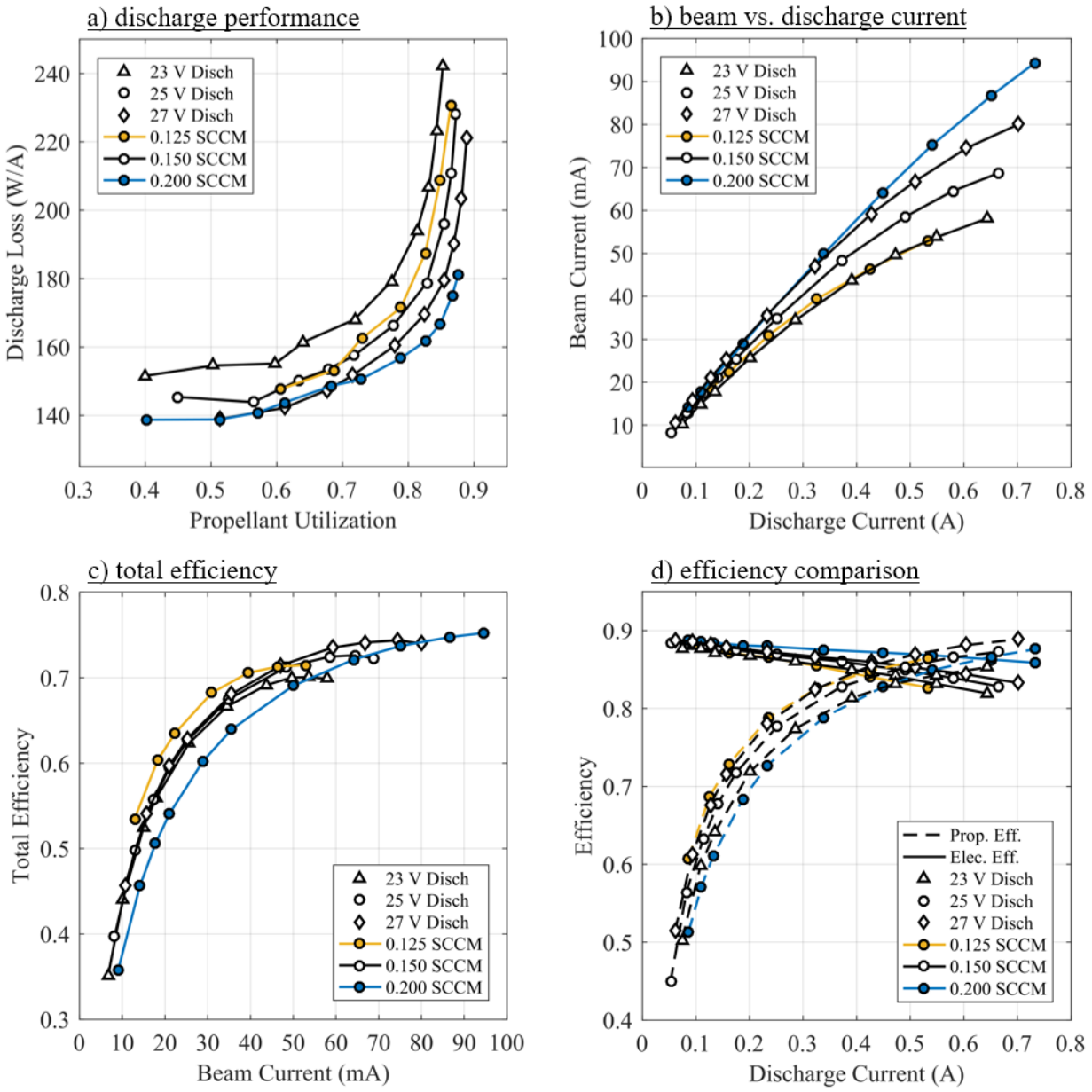

Figure 6.5: Performance assessment of the ARCH discharge at a range of discharge voltages and base neutral gas flow rates. The curves were generated by adjusting the heater power to increase the discharge current while keeping all other power supplies constant. Red circle represents the discharge condition shown in table 5.1.

to the ARCH V1 discharge, particularly between the 0.150 SCCM and 0.200 SCCM curves. Although not presented here, these curves were seen to coincide much closer together for the ARCH V0 data which did not have the isolated inter-cusp ring. It is probable that the inter-cusp ring was collecting a small fraction of the primary electrons due to misalignment and/or improper sizing of the ring.

The ARCH V1 discharge exhibited better performance compared to the 4R discharge despite the slightly lower primary electron confinement because of better ion and plasma electron confinement. Although the discharge map analysis is unavailable, figure 5.6 shows a relatively weak axial field that was shielding the two middle ring-cusps from the bulk plasma. Figure 6.5b shows that at 0.5 A of discharge current, the ARCH data exhibited a 20% increase to the beam current between a 23 V and 25 V discharge. The MiXI 4R discharge exhibited only a 20% increase for the same operating conditions. The difference is also reflected in figure 6.5d where increasing the discharge voltage raises the electrical efficiency in the ARCH V1 but not the 4R discharge.

Figure 6.6 is a comparison between the default MiXI 3R discharge and the various iterations and conditions of the ARCH discharge for a 25 V discharge and 0.140 or 0.150 SCCM specified flow rate. The red dot is the MiXI thruster's performance point shown in table 5.1. The ARCH V0 was the first iteration without the isolated inter-cusp ring and required 1.5 W of trim coil power to reach peak efficiency. The ARCH V1 included the inter-cusp ring and an optimized cusp field to where the trim coils are unnecessary. The ARCH V1 cold is the performance curve measured at standard ion thruster operating temperature of $150 - 200°C$, before the anode reached thermal equilibrium at $\sim 480°C$. The filament cathode accounts for approximately two-thirds of the total discharge power consumption that would be absent when operated with a hollow cathode. In addition, the prototype was only designed to manage the temperature of the permanent magnets and not the anode. The higher temperatures lead to higher neutral velocities which decrease the neutral density by 20-25% for a given specified flow rate.

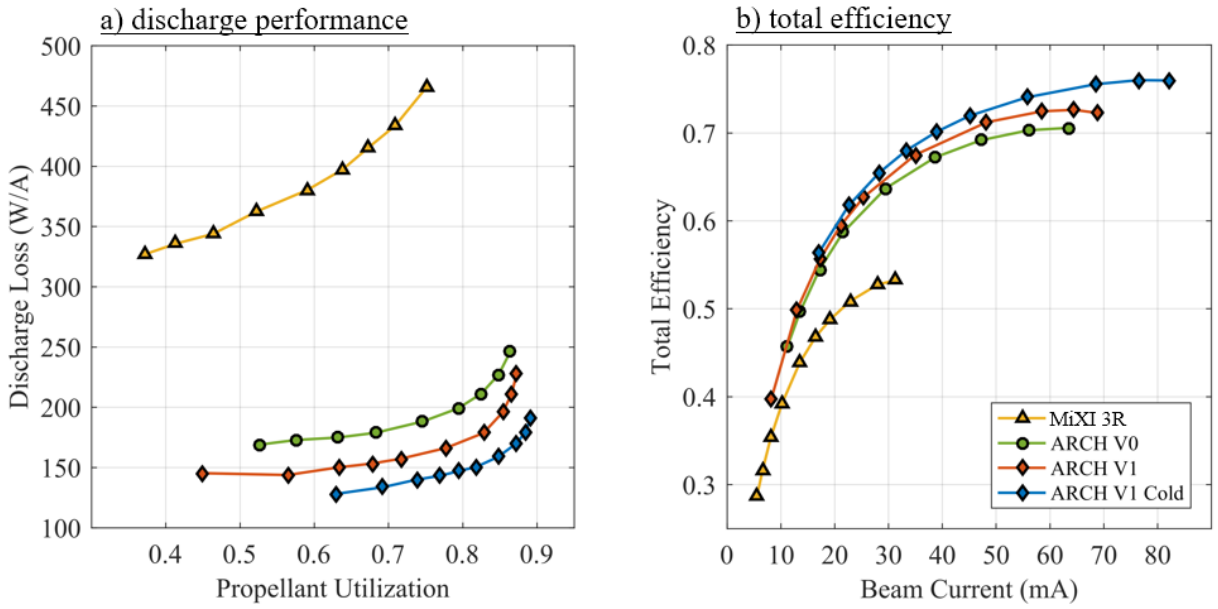

Figure 6.6: Performance comparison between multiple configurations of the ARCH discharge and the original MiXI discharge. Measurements are obtained for a 25 V discharge at 0.150 SCCM specified gas flow rate.

The beam current of the ARCH V1 discharge is currently limited by the use of the MiXI grids, which were designed for lower plasma densities and beam current densities. However, even at the 54 mA perveance limited beam current, it may be possible attain a discharge loss of under 160 eV/ion with a 0.85 propellant utilization efficiency. At the MiXI thruster's nominal operating condition shown in table 5.1, the ARCH discharge is able to produce the same beam current at less than half the discharge power or over twice the beam current at a given discharge power.

6.2.2 Discharge Map Analysis

The discharge map for ARCH V1 discharge are shown in figure 6.7, operating at 0.35 A discharge current and 0.150 SCCM specified flow rate. The average neutral density of approximately 2×10^{19} m^{-3} is based on a control volume calculations between the specified flow rate and the total open area of the grids. Overall, the discharge map reveals that the

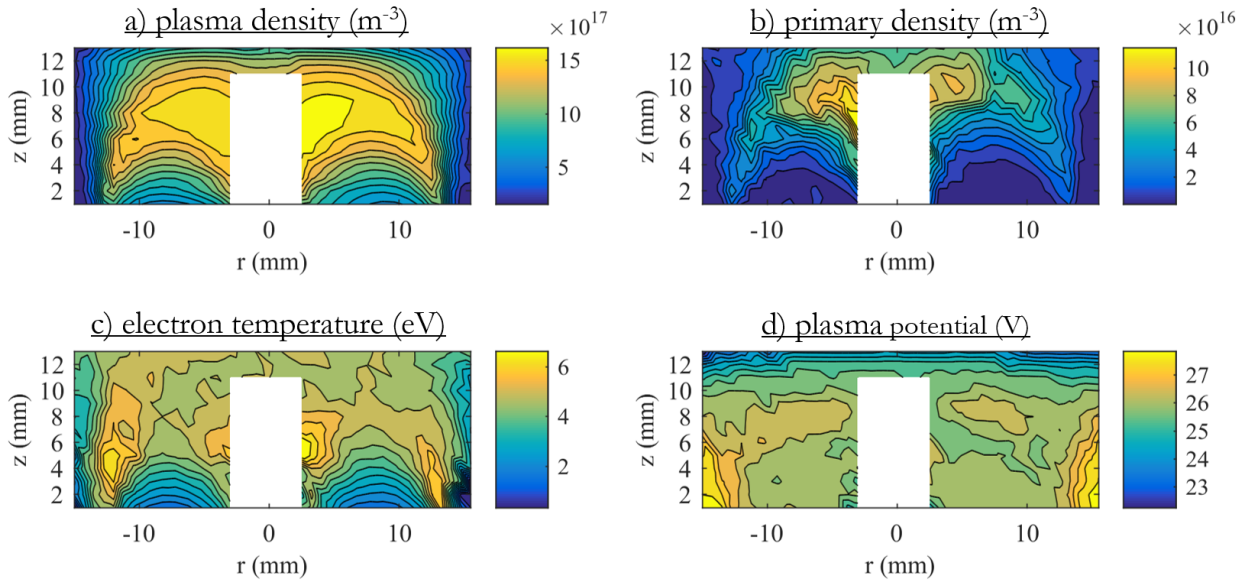

Figure 6.7: Plasma parameter maps for the ARCH V1 discharge for a 25 V, 0.35 A discharge and 0.150 SCCM specified flow rate. The cross-section map of the plasma density resembles a double arch structure. Note: the electron temperature values are elevated near the cusps due to the probe's orientation to the magnetic field.

improved performance is not impaired by poor beam uniformity such as with the 5R trimmed configuration.

Similar to the 3R discharge maps, the primary electron contour resembles an internal frame of the plasma electron distribution. The density maps exhibit a double arch-like structure that correlates with the magnetic fields shape. The electron temperature ranges between 4 to 6 eV and exhibits a more gradual delineation compare to the density contours. The plasma potential is by and large uniform at $\sim$ 26 V relative to the cathode potential within the entire discharge chamber. In addition, the potential profile shows that the cathode biased cusp at does not lead to an internal electric field such as with the 4R configuration.

Overall, the discharge maps show that the plasma is well-confined and verifies the simulated performance measurements. The plasma and primary electron are well distributed along and near the extraction plane for efficient ion generation. The primary electron density contour shows that the population are well-confined to the arch-shaped field lines; they

easily diverge from the on-axis discharge cathode and are also unable to diffuse across the axial fields to the anode. At the outer ring-cusp, the primary electron lost width is on the order of their Larmor radius. In the bulk region, they are seen to have a toroidal or doughnut-like spatial distribution where the peak density is slightly off-axis — a formation that is favorable for efficient ion generation as the radial location corresponds to a larger grid area. The strong radial plasma density gradient towards the anode walls confirms that the weak to moderate axial fields provides sufficient confinement. The plasma electrons are able to diffuse across the magnetic field lines to the anode where the entire discharge current to be collected at relatively low discharge voltage.

The electron temperature has the expected iso-thermal distribution along the magnetic field lines. The high electron temperature is an indication of good primary electron confinement as most of the discharge energy is deposited into the plasma through ionization or thermalization collisions rather than lost to the walls. In addition, the primary electron and temperature distributions are not localized to the center-line region that would lead to local neutral depletion and high double-ion generation, such as in the NSTAR thruster [12]. It should be noted that the electron temperature values are most likely artificially elevated near the cusp region due to errors in the probe analysis. The vertical orientation of the Langmuir probe in this region was parallel to the strong cusp magnetic field lines. This suppresses the electron collection in this region and a more advance theory would be required to more accurately resolve the temperature. In between the ring-cusps, the probe was oriented perpendicular to the field lines; the values here are a more accurate representation of the electron temperature along the field lines.

The low plasma potential in comparison to the electron temperature indicates a small sheath potential where the ion and plasma electron loss are well balanced and most of the collected discharge current are the low-energy plasma electrons. Coupled with the low electron temperature along the anode, the net effect is a minimization of the plasma electron power loss to the walls from extracting the discharge current.

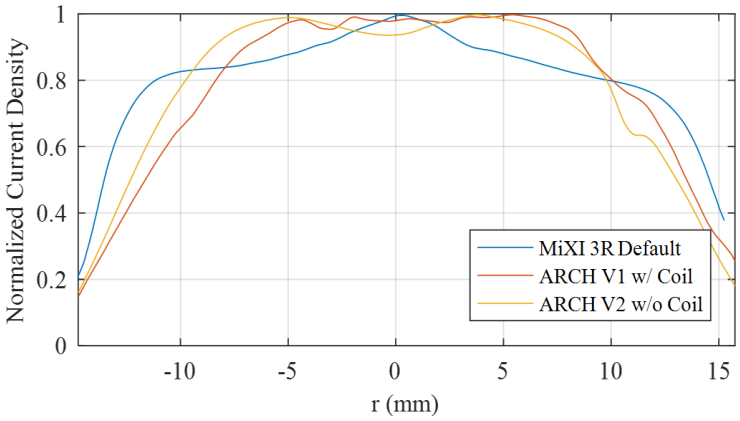

Figure 6.8: Normalized beam current profile, estimated from the plasma conditions measured near the exit plane of the discharge. Note: the beam current estimates are based on an ion transparency of 75% was assumed across the grid plane and grid perveance considerations are not included.

Figure 6.8 shows a comparison of the projected normalized beam profile, calculated from the plasma density and electron temperature values along the extraction plane. The MiXI thruster had a notably flat beam profile even when compared to much large ion thrusters. The ARCH thruster features a slightly dipped beam profile and an estimated beam flatness of 0.66. Although slighty worse than the MiXI thruster, it is still on par with most conventional-scale ion thrusters.

6.2.3 Inter-Cusp Diffusion

Figure 6.9 shows the discharge map for the ARCH V0 that did not include the isolated inter-cusp ring. Although very similar to the ARCH V1 discharge maps, there was higher than expected ion loss measured at the upstream rear plate. Figure 6.9a shows that the plasma density at the upstream surface is comparable to those near the extraction plane despite the order or magnitudes greater magnetic field strength upstream. In contrast, the radial inter-cusp region in the MiXI 3R discharge has approximately the same field strength and does not exhibit such a high plasma density. Figure 6.9b shows negligible primary electron population and figure 6.9c shows that the plasma electrons are at low temperatures

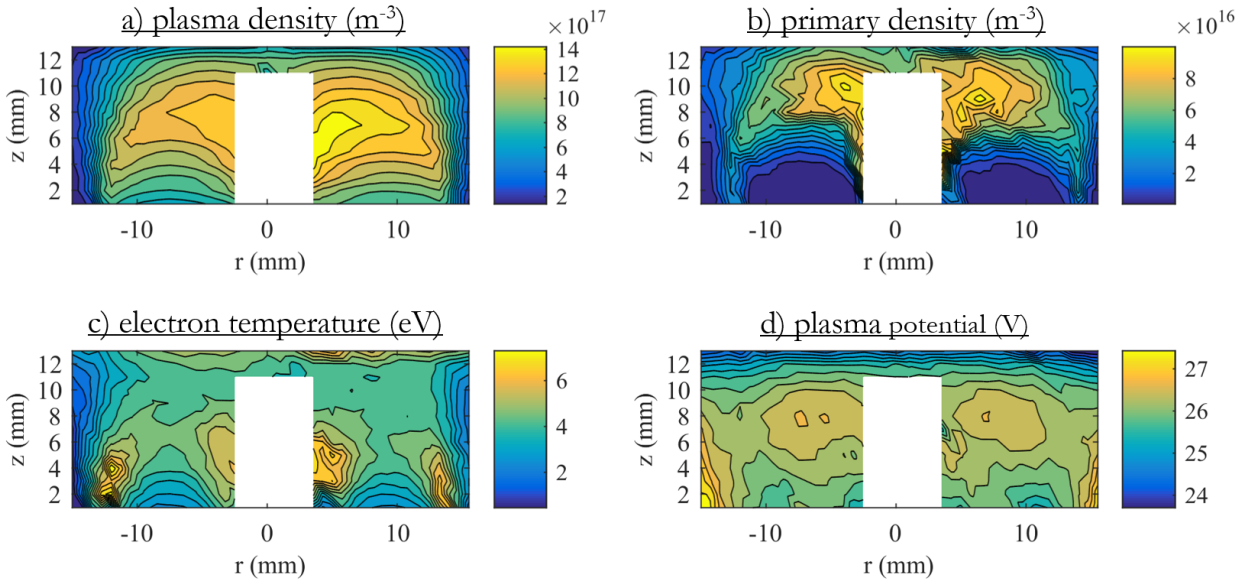

Figure 6.9: Plasma parameter maps for the ARCH V0 discharge without additional trim fields, operating at 25 V, 0.35 A discharge and 0.150 SCCM specified flow rate. Compared to figure 6.7, there is relatively high plasma density within the inter-cusp region.

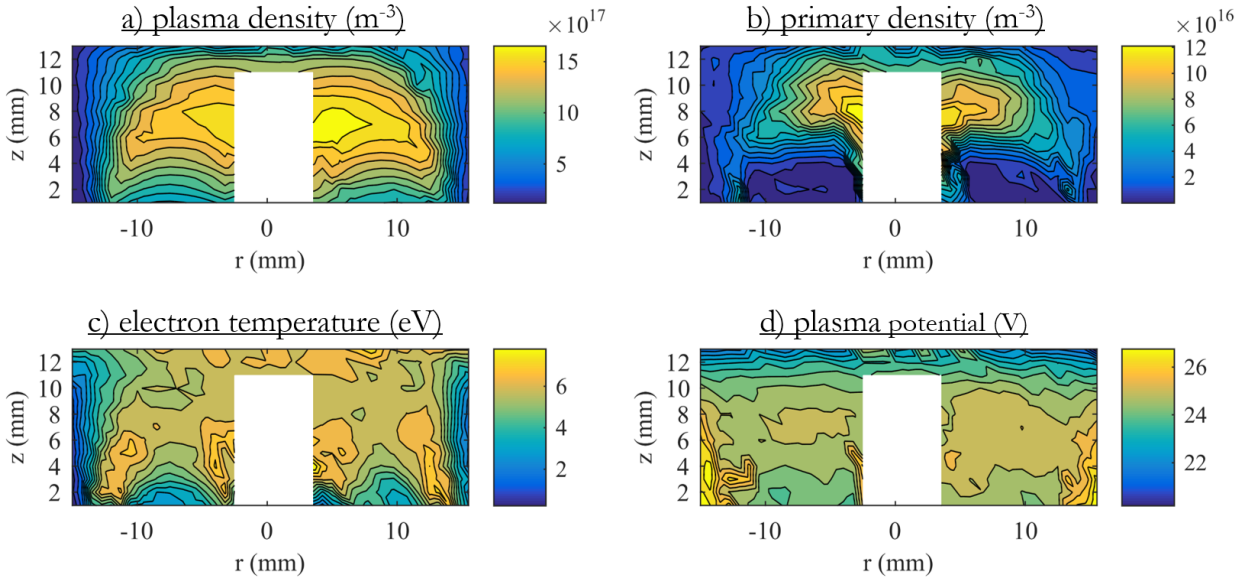

Figure 6.10: Plasma parameter maps for the ARCH V0 discharge with +1.0 A of trim coil field, operating at the same discharge condition as figure 6.9. There is higher plasma density and electron temperature due to improved plasma electron confinement.

within this region. Therefore, the plasma within the inter-cusp region must have diffused across the strong cusp magnetic fields from the bulk generation region.

Generally, the magnetic fields inhibit the transport of the unmagnetized ion population through ambipolar interaction with the confined plasma electron population. Without the inter-cusp ring, all the magnetic field lines within the inter-cusp region terminated at a surface below cathode potential. Any electrons that will eventually diffuse into this region are indefinitely confined between the two ring-cusps. In order to maintain quasi-neutrality within this region, there must exist a self-consistent electric field that opposes the density-gradient driven electron diffusion. This is evident in figure 6.9d, which shows a net negative electric field in the upstream direction and away from the bulk plasma. This electric field is also responsible for the upstream extraction of the ion population from the bulk generation region at a rate faster than if inter-cusp fields were absent all together, a behavior that is typically attributed to the "Simon short-circuit" effect [66].

The plasma potential contour also shows a slight radial electric field in the outward radial direction past the region of peak plasma density. Similarly, the axial magnetic fields in this region also terminated at cathode biased surfaces at both ends. The field lines at $r > 12$ mm then begins to intersect with the cylindrical walls which are at anode potential. Plasma electrons that eventually diffuse to these field lines are no longer confined and are readily collected as the discharge current. Therefore, the plasma potential profile shows a sudden inward radial electric field near the anode walls that exists to instead repel ions and pull in the electrons across the axial magnetic field.

The isolated inter-cusp ring at the minimum, ensures global ambipolar diffusion within the inter-cusp region. Although an insulating ring would enforce local ambi-polarity, it would also eventually be coated by sputterants and the evaporating filament. The ring is carefully sized to not extend into the actually cusp area to avoid collecting the primary electrons. Figure 6.7d shows that the upstream electric field is weakened with the inter-cusp ring. The plasma density is also much lower within the region and the overall distribution appears to

be pushed further towards the extraction plane.

6.2.4 ARCH V0 Trim Field

Figure 6.10 shows the discharge map of the ARCH V0 with trim fields. The improved performance data was a result of higher bulk plasma density despite the plasma density distribution being squeezed slightly more inwards, reducing the beam flatness. The primary electrons contour is also narrower and the toroidal shape is replace by a more disk-like distribution. This feature is reflected in projected beam profile with the trim fields, shown in figure 6.8, where the center-line dip is now absent. The performance data suggests high primary confinement in both the trimmed and untrimmed conditions. Despite the stronger magnetic fields, both maps show very similar primary electron density values and shape for the same discharge conditions.

Figure 6.10d shows a noticeably lower plasma potential with the trim fields to where the average bulk value is approximately 25 V. The 1.0 A trim coil setting was chosen as it attained the highest total efficiency for the given discharge condition. It is not by coincidence that the resulting magnetic field corresponds to a bulk plasma potential that is equal to the discharge voltage. In addition, Figure 6.10c shows that there is also a 20% increase to the electron temperature. Because of the nature of the Maxwellian distribution, the $\sim$1 eV difference translates into a large increase to the higher energy tail population that is responsible for a sizable portion of the ionization in a well-confined discharge.

6.2.4.1 Plasma Generation and Loss Analysis

The singly and doubly-charged ion generation rate contour maps are shown side-by-side in figure 6.11. The primary electron excitation and thermalization contour maps are shown in figure 6.12. The volume averaged rates are tabulated on table 6.1 and table 6.2. These analyzes are expected to possibly have high errors due to the issues outlined in section 5.2.3.

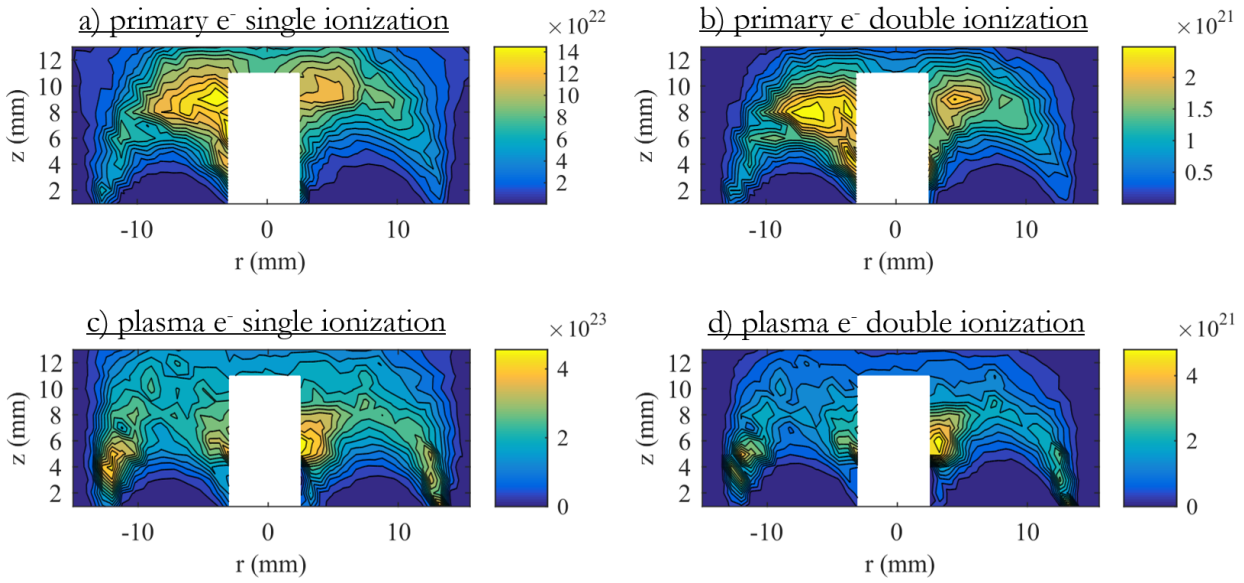

Figure 6.11: Contour map of the local reaction rates ($m^{-3} \cdot s^{-1}$) for singly and doubly-charge ion generation through ionization collision by primary and plasma electrons. The ionization rate from plasma electrons are exaggerated due to the elevated electron temperature obtain from the probe analysis.

Regardless, the following results are still informative for relative comparison between the various interactions.

Similar to conventional ion thrusters and in contrast with the MiXI thruster, the ionization contours show that a sizable portion of the ions are generated from the high-energy tail of the Maxwellian plasma electron population. Very few primary electrons are lost to the walls and they are more likely to thermalize with the plasma electrons rather than encounter an ionization collision due to the higher plasma-to-neutral density ratio. This is evident in the thermalization rates shown in figure 6.12b and the total primary electron power loss to thermalization in table 6.2. Therefore, more of the discharge energy is deposited into the plasma electrons population, increasing the electron temperature and thus, the plasma electron ionization. The excitation rates are similar to the ionization rates due of their similar cross-sections and interacting particles.

Table 6.1 shows an unrealistic volume averaged rate for ionization by plasma electrons

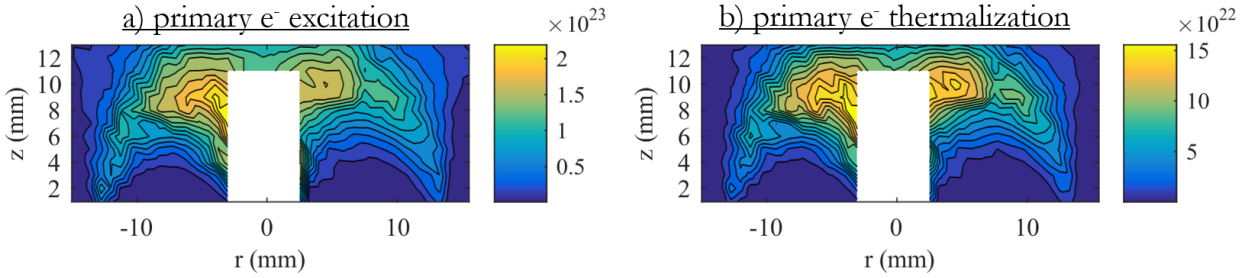

Figure 6.12: Contour map of the local reaction or loss rates ($m^{-3} \cdot s^{-1}$) for the primary electrons through excitation and thermalization. The primary electron loss rates for ionization collisions is identical to the ion generation rate in figure 6.11.

as it would account for ∼40% of the total input power of the primary electrons. The overestimation is a result of the elevated electron temperature previously discussed, particularly at the outer ring-cusp which accounts for most of the volume. The ionization reaction rate values more than doubles between an electron temperature of 4 and 5 eV.

Figure 6.11 shows that the doubly-charged ion generation rate is only ∼1% of total ion generation rate. Although this ratio is higher than the results for the 3R discharge it is still much lower than most conventional ion thrusters. The ratio of doubly-charged ions is strongly influenced by the depletion of the local neutral gas density. The neutrals are generally injected at the upstream side of discharge chamber and 80-90% of the propellant leaves the thruster as beam ions. Therefore, there is typically an overall axial gradient of the neutral density where the density is several factors lower at the grids than the region upstream. With the simulated ion thruster operation, there is effectively an additional propellant injection at the grid plane from the neutralized ions. Therefore, a proper neutral gas model is required to more accurately assess the double ion generation.

Configuration	P_p^+	P_e^+	P_p^{++}	P_e^{++}	L_{Grid}	L_{Side}	L_{Rear}	$L_{Cath.}$
3R	68.9	10.4	0.45	∼0	22.6	9.4	1.3	46.5
ARCH V1	92.1	251	1.32	1.59	63.1	24.6	29.6	22.4

Table 6.1: Ion generation (P) and loss (L) rates (mA) for the various discharge configuration. The generation terms are calculated from volume integration of the generation rates and the loss terms from surface integration using the plasma parameter maps.

Discharge	P_{pe}	L_{ion}	L_{ex}	L_{spz}	L_{th}	L_{wall}
3-Ring	6.0	0.14	0.14	0.07	1.62	2.70
ARCH V1	7.0	1.12	1.16	1.50	4.11	0.61

Table 6.2: Breakdown of the estimated primary electron power loss mechanisms. The Sptizer term (P_{spz}) is also included into the power loss to thermalization (P_{th}).

The calculated ion wall losses shown in table 6.1 confirms that there is still relatively high ion loss to the rear plate that can mitigated by replacing the isolated inter-cusp ring with an inter-cusp electrode. The ion current to the anode wall is almost 40% of the total grid current. Although not discussed in this thesis, it is also possible to reduce this current with small tweaks to the magnetic field and modifications to the grid mount assembly. The estimated total primary electron wall loss in table 6.2 is in agreement with the performance data analysis which suggested that the primary electrons are very well-confined.

6.2.4.2 Comparison

Table 6.3 reiterates the theoretical performance at 15 W discharge power for the various configurations previously discussed. These values are idealistic as they assume a grid system that is capable of 75% average ion transparency for each configuration while maintaining the same neutral transparency as the MiXI grids. The MiXI grids were designed to operate at ∼30 mA of total beam current and a theoretical maximum of 54 mA, where it encounters the perveance limit for the 3R beam profile. Although the performance data for the ARCH discharge presented in table 6.3 shows a beam current of 52 mA, the lower beam flatness

Configuration	I_b (mA)	ϵ_b	η_{ud}	η_T	F_B
MiXI 3R Default	30	480	0.75	0.53	0.73
ARCH V0 w/ Coils	48	305	0.85	0.68	0.72
ARCH V1 w/o Coils	59	190	0.86	0.73	0.66

Table 6.3: Theoretical performance comparison at 15 W discharge power. These values assume an ion and neutral transparency of 75% and 6%, respectively. Efficiency values does not include trim coil and filament heater power.

parameter would still result in beamlet currents greater than the perveance limit. However, figure 6.5 shows that the ARCH discharge can still operates with similar efficiencies at lower beam currents. The performance values also do not include the doubly-charged ion correction. Although MiXI thruster was shown to have negligible doubly-charged ion content, certain configurations tested herein operated at much higher electron temperature and therefore, double ions contributions may not be negligible.

6.3 Future Work

The ARCH V1 configuration was only the second iteration with a small tweak to the magnetic fields. The analysis of the discharge mapping result revealed ample room for further improvements to the performance with only minor changes. The ARCH design approach easily lends itself to addressing individual plasma specie confinement without severe impact to other species. The the most impactful redesign would be to increase confinement of the ions and improve the flatness of the ion beam profile. Figure 6.13 shows a second iteration of the ARCH prototype — the details of the improvements are discussed below.

6.3.1 Segmented Rear-Plate

Table 6.1 indicated that there is still high ion loss to the walls and figure 6.7d shows that there is still a slight upstream electric field extracting the ions to the rear plate. The plasma potential contours for the 3R discharge (figure 5.12) and from the RCTD (figure 4.12), strongly suggests that having the inter-cusp ring biased to anode voltage will improve ion confinement. This rear plate configuration would slightly resemble a Magneto-Electrostatic Contained Plasma Ion Thruster (MECALAC) configuration [31] where the anode is also located at the inter-cusp region in between cathode terminated ring-cusps. However, most of the discharge current will not be collected at the inter-cusp region in the ARCH discharge, but rather still at the cylindrical walls, more similar to a Kaufmann discharge.

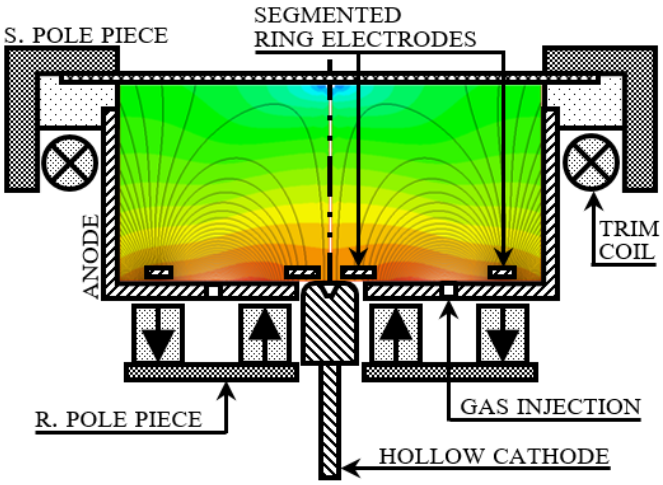

Figure 6.13: Diagram of the ARCH V2 discharge with the key components labeled and overlaid onto the magnetic field contour (in logarithmic scale).

Figure 6.13 is an inverted design to simplify the device by using a segmented electrode for the cathode cusp boundary instead. The inner and outer cathode ring can be connected together with 3 to 4 spokes across the inter-cusp region; the small total cathode area should not cause the same short circuit problem previous discussed. The inner ring electrode can also double as a hollow cathode keeper to protect the orifice plate from erosion. However, the keeper would not be able to extract electron current from the cathode during nominal operations.

6.3.2 Hollow Cathode Operation and Placement

Operation of the ARCH discharge with a hollow cathode is expected to alter the performance data and discharge maps obtained in this chapter. There will be an associated cathode sheath drop to heat the cathode insert and maintain self-heated operation. This value is generally higher on smaller hollow cathodes and will reduce the nominal energy of the primary electrons inside the discharge chamber. In addition, the electron source used for the ARCH prototype testing is a tungsten filament that is coiled to an approximate dimension of 3 mm diameter and 8 mm length. On the other hand, a miniature hollow cathode would

have a sub-mm orifice at the center-line and primary electrons injected at a single point. In traditional ion thruster designs, ring-cusp and Kaufman, plasma generated at the on-axis field lines are generally the most confined from the anode walls. In Kaufman thrusters, an on-axis injection often leads to a poor beam profile, high discharge voltage, and/or $E \times B$ driven instabilities. However, the concentric axial ring-cusps design in the ARCH discharge generates a field topology where electrons injected near center-line are the least confined. As shown in figure 6.1, the near on-axis field lines diverges furthest in the radial direction and into the center of the outer ring-cusp. With the filament cathode, the primary electron density map shows that the region of highest density is located approximately 75% of the chamber length downstream. The point cusp injection may "flatten out" the disk or toroidal distribution. There may be possibility for minor adjustment of the spatial distribution depending on the axial placement of the hollow cathode. If needed, it is possible to install a baffle downstream of the orifice to disperse the electrons to a finite radial location at the expense of additional electrical loss from an increased keeper current and cathode sheath drop.

6.3.3 Magnetic Field Optimization

The magnetic field topology shown in figure 6.1 was mainly designed as a preliminary test of the ARCH concept. The ARCH discharge prototype was designed to minimize complicated machining work, using in-house spare parts and readily available vendor stock. Therefore, the field topology was only configured enough to roughly obtain a few key design aspects: a center null region that is downstream of the extraction plane, the center field line of the outer-cusp is sufficiently spaced from the anode walls, and a relatively flat drop-off of the magnetic field strength in the axial direction. Through refinement of the field topology using custom ring magnets, it should be possible to achieve notably better beam flatness and discharge performance.

The field topology in figure 6.13 features a stronger upstream magnetic field, a less "toed-

in" inter-cusp field, and stronger axial fields adjacent to the anode walls. Currently, the rear plate has a thickness of 1 mm and the permanent magnets are spaced ∼1.5 mm away on the other side. It was designed conservatively to prevent demagnetization of the ring-cusp and to obtain the desire field structure with the available stock magnets. However, operation of the ARCH thruster revealed that heating of the region upstream of the discharge is no longer a design constraint (with a filament cathode). In conjunction with using better magnets, the magnetic field can be reconfigured to obtain higher inter-cusp field strength at the rear plate. The radial side pole piece modifies the topology for a stronger and more vertical near-wall magnetic field to account for the expected reduction of ion current to the rear plate. Furthermore, the design allows for better distribution of the plasma along the radial plane by toeing out the inter-cusp fields. Installed external to trim coil, the pole piece would also improve the efficiency and effectiveness of coils.

CHAPTER 7

Conclusions

In this thesis, experiments, computational models, and theory were used to investigate cusp confinement and the plasma behavior of miniature-scale DC discharges. The scientific findings and insights culminated in the development of the highly efficient ARCH discharge design, which is demonstrated to overcome the scaling limitations of conventional DC ion thruster designs. To describe the major findings that lead to the design of the Axial Ring-Cusp Hybrid (ARCH) discharge, the following sections successively describe major conclusions from chapters 3 to 6, and how these conclusions led to the design. This chapter highlights the main conclusion drawn from these chapters into four main sections. Recommendations for future work are provided within each section.

7.1 Cusp Interaction

Primary electrons are responsible for delivering the entire discharge power to the plasma and thus, their confinement is critical to the overall performance of any DC ion thruster. It was found in chapter 3 that the primary electron leakage to the cusp can be strongly influenced by the upstream magnetic field structure. This effect is of particularly importance for miniature scale discharges as most of the plasma volume is magnetized and each cusp element is in close proximity to another. The loss structure for the multi-ring cusp experiment exhibited an intricate collection pattern of peaks and ridges at the target point-cusp. These 1 to 2 mm features were a result of <0.2 mm perturbations of the particle's guiding center caused by small azimuthal fields very near the adjacent ring-cusp. The trajectory

perturbations of the primary electrons at one cusp was found to carry over to the following cusp instead of "resetting" at the nearby low-field region.

The geometry effect which led to a larger leak width at the point cusp in the electron gun experiments was also present in the spindle-cusp experiments (appendix A) and ARCH discharge (chapter 6). The hybrid leak width, derived based on the cross-field diffusion of plasma as it funnels into the cusp, is generally dependent only on the local magnetic field strength. However, the conservation of magnetic flux and the limited flux densities of permanent magnets lead to an expansion of the particle's guiding center as it approaches one cusp element from another that is at a greater radial location. Therefore, the leak width at the point-cusp for the spindle-cusp experiment and the inner ring-cusp in the ARCH discharge is larger than what is described by conventional theory.

7.2 Langmuir Probe Analysis for Cusp Discharges

The results from chapter 4 show that careful consideration must be taken when measuring a cusp-confined plasma with a Langmuir probe. The plasma density should be interpreted from the ion saturation region of the $I-V$ curve as the population is unaffected by magnetic fields typical of DC ion thruster discharges. The plasma electron temperature should be interpreted from the EEDF data when there is a strong presence of primary electrons. The 8 cm RCTD experiment was the first to obtain a primary electron density map. These results show good quantitative agreement with a MCC particle pusher simulation and provided strong evidence that the primary electron behavior can be treated independently in a DC ring-cusp discharge. It was also found that the magnetic fields do not directly inhibit the higher-energy primary electrons collection through confinement, but rather by altering their velocity distribution function (VDF) throughout the discharge.

In regard to future work, it may be of interest and short order to develop a probe analysis theory to extract the primary electron VDF from an orthogonal set of Langmuir

probes. A more advance Langmuir theory can also be implemented to analyze the low energy electron collection region of the EEDF. Several authors have formulated a kinetic theory which considers collisional sheaths and magnetized electrons [44]. It may be possible to obtain a more accurate plasma potential and possibly the plasma density and electron temperature very near the cusp. It would also be of interest to further investigate whether the measured EEDF and discharge condition would lead to the growth and saturation of the two-stream instability that may be responsible for the anomalous primary EDF observed in the probe data. This would allow computational models to more accurately simulate primary electrons and DC ion thruster discharges.

7.3 Miniature Ion Thruster Ring-Cusp Discharges

The discharge maps for all tested configurations show that the entire plasma structure is governed by the magnetic field topology, which is strongly dictated by the spatial distribution of the primary electron population. The performance data and discharge maps from chapter 5 provided crucial insight into discharge behavior of miniature DC ion thrusters. The overall results from the 3R discharge maps confirms previous findings from DC-ION that MiXI is a "primary ionizer." The high discharge loss is a result of the prodigious loss of primary electrons which limits the energy transferred to the plasma electrons; ions are almost exclusively generated from direct primary electron ionization. In addition, the discharge map was able to resolve details in the plasma structure and behavior that was previously unknown: (1) the flat beam profile is a result pushing the downstream cusp structure so that it lies along the extraction plane and (2) the virtual point-cusp between the two downstream ring-cusps inhibits the transport of the bulk plasma to the extraction plane.

It was found that conventional ring-cusp confinement methods are subject to inherent scaling limitations since the reduced primary electron confinement length caused by the volume reduction cannot be mitigated by reducing the overall cusp area. Almost any cusp

exposed directly to the bulk plasma will lead to high primary electron loss. Findings from the 5R configuration indicated that it is possible to confine primary electrons in a miniature discharge without encountering the discharge stability trade-off that has traditionally been considered a driving limitation of ring-cusp ion thruster design. The 4R configuration expanded on findings from the 5R configuration and demonstrated very promising improvements to the discharge performance. The use of an isolated ring electrode was found to be an effective approach at mitigating the primary electron lost at the cusp but also lead to an undesirable electric field within the internal plasma that must be considered in future design iterations.

7.4 ARCH Discharge

The ARCH discharge design decouples primary and plasma electron loss by shielding the anode with a moderate magnetic field which selectively only collects the diffusive plasma electrons. The primary electrons are trapped between the ARCH-shaped fields that span across the extraction plane to improve beam uniformity. The cusps are terminated at below cathode potential to electrostatically plug the leak area, which almost completely confines of the primary electrons from the chamber walls. The discharge mapping was crucial to the initial design and subsequent improvements to the ARCH discharge. The method revealed the existence of the Simon short circuiting of the inter-cusp region that was leading to high upstream ion loss, an uncommon phenomenon not usually seen in ion thruster discharges. From the results presented here, the most immediate improvements to the ARCH discharge would be to bias the inter-cusp ring to a potential near the anode voltage to reduce the upstream ion loss. The ARCH discharge design is expected to be highly-scalable due to the simple magnetic field geometry and the nature of the primary electron confinement. Further miniaturization is expected to be only limited by the physical size of the hollow cathode.

APPENDIX A

Spindle Cusp Experiment

Note: This appendix was originally a chapter in my prospectus and has remained unchanged.

Although measurements from the electron gun experiment have shown complex interactions between cusps, it remained unclear whether the same behavior would still manifest in a plasma discharge where there are interactions amongst other plasma species. This chapter is a work in progress to study cusp interaction and the effect of localized primary distribution in a weakly ionized plasma. In addition, measurements of the distribution of each plasma species will be taken for multiple ring cusp elements to investigate the inter-cusp diffusion for a variety of discharge conditions.

A.1 Approach

A.1.1 Experimental Setup

The design of the discharge experiment, shown in figure A.1 and diagrammed in figure A.2, is a progression of the electron gun experiment with the Helmholtz setup from section 3.3.1. It operates in the same facility with the same diagnostic and pumping capabilities. For the final configuration, an identical Helmholtz coil is installed and coil currents can be independently adjusted to generate either an extended Helmholtz field or a double spindle cusp. Anode rings are installed to collect plasma loss to the ring cusp and the cathode source is placed within the low-diverging field at the first spindle cusp. Neutral gas can be injected

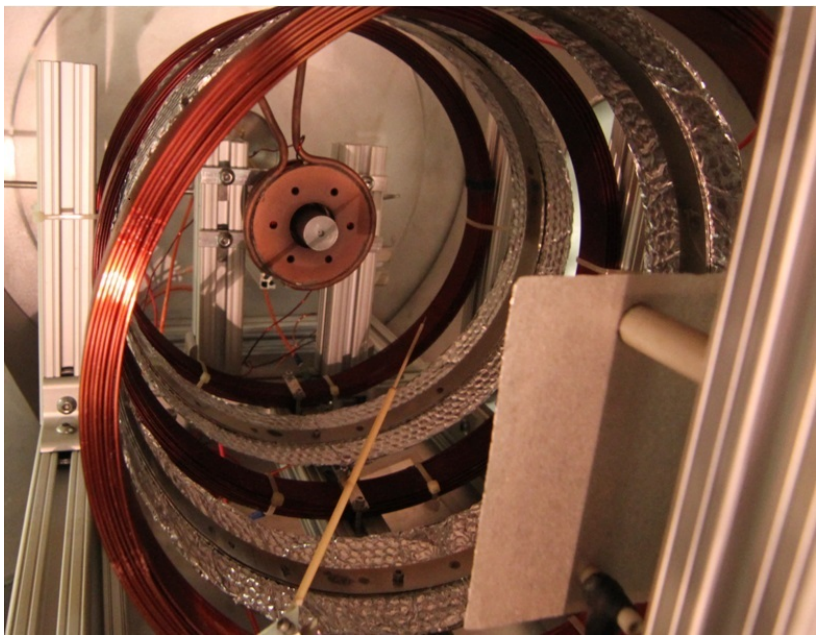

Figure A.1: Image of the multi-cusp discharge experiment with the hollow cathode in the back and the point cusp anode plate in the front. The point cusp magnet is not present in this picture.

into the chamber from both the hollow cathode and the back fill port to the desired neutral pressure via a flow controller and needle valve, respectively. A gate valve for one of the two cryogenic pumps is usually left closed during operation to reduce the total pumping speed and conserve the xenon gas supply. The back side of the point cusp anode plate is covered with a sheet of mica insulator to prevent the plasma from connecting to the backside of the anode.

The source is a barium oxide neutralizer hollow cathode for conventional sized EP thrusters on loan from the Jet Propulsion Laboratory. With a 1 mm orifice size, it is designed for relatively low-current steady operation of $1 - 8$ A. Operation of the cathode at discharge currents below 1.5 A requires additional current to the keeper to maintain adequate emission temperatures at the insert. The hollow cathode source is grounded to the vacuum chamber while all other surface besides the anode are electrically isolated. The cathode is operated by heating the barium oxide insert with a ceramic heater while either xenon or argon gas

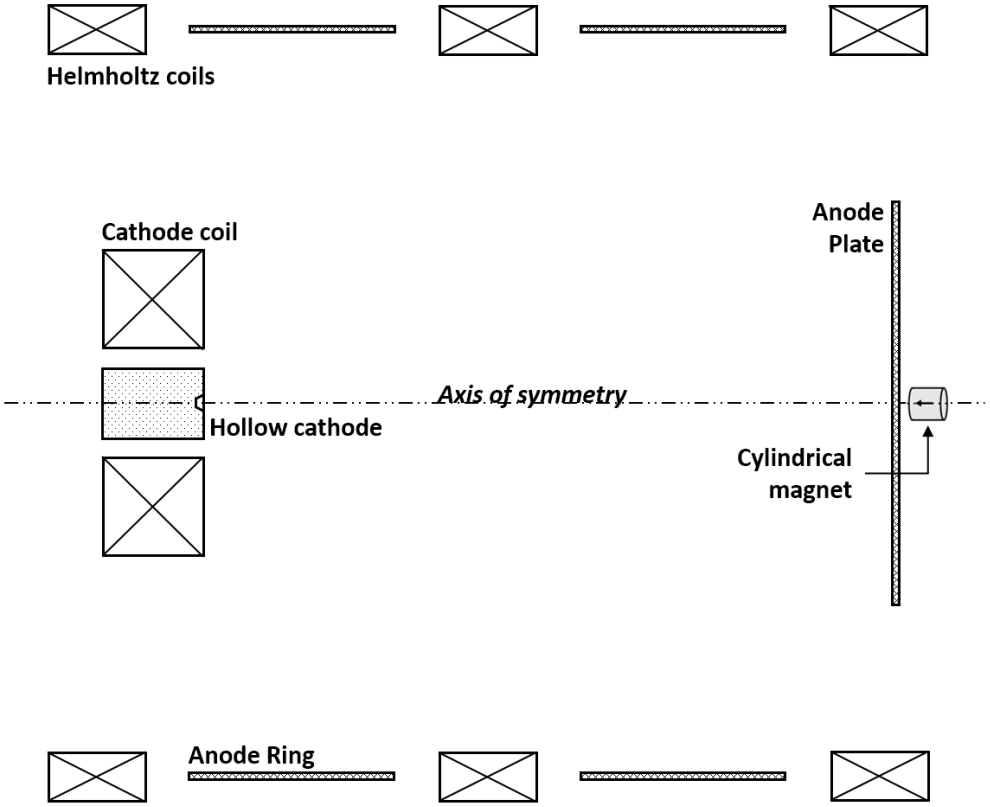

Figure A.2: Diagram of the multi-cusp discharge experiment shown in figure A.1. Each coil is powered independently to be able to generate various magnetic field configurations.

is injected down the tube. The keeper surface that is directly downstream of the orifice is then biased to a high positive potential to "strike" a sustained plasma current. The heater supply is then turned off to prevent overheating as the plasma bombardment and thermal insulation of the insert is enough to maintain emission temperatures.

A.1.2 Diagnostics

Langmuir and emissive probes are the most prominent method used to measure the properties of partially ionized plasma. At the most basic, they are both relatively simple to construct and operate. As shown in figure A.3b, the Langmuir probe consist of a supported electrode, most commonly cylindrical in shape, that is exposed to the plasma. Plasma conditions such as the density, electron temperature, and plasma potential can be interpreted using several theories based on how plasma is collected at a biased electrode. The circuit of the probe is diagrammed in figure A.4, particularly on the section right of the Kepco bipolar power supply. The function generator and Kepco is used to bias the probe with a repeating triangular voltage sweeps, the values of which are measured with a voltage divider and unity gain buffer. The probe current is measured using a shunt resistor on the high side of the circuit to avoid leakage current from the voltage divider and power supply. Hence, an optically isolated amplifier is required to differentially measure the shunt voltage using a standard National Instruments DAQ.

The Langmuir probe can also be operated at a fixed potential rather than a voltage sweep to collect only the saturation currents. This is generally used to collect only the ion saturation because the ion sheath is not as sensitive to changes in density or plasma potential. The fixed potential allows for significantly better time resolution to measure oscillations in the plasma. Although temporal measurements are also possible with Langmuir sweeps, it is extremely difficult to develop a system capable of generating the rapid voltage sweeps. There are innumerous amount of literature on the analysis of Langmuir probe traces [45, 67, 48]. The current collected on the probe can be significantly affected by the magnetic field, Debye

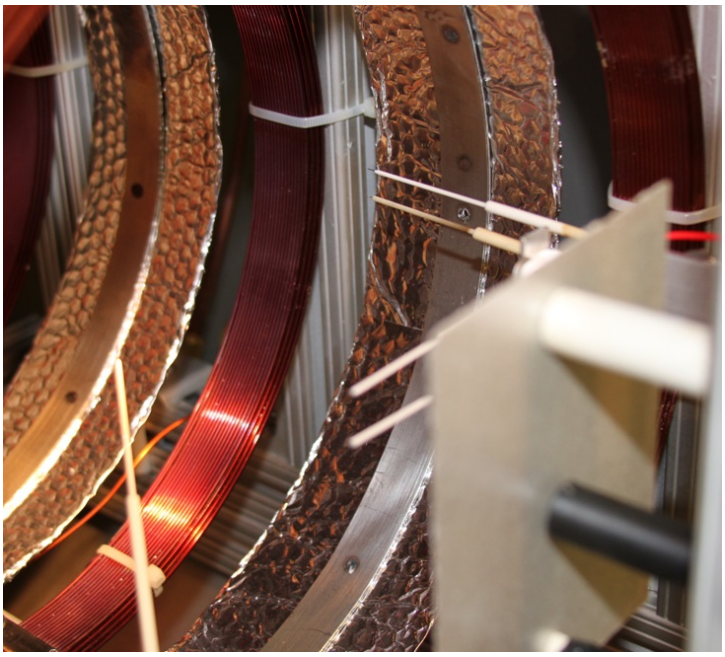

(a) Probe Setup

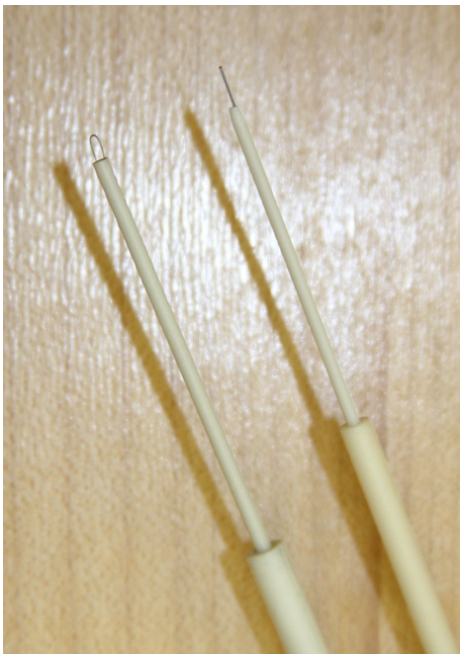

(b) Emissive & Langmuir Probe

Figure A.3: (a) Image showing the setup of the perpendicular set of probes mounted onto translational stages take measurements at both the point and ring cusp. (b) Closeup image showing the construction of the Langmuir and emissive probes.

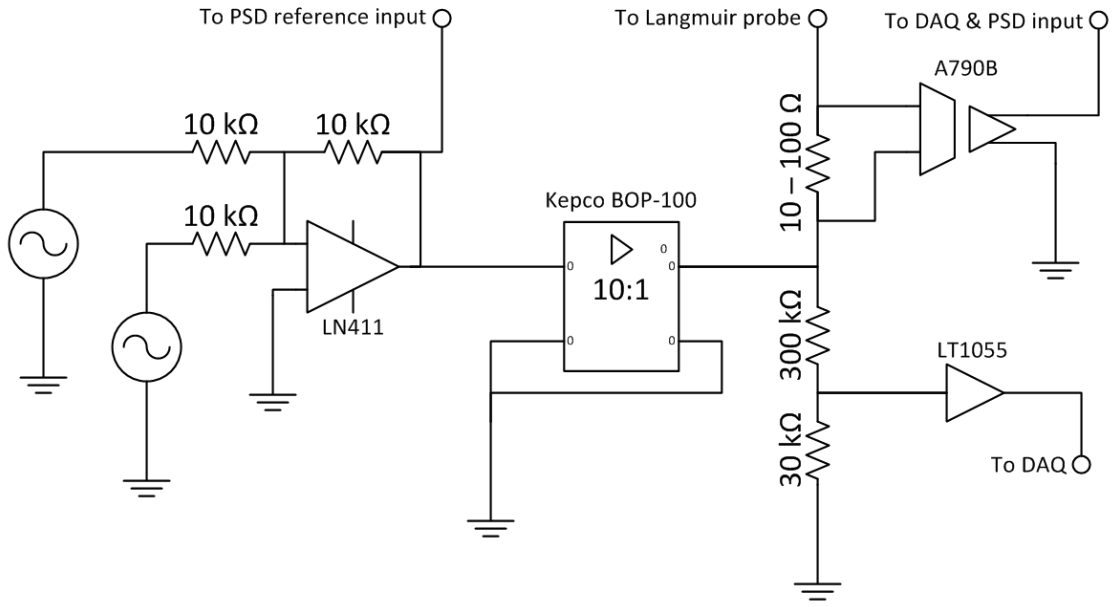

Figure A.4: Circuit diagram for operation and measurements of a Langmuir probe including a summing amplifier circuit for measuring the EEDF.

length, and the energy distribution of the electrons. These factors are particularly important for this work as measurements are taken across a magnetic cusp where there are large density gradients and the magnetic field orientation changes relative to the probe. A review of the various Langmuir probe theories will be included in the appendix for the finished dissertation.

The emissive probe is used to directly measure the plasma potential rather than from interpretation of theory with the Langmuir trace. As shown in figure A.3b, the probe consists of a long ceramic tube with an exposed filament at the end. As shown in figure A.5, a heater power supply is used to bring the temperature of the filament to a point where it can emit freely thermionic electrons. The filament and heating circuit is electrically isolated with a high impedance path to ground so that a floating probe potential can be measured with a voltage divide circuit. Therefore, the probe will generally sustain a potential one electron temperature below the plasma potential where there is no net current to the filament. The emissive probe also does not require a temporal voltage sweep and can be a good tool to

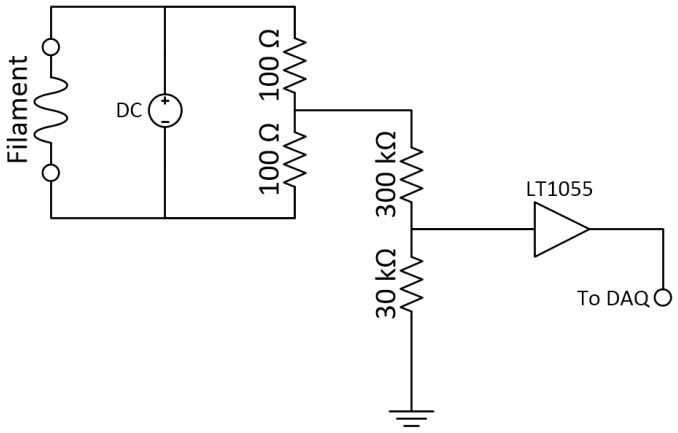

Figure A.5: Circuit diagram for operation and measurements of a emissive probe.

measure plasma potential oscillations in the discharge.

The geometry of the experiment does not allow for a Langmuir or emissive probe to spatial scan both the point and ring cusp with a single set of stages. As shown in figure A.3a, two sets of probes are perpendicularly mounted onto a holding device attached to the 3-axis set of stages. They are position in manner to prevent impingement from both probe sets into the plasma when one is being operated near its respective cusp.

The wall probe had to be redesigned to operate properly within the higher temperature of a plasma. The previous probe, shown in figure 3.3, was constructed using epoxy to adhere the collector to the aperture plate. The epoxy quickly overheated in preliminary testing and was substituted with ceramic cement. Figure A.6 shows an initial test design of the plasma wall probe with a larger aperture. However, the aspect ratio and aperture width was heavily affected by a changing sheath size so that an effective probe area cannot could not be determined. Near the edge of the cusp, the sheath may expand to nearly block all current to the collector. The wall probe will have to be redesigned so that the collector electrode is flushed with the plate and sufficiently small to obtain reasonable spatial resolution. Although the sheath structure may not be conventional, the simple geometry may allow for analytical formulation to resolve an accurate plasma measurements.

In order to determine the primary electron population in the plasma, their collected

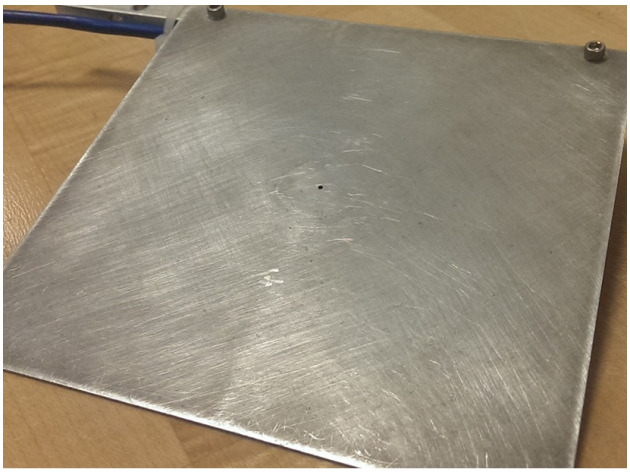

Figure A.6: Image of the plasma wall probe. The design in similar that for the electron gun experiment but constructed to handle high temperatures.

current must be differentiated from those of the plasma electron. The electron energy distribution function (EEDF) can be extracted from the second derivative of a standard Langmuir probe trace [43, 68, 44]. However, these measurements often have considerable plasma and electronic noise that which makes it difficult to obtain a smooth derivative. Even after averaging the Langmuir traces over numerous sweeps, complex smoothing and regularization techniques have to be implements to obtain usable data [69, 70]. In addition, many standard smoothing algorithms have a tendency to distort the second derivative and artificially change the shape of the EEDF. A lock-in amplifier, shown in figure A.7, is essentially a phase shift detector (PSD) that can instead be used to directly measure the first and second derivative of the Langmuir probe response. The process involves superimposing a harmonic signal onto the voltage sweep using a summing amplifier circuit shown in figure A.4. The voltage response from the shunt resistor is then multiplied with the reference signal and the derivatives can be extracted from the harmonics. Further detail of the lock-in amplifier operation and mathematical derivations will be covered in the appendix for the finished dissertation.

Figure A.7: Image of the Signal Recovery Model 7270 lock-in amplifier.

A.1.3 Test Plan

To characterize the cusp interaction, EEDF and emissive probe measurements will be taken across the both the point and ring cusps for a range of magnetic field strength and discharge conditions. A permanent magnet will be place at the point cusp as a reference field strength. Due to the strong but short range of permanent magnets, the field strength at the ring cusp can be adjusted without significant affecting the field at the point cusp. Data gathered from this simple geometry experiment may possibly assist in the modeling of the inter-cusp interactions based on parameters such as the Larmor radius and width of magnetic field flux tubes. The analysis may also aid in analytical performance calculations of discharge chambers with reducing radii or conical in shape, such as divergent cusp-field thrusters and some ion thrusters.

The plasma loss between ring cusps will be measured using a double spindle cusp magnetic field configuration with the same EEDF and emissive probe diagnostic. An additional ring electrode will be inserted in between ring cusps in order to investigate possible changes in cross-field diffusivity between an insulating and continuous conducting cylindrical wall.

A.2 Preliminary Results and Discussion

The experimental results shown in the section was taken to characterize the various probes, plasma discharge, and theories for probe analysis. Therefore, they have not been well analyzed and meticulously details of the operating conditions are not given. Figure A.8 shows a typical Langmuir probe trace measured at an intermediate density region of the plasma which has been average over numerous sweeps. This particular probe dimension is 0.010" diameter by 0.140" in length. The plot on the left side is cropped to show the ion saturation, electron retardation, and electron saturation region. The right side plot shows just the ion saturation portion of the trace along with a theoretical curve fit. Ion saturation is preferable for interpreting the plasma density as the motion of the heavier ions are not directly affected by the magnetic field. The shape of the curve indicates that the probe is operating in a regime in between thin and thick sheath theory. Therefore, the curve fit uses an intermediate theory, developed by Laframboise [45], that accounts for orbital motion of ions and an expanding sheath about the cylindrical collector.

A.2.1 Helmholtz-Cusp

The magnetic field for the Helmholtz-cusp configuration mimics that from the electron gun experiments in section 3.3.1. Figure A.9 shows an image of the discharge in operation with the expected plasma column created by the axial magnetic field. An anode grid is installed a short distance downstream of the cathode in addition to the axial anode plate. Without the grids, the plasma conditions would dramatically change when the wall probe is operated directly at the point cusp by changing the total effective anode area of the discharge. Compared to the electron gun experiment, the spatial location of the charged species can be seen visually. As was expected from the results in section 3.3.2, there is a misalignment of the components which causes the plasma to flow into the point cusp off axis. Although each component was aligned with a laser level, small tilts in any of the coils would cause large

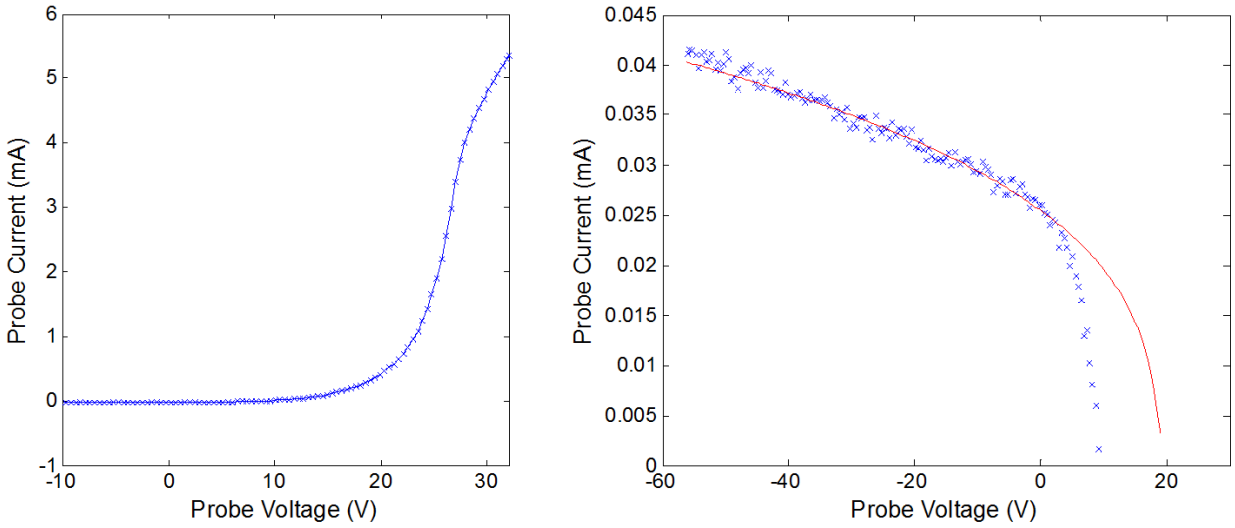

(a) Full Langmuir probe trave

(b) Ion saturation curve

Figure A.8: (a) Sample Langmuir probe trace showing the ion saturation, electron retardation, and electron saturation region of the sweep. (b) Close up view of the ion saturation region with a curve fit used to determine plasma density.

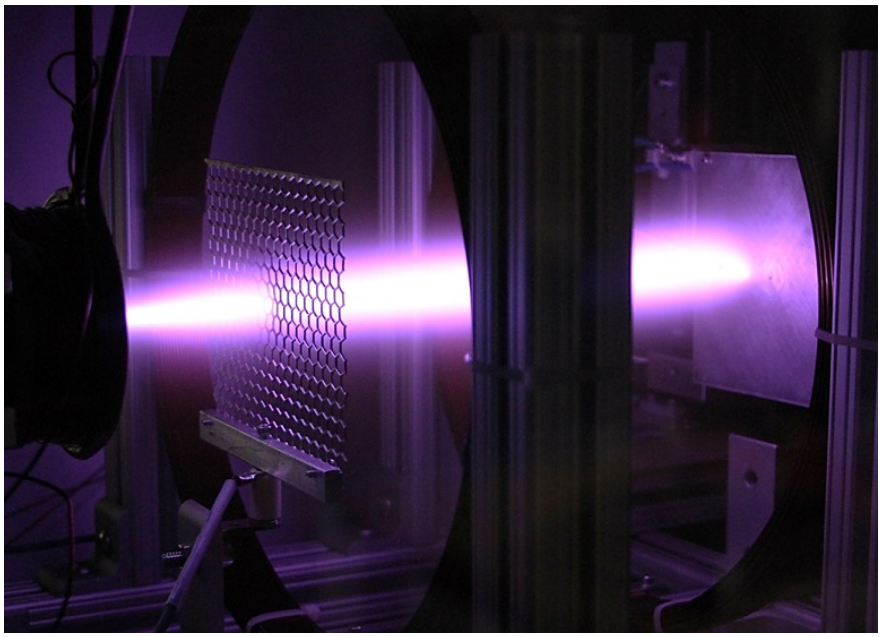

Figure A.9: Image of the plasma discharge in the Helmholtz-cusp configuration. High energy electrons generated at the cathode are confined to an axial magnetic field that terminates at the point cusp.

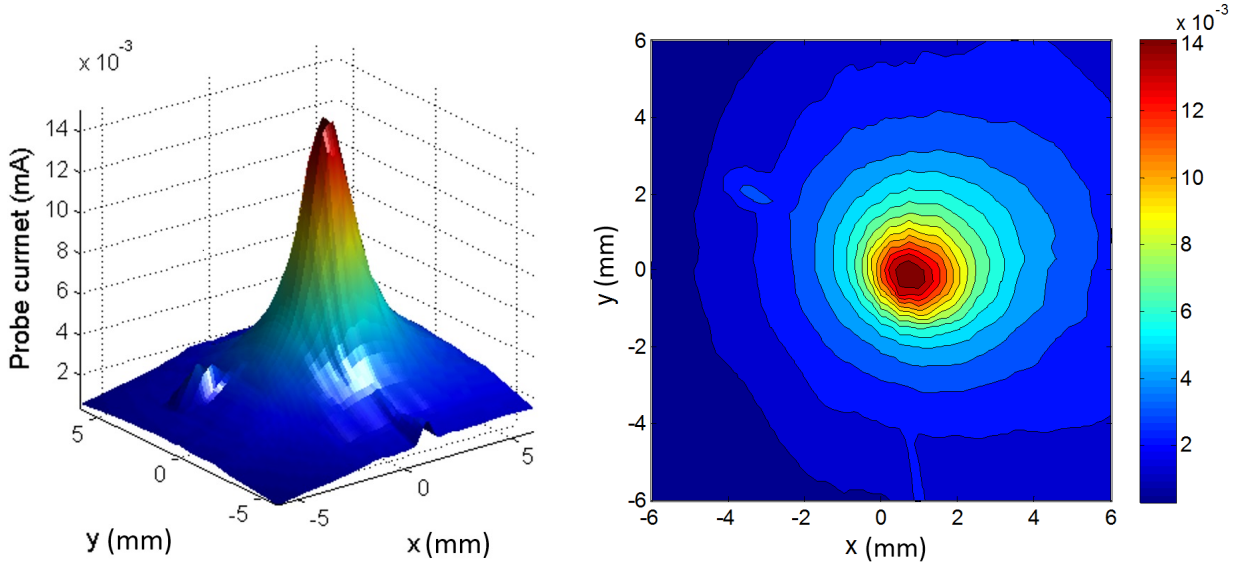

(a) Surface plot **(b)** Contour plot

Figure A.10: Ion saturation measurements using the plasma wall probe for the discharge in a Helmholtz-cusp configuration.

displacement of the field lines at the point cusp. The large turn-in of the plasma would be adequate to account for the expected curvature drift in the electron gun results. However, there is no annular collection in the plasma results. This could be attributed to the addition of ionization collision as well as changes in electrostatic confinement conditions at either ends of the plasma column.

The results shown in figure A.10 was for a 19.1 V and 5.0 A discharge operating in 5.0×10^{-4} Torr of xenon gas with an average axial field of about 60 Gauss. The wall probe was rastered across the cylindrical point-cusp magnet at an ion saturation voltage of -90 V. Although electron saturation was also measured, the results are not shown because the changing plasma potential across the cusp have considerable affect to the sheath expansion. The cusp magnetic field strength measured at the location of the probe is about $1.4-1.5$ kG. The estimated leak FWHM diameter measured from figure A.10 is approximately 2.1 mm which coincides almost directly to the geometric mean expression of four times the hybrid gyro-radius.

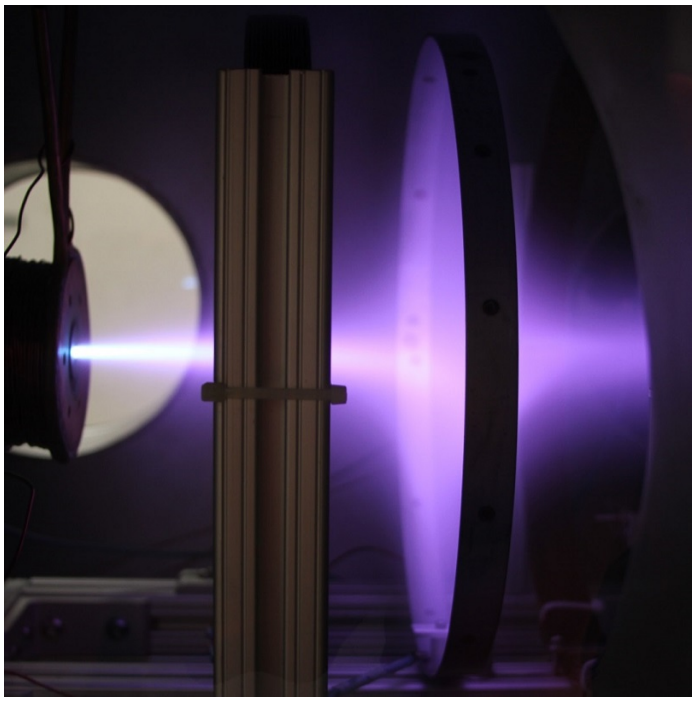

Figure A.11: Image of the plasma discharge in the single spindle-cusp configuration. High energy electrons are injected at the upstream point cusp and loss to the anode ring and plate at the ring and point cusp, respectively.

A.2.2 Spindle-Cusp

The plasma discharge shown in figure A.11 was operated in the single spindle cusp configuration where one of the coils is generating an axially opposing magnetic field to the other. The first coil shown in figure A.2 was not yet installed and the hollow cathode injected plasma at the upstream point cusp. Both anode surfaces at the ring and point cusp were kept at the same potential even though the majority of the discharge current is collected by the ring electrode. The discharge was operated at 22.2 V and 4.0 A with xenon gas at 2.0×10^{-4} Torr. A Langmuir and emissive probe was rastered across the maximum allowable range which was limited to obstruction from the coils and anode surfaces.

The plasma density is interpreted from the ion saturation curve and the electron temperature from the electron retardation region. The orientation of the results shown in figure A.12 is such that the left and bottom side of the plot corresponds to the point and ring cusp, re-

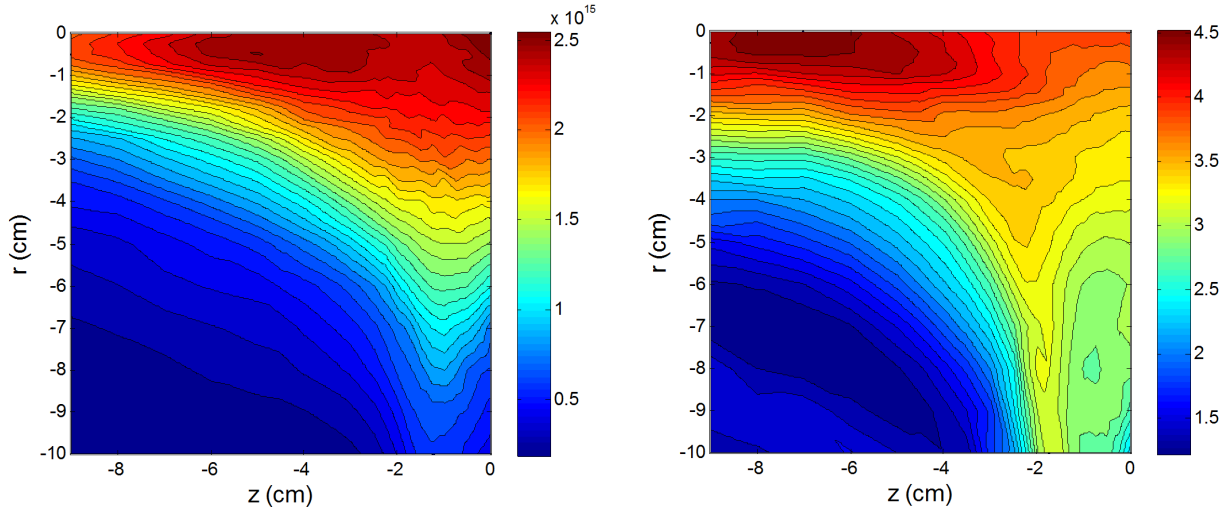

(a) Plasma density (m^2) **(b)** Electron temperature (eV)

Figure A.12: Analysis from Langmuir probe measurements of a spindle cusp plasma. The left and bottom sides are facing in the direction of the point and ring cusp, respectively.

spectively. The electron temperature contour shows the expected behavior of shaping to the magnetic field lines. These flux lines represent isothermal lines due to the highly anisotropic transport coefficients. However, the electron temperature is also shown to be decreasing towards the ring cusp and increasing towards to point cusp, away from the cathode source. This is likely attributed to the magnetic nozzle effect in which the plasma is expanding towards the ring cusp while converging at the point cusp. The same temperature trends have previously been measured in experiments [71, 72] as well as modeled computationally [73]. The plasma density contour follows a similar trend as the electron temperature but decreases more rapidly towards the ring cusp. Although the measurement region does not reach the cusp location, the estimated FWHM girth of the plasma at each respective side is much less than the geometric hybrid gyro-radius. The highest magnetic field from just the spindle cusp is approximately 20 Gauss which corresponds to a 12 cm hybrid gyro-radius.

A.2.3 Asymmetric Injection

The original experimental configuration had a single spindle cusp and the cathode source station before the first Helmholtz coil. The intention was to inject plasma and high energy electrons from the upstream point cusp and investigate the transport across the null region to the opposite point cusp. However, injection at the diverging high field location led to prodigious loss of primary electrons directly to the ring cusp. This manifested in an overall low plasma density and discharge voltage for the relatively high discharge currents. The effect can be seen in figure A.11 where the plasma density appears to be greater in lower azimuthal direction, indicating that the primary electrons are not streaming down the center of to the null region of the spindle cusp. There is an overall azimuthal preference because the magnetic resistance is lower for the primary electrons to take the off-axis path rather than to lose its magnetic moment in the null region. The dense and collisional plasma directly in front of the hollow cathode facilitates a region of high cross-field diffusion across the point cusp field. In addition, the high field strength injection site ensured unfavorable initial magnetic moments for reflection at the ring cusp. Once a "path of least resistance" is established, the azimuthal preference is further solidified by lower resistivity from the resulting higher plasma density. The asymmetry is more pronounce with higher cathode coil field strength and higher cathode gas flow. The suspected highly asymmetric primary electron stream was also measured in the electron gun experiment. Proper care has since been taken to ensure the hollow cathode is place in a region of adequately low field strength.

A.2.4 Concluding Remarks

A versatile discharge experiment was developed to study cusp interactions and plasma diffusion in various multi-cusp configurations. Early preliminary results for the spindle cusp discharge show a surprisingly well confined low-β xenon plasma for very low magnetic fields. The width of the plasma near and approaching the cusps are several times smaller than the geometric hybrid radius and instead, are much closer to the primary electron gyro-radius.

However, more detailed measurements and analysis are required before any conclusions can be made.

APPENDIX B

Discharge Modeling

Note: This appendix was originally a chapter in my prospectus and has remained unchanged.

The results and analysis from the primary electron multi-cusp experiment in section 3.4 indicated that the loss structure at a particular cusp element can be significantly influenced by the upstream magnetic field and can lead to an increase loss area. This is particularly prominent in 3-D cylindrical domain where the magnetic flux is increasingly compressed closer the center-line of the domain. However, this effect has only been measured and simulated first hand for primary electrons whose dynamics differ considerably to the other plasma species. It is not clear whether this phenomenon carries over to the ions or plasma electrons as their motions are generally driven through collisions and electromagnetic interaction amongst the two species. The spindle cusp domain is similar to the multi-cusp experiment in that they both provide a significantly converging field structure at the point cusp that would enhanced geometric effect seen in the primary electron data. In addition, the spindle cusp has been prominently used in past studies of leak widths in low-β plasmas and experimental data are readily available for comparison with computational results.

Although preliminary results from appendix A.2.2 may suggest cusp interaction, the measured properties are currently not reliable or comprehensive enough to convincingly certain. Previously, Bosch and Merlino [21] measured the plasma density and potential for the entire spindle cusp domain as well as the plasma leak width at both cusp elements as shown in figure B.1. The ring cusp results show an expected Gaussian-like loss profile

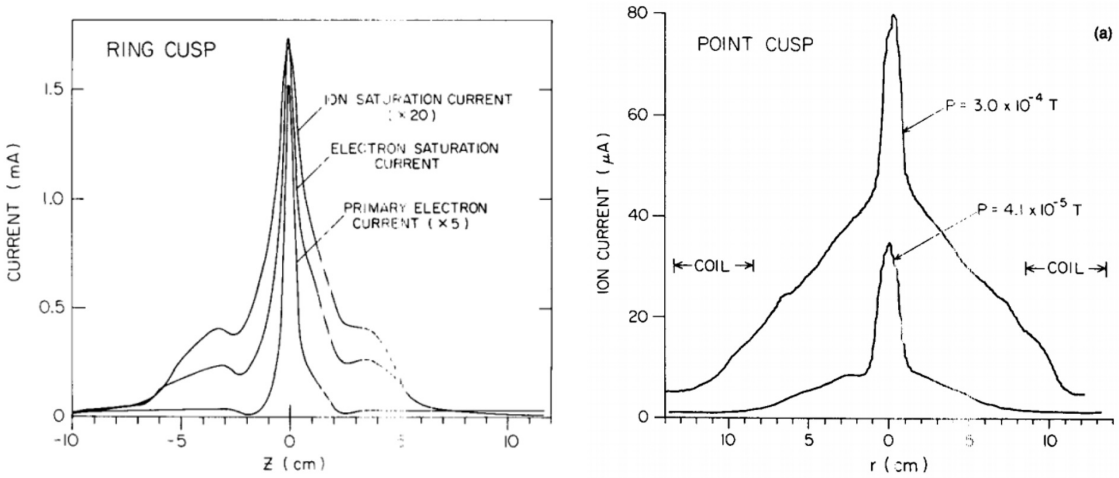

(a) Ring cusp **(b)** Point cusp

Figure B.1: Ring and point cusp leak width profiles of a spindle cusp discharge measured by Bosch and Merlino.

that was found to follow the hybrid loss radius scaling. While the point cusp loss profile also exhibits a similar profile in the center, the results also show a large accompanying shoulder region that becomes more pronounced at higher pressures. Integrated over the axis-symmetric domain, the shoulder region encompasses the bulk of the plasma leakage at the point cusp. Conventional theory for the loss width at the cusp would suggest that the plasma should be more confined at the point cusp due to the much greater magnetic field strength. The data shown here suggests a similar behavior as seen from the primary electron results from section 3.4.2. A simple model of a spindle cusp plasma is developed to analyze the interaction between the point cusp and ring cusp in a diffusive plasma.

B.1 Approach

B.1.1 Model Overview

This model solves a heavily simplified fluid equation, known as the diffusion equation, in which plasma transport is assumed to be dominated by collision with the neutral gas. The

equation is solved on a magnetic field aligned (MFA) mesh to reduce the effect of numerical diffusion in a highly anisotropic plasma spindle cusp geometry. The plasma generation is assumed to be directly proportional to the primary electron density. The distribution of which is determined independently using a particle pushing technique with the equation for single particle motion in an electromagnetic field. The model will simulate the plasma conditions similar the the spindle cusp discharge experiment in appendix A.2.2. However, the model is currently not self-consistent as it requires multiple inputs based on typical laboratory plasma operating conditions and ignores many second order effects. The purpose of the model is not to accurately simulate a discharge from experimental input conditions, but rather, to investigate physical behaviors at key regions in the discharge to explain trends in the experimental data.

B.1.2 Governing Equations

The plasma in ion thrusters and many laboratory devices are weakly ionized and transport is primarily dominated by neutral atom collision rather than amongst other charged particles. The fluid model treats the plasma as fluid elements containing electrical charges and is obtain through velocity-space integration of the Vlasov-Maxwell equations. The equation for continuity and motion for each plasma species are derived from the zeroth and first moment and the assumption of an ideal fluid:

$$\frac{\partial n}{\partial t} + \nabla \cdot (n\mathbf{v}) = \dot{n} \tag{B.1}$$

$$mn\frac{d\mathbf{v}}{dt} = mn\left[\frac{\partial \mathbf{v}}{\partial t} + (\mathbf{v}\cdot\nabla)\mathbf{v}\right] = \pm en(\mathbf{E} + \mathbf{v}\times\mathbf{B}) - \nabla p - mn\nu\mathbf{v} \tag{B.2}$$

where ν is the kinematic viscosity, $\dot{n}$ is the generation rate, and the pressure, $\nabla p = kT\nabla n$, for isothermal compression. In addition, the plasma is assumed to be in steady state and

the transport is driven only by collisions. The above equations can then be rewritten as:

$$\nabla \cdot (n\mathbf{v}) = \nabla \cdot \Gamma = \dot{n} \tag{B.3}$$

$$\pm en(\mathbf{E} + \mathbf{v} \times \mathbf{B}) = kT\nabla n + mn\nu v \tag{B.4}$$

The ambipolar diffusion equation is obtain by combining the ion and electron momentum equations. The theory approximates quasineutrality in that the local ion and electron charge densities are equal ($\rho_{qi} = \rho_{qe}$) so that the total charge density is zero ($\rho_q = 0$). This assumption is generally valid when the length scale of interest is much greater than the Debye length for the given plasma condition. The remaining portion of the derivation is long and complicated with many new parameters introduced. It will be included in the appendix for the finished dissertation. The details of the derivation and parameters can be found in Koch and Matthieussent [25] and the ambipolar ion fluxes can be simplified to:

$$nv_i^{\parallel} = -D^{\parallel}\nabla^{\parallel} n \ , \ D^{\parallel} = \frac{\mu_e^{\parallel} D_i^{\parallel} + \mu_i^{\parallel} D_e^{\parallel}}{\mu_i^{\parallel} + \mu_e^{\parallel}} \tag{B.5}$$

$$nv_i^{\perp} = -D^{\perp}\nabla^{\perp} n \ , \ D^{\perp} = \frac{\mu_e^{\perp} D_i^{\perp} + \mu_i^{\perp} D_e^{\perp}}{\mu_i^{\perp} + \mu_e^{\perp}} \tag{B.6}$$

where μ is the mobility, D is the diffusion coefficient, and the $\parallel$ and $\perp$ subcripts denote the direction parallel and perpendicular to the magnetic field, respectively. The final expression above assumes that the local ion and electron generation rates are equal and that the perpendicular electric field is negligible due to a "short-circuit" effect [66]. Lastly, the momentum equations are combined with continuity, Eq. (B.1), resulting in the final expression:

$$\nabla \cdot (D^{\parallel}\nabla^{\parallel} n + D^{\perp}\nabla^{\perp} n) + \dot{n} = 0 \tag{B.7}$$

The diffusion coefficient is function of the electron temperature which normally has be calculated using an energy balance equation. This has yet to be implemented in any form and

a constant electron temperature was initially assumed. However, as the electron temperature generally decreases across the magnetic field away from the bulk plasma, the diffusion rates were artificially high in at the plasma edge. To better match the experimental data, a temperature profile was added to the model based on the spindle cusp measurements from figure A.12b.

B.1.3 Magnetic Field Align Mesh

A computational mesh that is aligned with the magnetic field is used in order to resolve the plasma interaction between point and ring cusp. The MFA mesh is commonly used approach to model highly anisotropic plasmas, particularly in both the electric propulsion [74, 75] and fusion energy community. The disparity between the transport coefficients parallel and perpendicular to the local magnetic field direction would cause significant numerical diffusion in key regions of the domain. Particularly, in the region between the point and spindle cusp where the magnetic field would predominately be at a 45° angle to standard Cartesian mesh boundaries. The model employs automatic generation of a structured MFA mesh for a simple spindle cusp geometry but will later be expanded for other configurations. The magnetic field of the domain is first calculated for a high-resolution Cartesian mesh by superimposing analytical expressions for the field created by an ideal current loop and/or permanent magnets [76]. Figure B.2 shows the resulting magnetic field direction and contour for a spindle cusp geometry.

The axis-symmetric geometry of the domain allows the magnetic field stream lines and equipotential lines to be described by the stream function (Ψ) and scalar potential (Φ), respectively. These functions offer a natural grid system for the field structure because their contour lines are inherently always perpendicular to each other. A method outlined by Mao [32] and Araki [75], uses magnetic field grid data calculated shown in figure B.2 to solve the

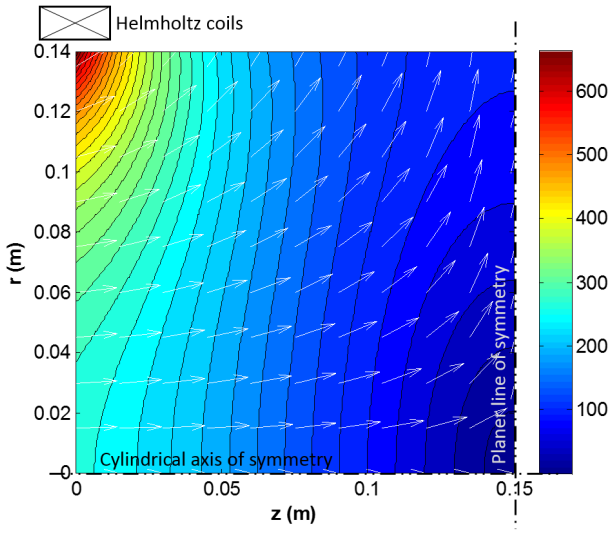

Figure B.2: Magnetic field contour (Gauss) for a spindle cusp geometry generated using the analytical expression for an ideal current loop.

following differential equation:

$$\frac{\partial^2 \Psi}{\partial z^2} + \frac{\partial^2 \Psi}{\partial r^2} = \frac{\partial}{\partial z}(rB_r) + \frac{\partial}{\partial r}(rB_z) \tag{B.8}$$

$$\frac{\partial^2 \Phi}{\partial z^2} + \frac{\partial^2 \Phi}{\partial r^2} = -\frac{B_r}{r} \tag{B.9}$$

Although simple analytical expressions for the stream function and scalar potential exists for a current loop, this method is more robust as it is able to resolve complicated fields with permanent magnets. The differential equations are easily solved using the standard 2nd order finite difference method on a uniform Cartesian mesh. The results for the magnetic field in figure B.2 are shown in figure B.3.

The streamlines and equipotential lines are readily extracted from the contour plot function in MATLAB. The set of contour levels are chosen based on the desired domain size and resolution of the mesh. In addition, a single equipotential line is always chosen to intersect with the bottom right corner of the domain to ensure all cells are four side. All chosen streamlines must also intersect with all equipotential lines and vise versa because the solver

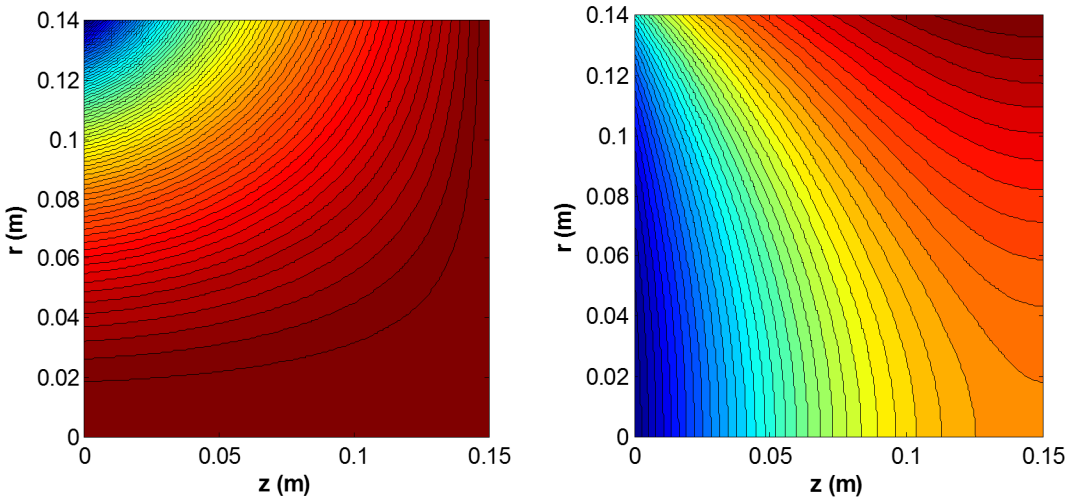

(a) Stream function **(b)** Scalar potential

Figure B.3: Contour plots for the stream function and scalar potential for the spindle cusp domain obtained by solving Eq. (B.8) and Eq. (B.9), respectively.

is currently limited to structured mesh. The location of the node points is then calculated from the intersections and properly indexed. The cell center location and cell volume are calculated by splitting the quadrilateral cells into two triangular elements. The centroid is the area weighted average of the split elements and the cylindrical volume can be found using:

$$V = 2\pi \left(A_a \bar{r}_a + A_b \bar{r}_b \right) \tag{B.10}$$

where A is the area and $\bar{r}$ is the radius of its centroid for each of the subscript triangle. Lastly, the cylindrical surface area for each cell face is calculated from:

$$S_v = 2\pi \bar{r}_v l_v \tag{B.11}$$

where l_v is the length and $\bar{r}_v$ average radius of each side of the cell. A low resolution sample mesh is shown in figure B.4 with all the cell center and node points marked. Magnetic field calculations are made for each cell center location that will be used to determine the diffusion coefficients. The relatively low grid resolution at the bottom right corner is an inherent

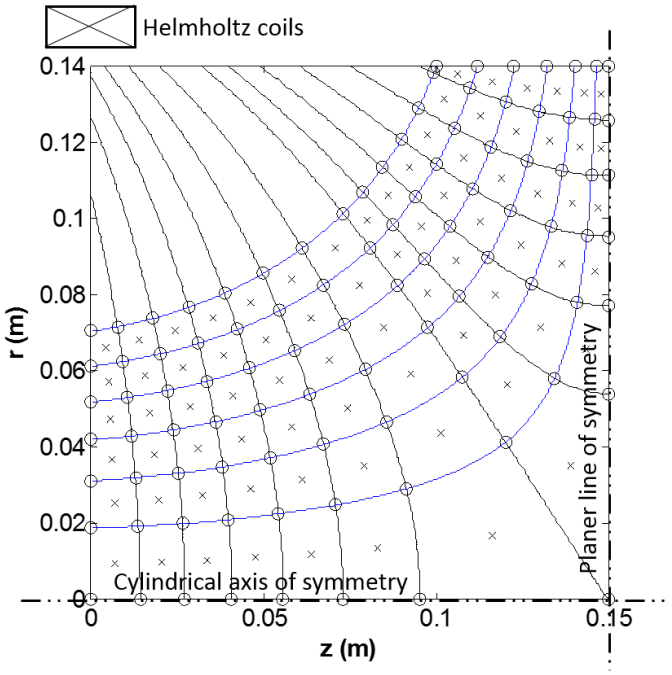

Figure B.4: Low resolution sample MFA grid for the spindle cusp geometry with the node points ("×") and centroids ("○") marked.

consequence of the structured MFA mesh. The region corresponds to a null point where the magnetic field strength is low and the streamline spacing has to increase to conserve the flux in between each flux tube. Although this region represents the bulk region of the plasma where the density is the highest, the loss of detail is mitigated by the increase uniformity within the low-field region.

B.1.4 Primary Electron Tracking

As previously described in chapter 3, primary electrons are relatively energetic electrons that accounts for essentially all the energy input into the plasma. Their population is normally less than 10% of the thermalized plasma electrons. In addition, Wirz has also suggested primary electrons to be directly responsible for the majority of ionization in miniature discharge devices [12]. For discharge conditions common to ion thrusters and weakly ionized laboratory plasmas, the mean free path for the primary electrons is much larger that the size

of the discharge chamber. Therefore, their non-collisional trajectories can be represented by the Lorentz equation which describes charge particle motion in an electromagnetic field:

$$\mathbf{F} = m\frac{\mathrm{d}\mathbf{v}}{\mathrm{d}t} = q(\mathbf{E} + \mathbf{v} \times \mathbf{B}) \tag{B.12}$$

where $\mathbf{E}$ and $\mathbf{B}$ are the local electric and magnetic field, respectively, and $\mathbf{v}$ is the average velocity of the primary electron population. All collisions are modeled as impulsive events that are statistically determined based on the mean free path calculations for a given discharge condition.

The "Boris Method" for particle pushing is a explicit second-order accurate scheme and is the most common method used for particle tracking in plasma simulations due to its accuracy and speed [39]. Standard explicit methods such as forward difference scheme causes the particle to rapidly accrue numerical energy, while implicit methods such as Runge-Kutta are computationally expensive to track multiple particles. The Boris Method uses a leapfrog scheme that also decouples the electric field push from that of the magnetic field to properly conserve the particle's energy. The method starts by solving a leapfrog Lorentz integrator which uses the average velocity at time "n" to propagate the particle:

$$\frac{\mathbf{v}_{n+1/2} - \mathbf{v}_{n-1/2}}{\Delta t} = \frac{q}{m}\left(\mathbf{E} + \frac{\mathbf{v}_{n+1/2} - \mathbf{v}_{n-1/2}}{2} \times \mathbf{B}\right) \tag{B.13}$$

where $\mathbf{v}_{n+1/2}$ and $\mathbf{v}_{n-1/2}$ represents the velocity at each forward and backward half step, respectively. This is accomplished by splitting the electric push as defined by the following equations:

$$\mathbf{v}_{n-1/2} = \mathbf{v}_{-} - \left(\frac{q\Delta t}{2m}\right)\mathbf{E} \tag{B.14a}$$

$$\mathbf{v}_{n+1/2} = \mathbf{v}_{+} + \left(\frac{q\Delta t}{2m}\right)\mathbf{E} \tag{B.14b}$$

The new quantities, $\mathbf{v}_{+}$ and $\mathbf{v}_{-}$, can then be substituted into Eq. (B.13) to obtain the

magnetic push equation for pure rotation:

$$\frac{\mathbf{v}_+ - \mathbf{v}_-}{\Delta t} = \frac{q}{2m}\left(\mathbf{v}_+ + \mathbf{v}_-\right) \times \mathbf{B} \tag{B.15}$$

This is resolved geometrically for circular rotation with a method that ensures the particle's momentum remains unchanged after the rotation:

$$\mathbf{t} = \left(\frac{q\Delta t}{2m}\mathbf{B}\right) \tag{B.16a}$$

$$\mathbf{v}' = \mathbf{v}_- + (\mathbf{v}_- \times \mathbf{t}) \tag{B.16b}$$

$$\mathbf{s} = \frac{2\mathbf{t}}{1+t^2} \tag{B.17a}$$

$$\mathbf{v}_+ = \mathbf{v}_- + (\mathbf{v}' \times \mathbf{s}) \tag{B.17b}$$

Therefore, to determine the updated half-step velocity, Eq. (B.14a) is used to calculate $\mathbf{v}_-$ and a full rotation is then applied using Eq. (B.16) and Eq. (B.17) to obtain $\mathbf{v}_+$. The other half acceleration is then applied to find $\mathbf{v}_{n+1/2}$ using Eq. (B.14b). Finally, the full step position can be obtain using:

$$\frac{\mathbf{x}_{n+1} - \mathbf{x}_n}{\Delta t} = \mathbf{v}_{n+1/2} \tag{B.18}$$

The model currently ignores the electric field and track particles only based on the applied magnetic fields from the spindle cusp coils. This assumption is usually reasonable in a uniform plasma as the plasma potential is constant and the presheath potential drop is insignificant to the primary electron's energy. However, this assumption becomes more inaccurate in magnetic fields where large and moderate potential structures may exist across and along the magnetic field, respectively.

As primary electrons traverse in the discharge, they encounter a range of elastic and inelastic collisions with other plasma species. These collisions are treated as probabilistic impulsive events based on macroscopic parameters and conditions of the discharge. Cur-

rently, only elastic scattering and inelastic ionization with the neutral gas is considered in the model. Excitation collisions and thermalization with the plasma electron population will be included in later future work. The equation for the change in electron flux (Γ) incident on a slab of particles for probabilistic hard sphere collisions is:

$$\Gamma(x) = \Gamma_0 e^{-n\sigma x} \tag{B.19}$$

where σ is the effective cross-sectional area , n is the density, and x is the slab length of the particles. The equation is normalized and rewritten as a collision probability based on the time step passage:

$$\text{Rand} \sim U([0,1]) > 1 - \exp(-n_0 \langle \sigma v \rangle_{pe} \Delta t) \tag{B.20}$$

where Δt is the particle pusher time step interval and $\langle \sigma v \rangle_{pe}$ is the electron velocity and the corresponding collision cross-section. A random number is generated at each time step and compared to the value of Eq. (B.20) for both the total elastic scattering and ionization cross-sections to determine collision events. The cross-sections for a particular electron energy are found from experimental data from past researchers [77, 78, 79]. For elastic collisons, an isotropic scattering angle with no energy loss is assumed. Therefore, the velocity direction is randomized which contributes to the diffusion of the particles. Each particle in the tracker is terminated when it encounters an ionization collision or is able to reach the cusp boundaries. Sample primary electron trajectories using the described method are shown in figure B.5 for illustrative purpose as upwards of a thousand particles are tracked to obtain a smooth density profile.

The primary electron density is estimated by measuring the tracked particle's time of flight within each of the grid cells. This process involves determining the grid index corresponding to the instantaneous spatial location of the particle at each time step. The method for rectilinear grid is trivial and quick to calculate. The MFA mesh presents a more complicated situation where each grid cell boundary location is practically arbitrary, and therefore,

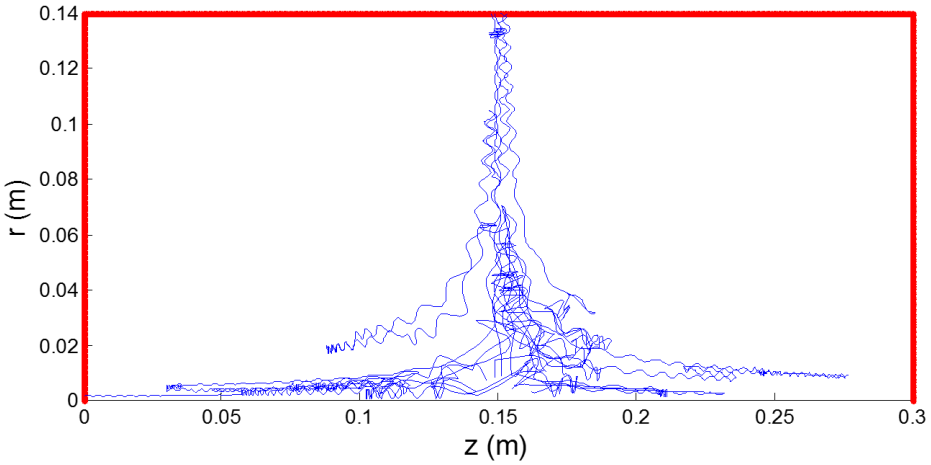

Figure B.5: Example trajectories of primary electrons in a spindle cusp magnetic field using the Boris particle pusher with elastic and inelastic collisions.

there is no geometric expression relating the cell's spatial location to it's index. It is very important to reduce the computational cost needed to find the cell index as the calculations must be repeated for each time step and for each particle. Therefore, the grid index for the residing particle is stored from the previous time step to reduce the required number of "location checks". This method limits the number of computations needed to only 9 cells rather than the entire domain. The only limitation is that the particles cannot translate across more than a single grid cell per time step which is already satisfied to reduce error in the tracker.

The location check algorithm calculates the cross product between the vector of each cell face to the vector of the particle's location to the corresponding vertex. The sign of the results informs which side of the cell boundary the particle resides. With careful programming, the particle's grid location can be determined from a maximum of 6 cross product calculations. The primary electron density contribution from the residing particle can then be estimated using:

$$\Delta n_{pe(i,j)} = \frac{I_{pe}\Delta t}{V_{(i,j)}} \tag{B.21}$$

where I_{pe} is the represented total current for the "super-particle" and $V_{(i,j)}$ is the cylindrical

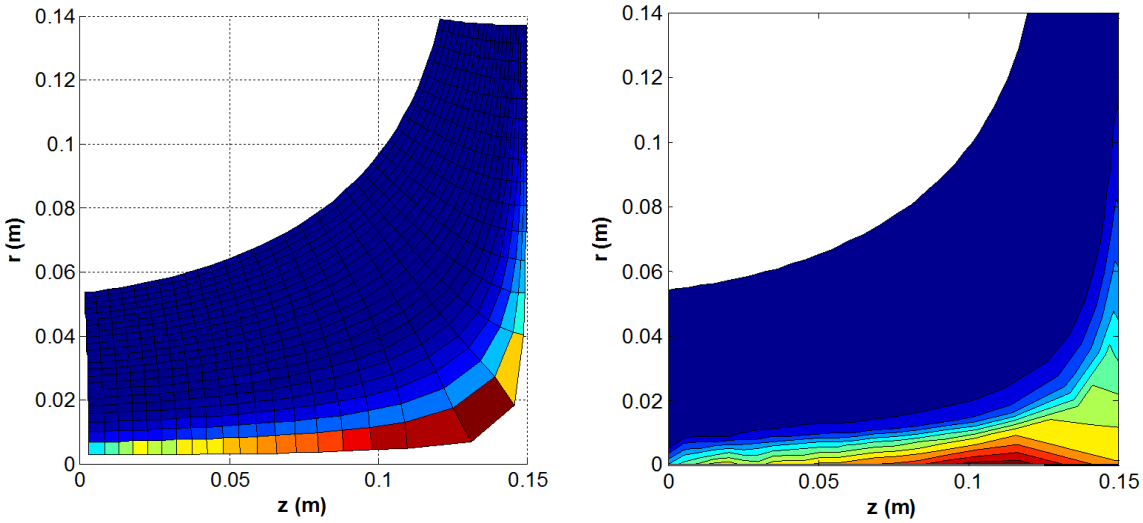

(a) Cell centered density

(b) Interpolated density

Figure B.6: Normalized primary electron density calculated from residence time based on the particle tracking data. The non-collisional particles remains predominately within the first couple streamlines.

volume of the residence cell. The raw results are shown in figure B.6a which based on a cell-centered coordinate. The values at the node points, shown in figure B.6b, are obtain through interpolation using a library function in MATLAB.

B.1.5 Numerical Method

The diffusion equation is solved using a finite volume method with the MFA mesh and particle tracking results for the generation term. As the mobility terms are dependent to the plasma density, the final solution is obtained iteratively by updating the mobility using plasma density values from the previous iteration. The process is repeated until the 2-norm of the plasma density change per iteration approach an acceptable tolerance. Eq. (B.3) is first integrated over a control volume and the divergence theorem is used to transform the

RHS into a surface integral:

$$\int_{CV} K_{iz} \mathrm{d}V = \int_{CV} \nabla \cdot \vec{\Gamma} \mathrm{d}V = \oint_S \vec{\Gamma} \cdot \hat{n} \mathrm{d}A \tag{B.22}$$

where $K_{i,j}$ is the generation rate of ions in each cell. A constant ionization rate is assumed within each grid cell as well as a constant flux along each face of the cell. Eq. (B.22) can then easily be integrated to:

$$K_{i,j} V_{i,j} = (\Gamma^{\parallel} S)_{i+\frac{1}{2}} + (\Gamma^{\parallel} S)_{i-\frac{1}{2}} + (\Gamma^{\perp} S)_{j+\frac{1}{2}} + (\Gamma^{\perp} S)_{j-\frac{1}{2}} \tag{B.23}$$

where the flux normal to each face is exactly parallel or perpendicular to the magnetic field. As diagramed in figure B.7, the geometry of a full MGA grid ensures that only one of the two anisotropic transport coefficients independently applies for a given cell face. The flux terms can then be rewritten using Eq. (B.7) and taking a first-order finite difference across each cell face to determine the density gradient:

$$\begin{aligned} K_{i,j} V_{i,j} = D^{\parallel}_{i,j} \left[(n_{i+1,j} - n_{i,j}) \left(\frac{S}{\Delta x} \right)_{i+\frac{1}{2}} + (n_{i-1,j} - n_{i,j}) \left(\frac{S}{\Delta x} \right)_{i-\frac{1}{2}} \right] ... \\ + D^{\perp}_{i,j} \left[(n_{i,j+1} - n_{i,j}) \left(\frac{S}{\Delta x} \right)_{j+\frac{1}{2}} + (n_{i,j-1} - n_{i,j}) \left(\frac{S}{\Delta x} \right)_{j-\frac{1}{2}} \right] \end{aligned} \tag{B.24}$$

The ionization rate for within each cell is proportional to the neutral density, ionization cross-section, and the primary electron density and energy, $K_{i,j} = n_{p(i,j)} n_0 \langle v_p \sigma \rangle_{iz}$. Since the diffusion coefficients are aligned with each cell, the Δx term is only the absolute spatial distance between the centroid of each cell.

The MFA mesh creates a stretched grid where each edge of the mesh boundary does not correspond to a single edge of the physical boundary. The two symmetric edges of the physical domain correspond to a single edge of the mesh boundary and can easily be described by a zero net flux condition, ie. $\Gamma_{sym} = 0$. The opposite edge of the computational mesh represents

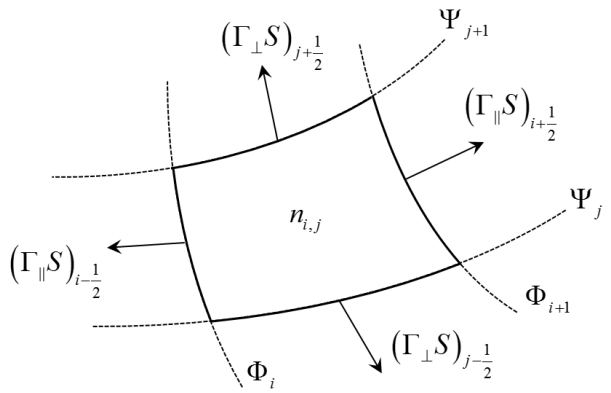

Figure B.7: Diagram of a finite volume grid cell in which the each side of the cell is exactly perpendicular or parallel to the local magnetic field.

the external vacuum chamber where the boundary conditions are ill defined. However, with an adequately sized computational domain, the plasma density should decay to a value where there would be negligible flux leaving the boundary because of the anisotropic diffusion rates. Nevertheless, the same cross-field diffusion rate from the adjacent flux tube is also imposed on the outer boundary. Plasma incident to the point and ring cusps are collected by a virtual anode plate where the cusp boundary cells are assumed to satisfy the Bohm criterion for a positive plasma sheath [58]. The assumption is reasonable assuming that the plasma potential is above the anode potential and that the boundary cell size is much larger than the sheath thickness. The ions therefore enter the thin sheath perpendicularly at the ion acoustic speed and the flux boundary conditions can be described by:

$$\Gamma_{cusp} = D\nabla n = n_{cusp} u_{Bohm} = n_{cusp}\sqrt{\frac{kT_e}{m_i}} \tag{B.25}$$

where n_{cusp} is the average plasma density at the cusp boundary cells and m_i is the molecular mass of the ion.

The finite volume method creates a separate equation for each cell in the grid in the form of Eq. (B.24) along with the proper boundary conditions. These equations are only linearly dependent of their neighboring cells and the system of equations can be transformed

into a sparse matrix of the form $Ax = b$, where x is the density of each cell in the mesh. The matrix is then solved using the MATLAB built in functions, "sparse" and "mldivide", consecutively.

B.2 Preliminary Results & Analysis

The results shown in this section are currently only exploratory and will be used as a tool to better understand the mechanics of the plasma loss. There are still many important components missing and rigorous care has not been taken to accurately fine tune the different collision frequencies and mobility parameters.

B.2.1 Simulation Conditions

The magnetic field and discharge conditions used for the computational model results in this section is shown in table B.1. The values represents the operating conditions of the spindle cusp experiment in appendix A.2.2. However, the loss width measured are too large due to the domain size limitation of the current MFA grid. Hence, the domain is scaled to a larger size while maintaining the same magnetic field strength at the cusp to increase the available cross-field diffusion path length.

Table B.1: Simulated discharge conditions

Parameter name	Symbol	Units	Value
coil radius		cm	25
coil separation		cm	20
coil current-turns		A	3000
xenon neutral density	n_0	m^{-3}	3×10^{18}
max electron temperature	T_e	eV	4
max ion temperature	T_i	eV	0.4
primary e^- energy	E_{pe}	eV	25
max primary e^- density	n_{pe}	m^{-3}	2×10^{15}

B.2.2 Model Results

The plasma density results for the condition in table B.1 are shown in figure B.8. The left contour plot is the the solution in the streamline or grid index coordinate. The right contour is the density values interpolated onto a cylindrical Cartesian grid where the highest scalar potential value corresponds to the location of the ring cusp. Although the maximum density in the model was scaled by adjusting the primary electron density, the overall structure of the plasma follows similar trends with the experimental measurements in figure A.12a. Particularly, the plasma density is seen to decrease rapidly towards the ring cusp and more slowly towards the point cusp. This is attributed to the cylindrical domain in which the expand as it flows radially outwards. A qualitative analysis of figure B.8a shows that the density diffuses across the streamlines primarily towards the ring cusp where the magnetic field is weaker and the streamlines are closer together. At the center or zeroth streamline, there is a negative gradient of plasma density from the null region towards both cusps. However, there is a general decrease in plasma density along the off-axis streamlines towards the point cusp. This indicates a fluid flow of diffused plasma from the ring to the point cusp region.

Figure A.12 highlights the plasma (n_e) and primary (n_p) electron density at the point and ring cusp. The line plot on the right shows the normalized densities across each of the cusp. The leak width of the non-diffusive primary electrons is approximately twice the Larmor radius at the ring cusp. Estimation of the width at the point cusp is unreliable due to the local grid resolution of the MFA mesh. The leak width of the plasma electrons is very similar despite the point cusp field strength being almost twice that of the ring cusp. Similar to the experimental measurements in appendix A.2.2, the leak width in general is much less than the geometric hybrid leak width. In addition, the point cusp profile from the model exhibits the same shoulder region shown as experimentally shown in figure B.1b.

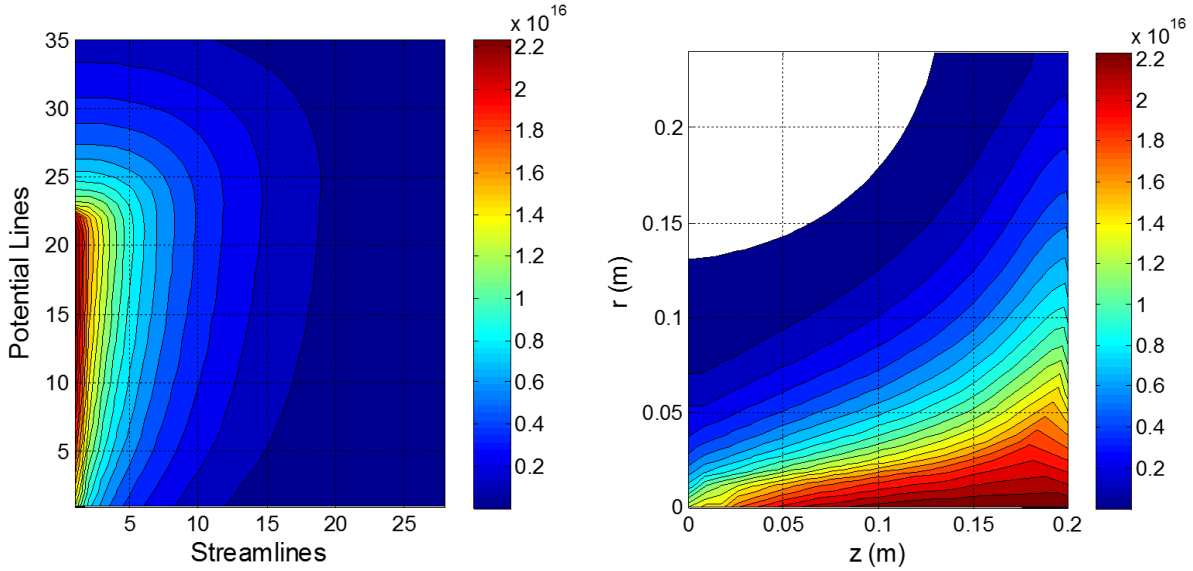

(a) Streamline coordinates **(b)** Cylindrical coordinates

Figure B.8: Discharge model result with simulation conditions shown in table B.1 plotted in two different coordinate system for analysis.

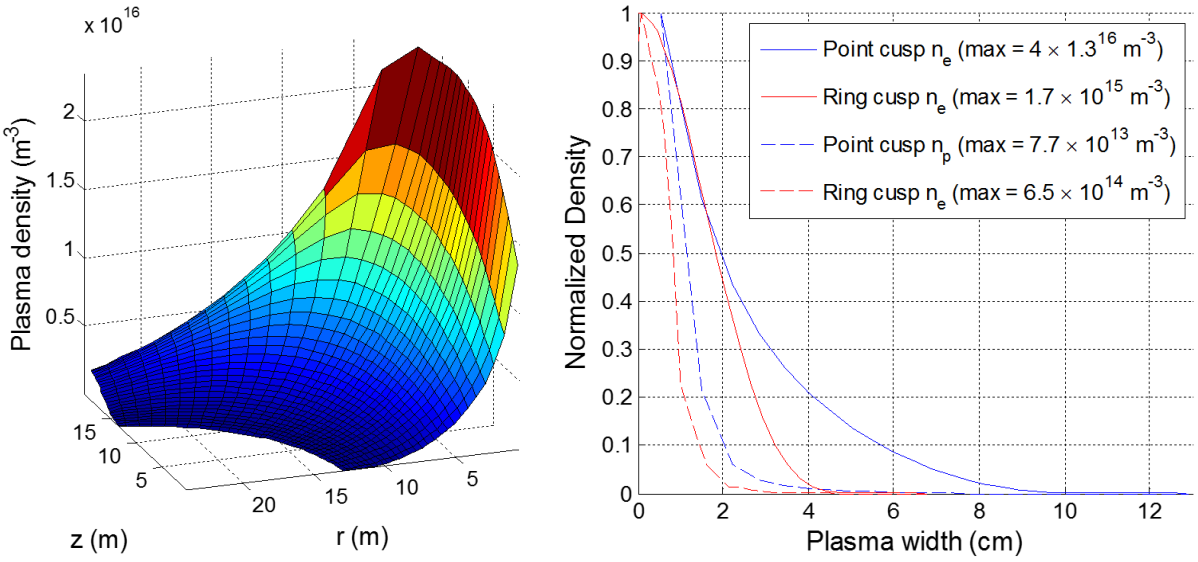

(a) Surface plot **(b)** Cusp leak profile

Figure B.9: Discharge model result plotted to highlight the structure of the plasma at the point and ring cusp anodes.

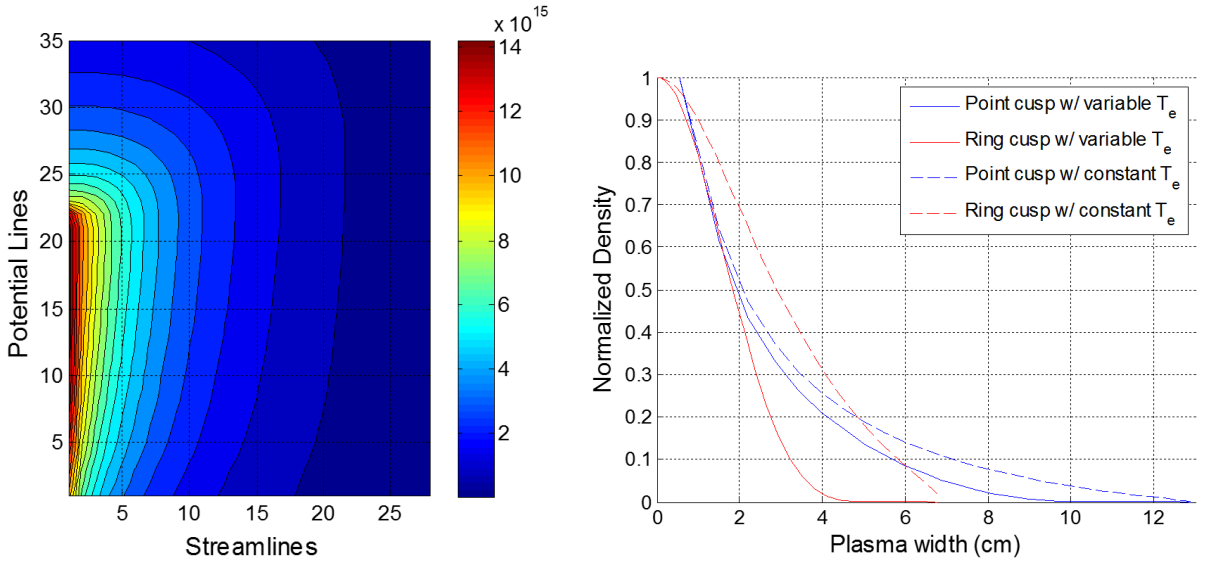

(a) Constant temperature

(b) Cusp leak profile

Figure B.10: Computational results comparing treatments of the electron temperature and showing the significance of properly resolving the electron temperature profile.

B.2.3 Temperature Gradients

As previously mentioned, the results shown in appendix B.2.2 required implemention of an artificial electron temperature profile. The contour plot shown in figure B.10 is for the same simulation but with a constant electron temperature. The plasma width at the ring cusp assuming constant temperature is almost twice the FWHM value compared to the variable temperature. In addition, the density spans across the entire computational domain which may have also imposed a computational limitation to the profile. The plasma radius at the point cusp is not significantly affected and maintains a similar profile. Although there is negligible change to the FWHM value at the point cusp, the shoulder region extends further out. It is unclear whether this is causes by higher diffusion at the point cusp or the diffuse plasma flowing from the ring cusp. Further investigation is required to better understand the effect of cusp geometry and temperature on the diffusion scaling parameters for the leak widths.

B.2.4 Cusp Interaction

It is expected that the large disparity between the parallel and perpendicular diffusion coefficient may be the cause of the large leak width at the point cusp. The results presented thus far have been for a condition similar to the experiment which has overall low field strengths. Figure B.11 shows the simulation results with a stronger magnetic field that is more similar to conditions from Bosch and Merlino. The comparison plot on the left shows that the ring cusp loss width has decreased by more than half. While the FWHM leak radius at the point cusp shows only slight decrease, the total area under the curve within the shoulder region is considerably reduced. In addition, the center density peak at the point cusp is more prominent with a better defined shoulder region and better resembles the profile shown in figure B.1b.

The results in figure B.12 shows a simulation where an artificial conducting wall is placed at the location marked by the red line. It spans across the diagonal of the domain sans the inner most grid cell. Physically, the wall prevents the diffuse particles from each cusp from interacting with each other while still allowing the primary electrons and the core plasma for pass. The purpose is to isolate the two cusp elements to investigate their contributions to each other. The results show a very slight change to the ring cusp, which is likely caused by the reduced plasma density. However, the shoulder region for the point cusp show a noticeable decrease. In addition, a kink in the plasma density can be seen at the location of the wall in a manner that clearly infers the suspected cusps interaction.

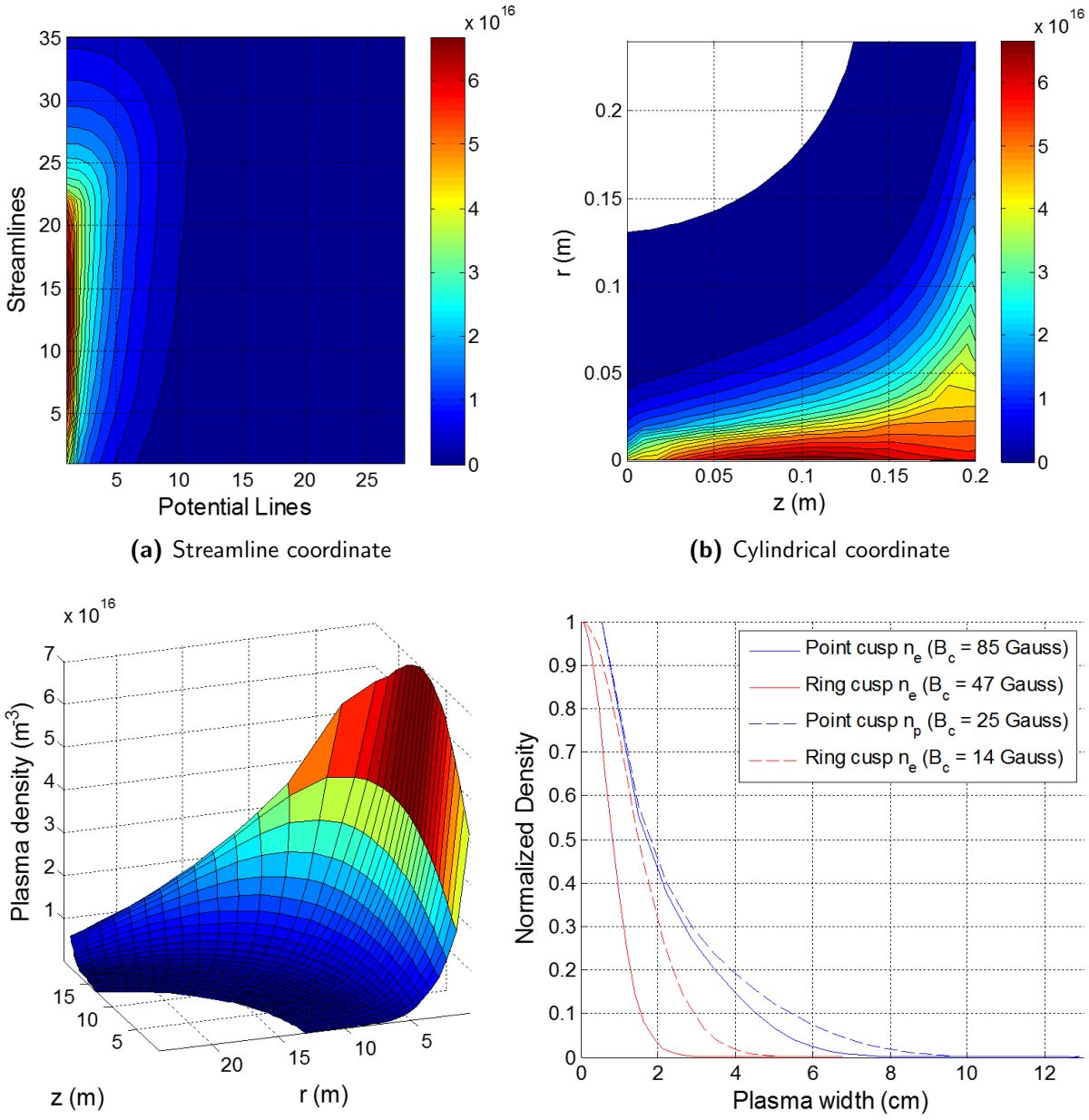

(a) Streamline coordinate

(b) Cylindrical coordinate

(c) Surface plot

(d) Cusp leak profile

Figure B.11: Computational results with higher coil currents showing better plasma confinement. The leak profile plot compares with results with the original magnetic field strength.

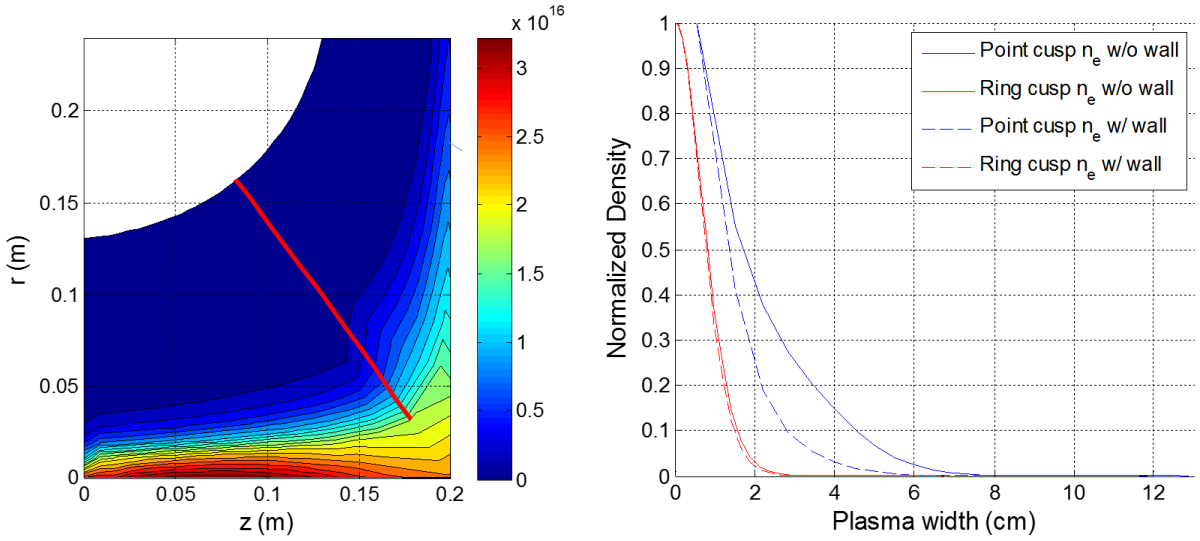

(a) Cylindrical coordinate

(b) Cusp leak profile

Figure B.12: Computation results with the higher magnetic field strength and a conducting wall boundary condition added across the domain as shown with the red line.

B.3 Conclusion and Future Work

A computational model was developed to be used as a tool for understanding the plasma behaviors seen in the experimental measurements. The results strongly suggest that the leak structure to a specific cusp element can be dramatically influenced by another, particularly in a variable radius cylindrical geometry. These interactions also show the importance of using a MFA mesh to reduce the effects of numerical diffusion. The effect of cusp interaction is expected to be much more dramatic for a miniature ring-cusp discharge. Although the radius of the device is much smaller, the magnetic field strength of a typical samarium cobalt ring magnet is significantly greater; whereas the magnetic field is highest at the point cusp for any normal spindle cusp device.

B.3.1 Improvement of Model

The diffusion equation is valid for when the inertial transport component is insignificant compared to the collisional component. This assumption is most likely to breakdown within the region approaching the point cusp where the magnetic field forms a nozzle shape. Magnetic nozzles are used for certain EP thrusters and the ions are able to obtain a Mach number of unity at the choke point given proper conditions. Although the ions are assumed to be loss at the sonic velocity in the model, this is obtained through the electric field in the sheath as imposed by the Bohm criterion rather than compression of the flow. For future analysis of the model validity, the inertial terms will be theoretically calculated from the results shown in figure B.8 and the magnitudes compared. Possibility for a correction factor may be explored and implemented to improve the accuracy of the model.

Even though the intention of this discharge model is only to simulate specific behavior of plasma diffusion, many important physical processes have yet to be implemented. Many of these assumptions and omissions were already stated throughout the model description but are listed here for clarity:

1. Include the effects of excitation collisions, thermalization, energy distribution and sheath boundaries, and potential profiles along magnetic field lines for the primary electron particle tracker.
2. Quantify effect of neutral depletion.
3. Solve the energy balance equation to properly determine the electron temperature profile.
4. Expand current limitations on the domain by combining several sets of structured MFA mesh.

References

[1] Wirz, R. E., Mueller, J., Gale, M., and Marrese, C., "Miniature Ion Engines for Precision Formation Flying," *40th AIAA/ASME/SAE/ASEE Joint Propulsion Conference & Exhibit*, Fort Lauderdale, Florida, 2004, AIAA 2004–4115.

[2] Martin, S., Scharf, D., Wirz, R. E., Lay, O., McKinstry, D., Mennesson, B., Purcell, G., Rodriguez, J., Scherr, L., Smith, J. R., and Wayne, L., "Design Study for a Planet-Finding Space Interferometer," *Proceedings of IEEE Aerospace Conference*, Big Sky, Montana, 2008.

[3] Conversano, R. and Wirz, R. E., "Mission Capability assessment of CubeSats Using a Miniature Ion Thruster," *AIAA Journal of Spacecraft and Rockets*, Vol. 50, No. 3, 2013.

[4] Tighe, W., Chien, K.-R., Ahn, J., Solis, E., Hurtado, J., and Spears, R., "Update on the XIPS 8-cm Thruster Prototype," *44th AIAA/ASME/SAE/ASEE Joint Propulsion Conference & Exhibit*, American Institute of Aeronautics and Astronautics, July 2008, AIAA-2008-4912.

[5] Christensen, J., Benson, G., Bond, T., Gallagher, J., and Matranga, M., "The NSTAR Ion Propulsion System for DS1," *35th AIAA/ASME/SAE/ASEE Joint Propulsion Conference & Exhibit*, American Institute of Aeronautics and Astronautics, Los Angeles, California, 1999, AIAA-99-2972.

[6] Wirz, R. E., "Miniature Ion Thrusters: A Review of Modern Technologies and Mission Capabilities," *34th International Electric Propulsion Conference*, Hyogo-Kobe, Japan, July 2015, IEPC-2015-275.

[7] Jahn, R. G., *Physics of Electric Propulsion*, Dover Publications, Inc., 2006.

[8] Goebel, D. M. and Katz, I., *Fundamentals of Electric Propulsion: Ion and Hall Thrusters*, John Wiley & Sons, New York, 2008.

[9] Arenberg, J. W. and Cash, W., "New Worlds Observer: A Novel Mission Concept for Exoplanetary Studies," *Direct Imaging of Exoplanets: Science and Techniques. Proceedings of the IAU Colloquium*, , No. 200, 2006, pp. 199–204.

[10] Russell, C. T., Wirz, R. E., Lai, H. R., Li, J.-Y., and Connors, M., "Smallsats with Ion Propulsion: An Affordable Approach to Meeting the Needs of Planetary Defense and Planetary Science at 1 AU," 2017.

[11] Wirz, R. E., Polk, J., Marrese, C., Mueller, J., Escobedo, J., and Sheehan, P., "Experimental and Computational Investigation of the Performance of a Micro-Ion Thruster," *38th AIAA/ASME/SAE/ASEE Joint Propulsion Conference & Exhibit*, Indianapolis, Indiana, 2002, AIAA 2002–3835.

[12] Wirz, R. E., *Discharge plasma processes of ring-cusp ion thrusters*, Ph.D. thesis, California Institute of Technology, Pasadena, CA, 2005.

[13] Goebel, D. M., Katz, I., Ziemer, J., Brophy, J. R., Polk, J. E., and Johnson, L., "Electric Propulsion Research and Development at JPL," *41th AIAA/ASME/SAE/ASEE Joint Propulsion Conference & Exhibit*, Tucson, Arizona, 2005, AIAA 2005–3535.

[14] Wirz, R. and Goebel, D., "Effects of magnetic field topography on ion thruster discharge performance," *Plasma Sources Science and Technology.*, Vol. 17, No. 3, Aug. 2008, pp. 035010.

[15] Goebel, D., Polk, J., and Sengupta, A., "Discharge Chamber Performance of the NEXIS Ion Thruster," *40th AIAA/ASME/SAE/ASEE Joint Propulsion Conference & Exhibit*, American Institute of Aeronautics and Astronautics, Fort Lauderdale, Florida, July 2004, AIAA-2004-3813.

[16] Limpaecher, R. and MacKenzie, K., "Magnetic Multipole Containment of Large Uniform Collisionless Quiescent Plasmas," *Review of Scientific Instruments*, Vol. 44, No. 6, Nov. 1973, pp. 726.

[17] Hershkowitz, N., Leung, K. N., and Romesser, T., "Plasma Leakage Through a Low-Line Cusp," *Physical Review Letters*, Vol. 35, No. 5, Aug. 1975, pp. 277–280.

[18] Dolan, T., "Magnetic electrostatic plasma confinement," *Plasma Physics and Controlled Fusion*, Vol. 36, No. 10, Oct. 1994, pp. 1539–1593.

[19] Bohm, D. and Gross, E. P., "Theory of Plasma Oscillation. B. Excitation and Damping of Oscillations," *Physical Review*, Vol. 75, No. 12, 1949, pp. 1864–1876.

[20] Leung, K., Hershkowitz, N., and MacKenzie, K., "Plasma confinement by localized cusps," *Physic of Fluids*, Vol. 19, No. 7, 1976, pp. 1045–1053.

[21] Bosch, R. and Merlino, R., "Confinement properties of a lowbeta discharge in a spindle cusp magnetic field," *Physic of Fluids*, Vol. 29, No. 6, 1986, pp. 1998–2006.

[22] Christensen, T., Hershkowitz, N., and Leung, K. N., "Mass Scaling of Permanent Magnet Line Cusp Plasma Leaks," *IEEE Transactions on Plasma Science*, Vol. 5, No. 1, 1977, pp. 23–26.

[23] Matlock, T., Lozano, P., and Martinez-Sanchez, M., "Discharge Chamber Wall Flux Measurements in a Diverging Cusped-Field Thruster," *ESA/3AF Space Propulsion Conference*, San Sebastian, Spain, 2010.

[24] Hubble, A. and Foster, J., "Spatially resolved study of primary electron transport in magnetic cusps," *Journal of Vacuum Science and Technology A*, Vol. 30, No. 1, Nov. 2012, pp. 011301.

[25] Koch, C. and Matthieussent, G., "Collisional diffusion of a plasma in multipolar and picket fence devices," *Physics of Fluids*, Vol. 26, No. 2, Feb. 1983, pp. 545.

[26] Knorr, G. and Merlino, R. L., "The role of fast electrons for the confinement of plasma by magnetic cusps," *Plasma Phys. and Control. Fusion*, Vol. 26, No. 2, Feb. 1984, pp. 433–442.

[27] Goebel, D. M., Wirz, R. E., and Katz, I., "Analytical Ion Thruster Discharge Performance Model," *Journal of Propulsion and Power*, Vol. 23, No. 5, Sept. 2007, pp. 1055–1067.

[28] Goebel, D. M., "Ion source discharge performance and stability," *Physics of Fluids*, Vol. 25, No. 6, 1982, pp. 1093–1102.

[29] Sengupta, A., "Magnetic Confinement in a Ring-Cusp Ion Thruster Discharge Plasma," *Journal of Applied Physics*, Vol. 105, No. 093303, 2009, pp. 1–10.

[30] Huddleson, J., Brandon-Cox, J., Wallace, N., and Palencia, J., "An Overview of the T6 Gridded Ion Propulsion System Pre-Development Activities for Alpha-Bus," *4th International Spacecraft Propulsion Conference*, Chia Laguna, Cagliari, June 2004.

[31] Moore, D. R., "Magneto-electrostatically contained plasma ion thruster," *7th Electric Propulsion Conference*, Williamsburg, Virginia, 1969.

[32] Mao, H.-S., *Plasma Structure and Behavior of Miniature Ring-Cusp Discharges*, Ph.D. thesis, University of California, Los Angeles, 2013.

[33] Wirz, R., "Computational Modeling of a Miniature Ion Thruster Discharge," *41st AIAA/ASME/SAE/ASEE Joint Propulsion Conference & Exhibit*, American Institute of Aeronautics and Astronautics, Tucson, Arizona, July 2005.

[34] Jones, R., "Cusp leak width reduction by electron beam injection," *Plasma Physics*, Vol. 23, No. 4, April 1981, pp. 381–383.

[35] Anukaliani, A. and Selvarajan, V., "Loss of plasma scaling with magnetic field, pressure and discharge current in a CUSP confined plasma," *The European Physical Journal - Applied Physics*, Vol. 15, No. 3, Sept. 2001, pp. 199–206.

[36] Wirz, R., "Near-Surface Cusp Confinement for Weakly Ionized Plasma," *46th AIAA/ASME/SAE/ASEE Joint Propulsion Conference & Exhibit*, American Institute of Aeronautics and Astronautics, San Jose, California, July 2012.

[37] Engel-Herbert, R. and Hesjedal, T., "Calculation of the magnetic stray field of a uniaxial magnetic domain," *Journal of Appied. Physics*, Vol. 97, No. 7, 2005, pp. 074504.

[38] Babic, S. and Akyel, C., "Improvement in the analytical calculation of the magnetic field produced by permanent magnet rings," *Progress in Electromagnetics Research*, Vol. 5, 2008, pp. 71–82.

[39] Boris, J. P., "Relativistic plasma simulations-optimization of a hybrid code," *Proceedings of the 4th Conference of Numerical Simulation of Plasmas*, Washington DC, 1970.

[40] Mao, H.-S. and Wirz, R. E., "Plasma Structure of Miniature Ring-Cusp Ion Thruster Discharges," *Journal of Propulsion and Power*, Vol. 30, No. 3, 2014, pp. 628–636.

[41] Mahalingam, S. and Menart, J. A., "Particle-Based Plasma Simulations for an Ion Engine Discharge Chamber," *Journal of Propulsion and Power*, Vol. 26, No. 4, 2010.

[42] Herman, D. A. and Gallimore, A. D., "Discharge Cathode Electron Energy Distribution Functions in a 40-cm NEXT-type Ion Engine," *41st AIAA/ASME/SAE/ASEE Joint Propulsion Conference & Exhibit*, American Institute of Aeronautics and Astronautics, Tucson, Arizona, July 2005, AIAA-2005-4252.

[43] Druyvesteyn, M., "Der Niedervoltbogen," *Zeitschrift fr Physik*, Vol. 64, 1930, pp. 781–798.

[44] Popov, T., Ivanova, P., Kovacic, J., and Gyergyek, T., "Langmuir probe measurements of the electron energy distribution function in magnetized gas discharge plasma," *Plasma Sources Science and Technology*, Vol. 21, 2012.

[45] Laframboise, J., *Theory of spherical and cylindrical Langmuir probes in a collisionless, maxwellian plasma at rest*, Ph.D. thesis, University of Toronto Institute for Aerospace Studies, 1966.

[46] Havlickova, E. and Hrach, R., "Numerical investigations of sheath structure inpresence of magnetic field," *Journal of Physics: Conference Series*, Vol. 207, 2010.

[47] Ibehej, T. and Hrach, R., "Computational Study of Sheath Structurein the Presence of Magnetic Field," *WDS'12 Proceedings of Contributed Papers, Part II*, 2012, pp. 87–92.

[48] Chen, F., "Langmuir probes in RF plasma: surprising validity of OML theory," *Plasma Sources Science and Technology*, Vol. 18, 2009.

[49] Crowley, B., Homfray, D., Fantz, U., Boilson, D., and Hemsworth, R. S., "Electron Energy Distribution Function Measurements by Langmuir Probe in ITER like Negative Ion Sources," *AIP Conference Preceeding*, Vol. 925, 2007.

[50] Brophy, J., *Ion Thruster Performance Model*, Ph.D. thesis, Colorado State University, Fort Collins, Colorado, 1984.

[51] Herman, D. A. and Gallimore, A. D., "An ion thruster internal discharge chamber electrostatic probe diagnostic technique using a high-speed probe positioning system," *Review of Scientific Instruments*, Vol. 79, No. 013302, Jan. 2008.

[52] Hubble, A. A., Foster, J. E., Barnat, E. V., and Weatherford, B. R., "Laser-Collisional Induced Fluorescence Study of Electron Distributions in a Magnetic Cusp," *33rd International Electric Propulsion Conference*, Washington D.C., USA, Oct. 2013, IEPC-2013-367.

[53] Tsukizaki, R., Toshiyuk, I., Hiroyoshi, T., Nishiyama, K., and Kuninaka, H., "Thrust Enhancement of a Microwave Ion Thruster," *Journal of Propulsion and Power*, Vol. 30, No. 5, 2014, pp. 1383–1389.

[54] Foster, J. E. and Patterson, M. J., "Internal plasma properties and enhanced performance of 8-cm ion thruster discharge," *Journal of Propulsion and Power*, Vol. 17, No. 2, 2001, pp. 5.

[55] Brophy, J. R., "Simulated ion thruster operation without beam extraction," *21st International Electric Propulsion Conference*, Orlando, Florida, 1990, IEPC-1990-2655.

[56] Foster, J. E., Hubble, A., Nowak-Gucker, S., Davis, C., Peterson, P., Viges, E., and Chen, D., "Simulated Beam Extraction Performance Characterization of a 50-cm Ion Thruster Discharge," *48th AIAA/ASME/SAE/ASEE Joint Propulsion Conference & Exhibit*, American Institute of Aeronautics and Astronautics, Atlanta, Georgia, July 2010, AIAA-2012-3795.

[57] Wirz, R., Sullivan, R., Przybylowski, J., and Silva, M., "Hollow Cathode and Low-Thrust Extraction Grid Analysis for a Miniature Ion Thruster," *International Journal of Plasma Science and Engineering*, Vol. 2008, 2008, pp. 1–11.

[58] Riemann, K., "Review article: The Bohm criterion and sheath formation," *Journal of Physics D: Applied Physics*, Vol. 24, 1990, pp. 493–518.

[59] Willams, G. J., Domonkos, M. T., and Chavez, J. M., "Measurement of Doubly Charged Ions in Ion Thruster Plumes," *27th International Electric Propulsion Conference*, Pasadena, California, Oct. 2001, IEPC-01-310.

[60] Mantenieks, M. A., "Sputtering Threshold Energies of Heavy Ions," *25th International Electric Propulsion Conference*, Cleveland, Ohio, Aug. 1997, IEPC-97-187.

[61] Rapp, D. and Englander-Golden, P., "Total Cross Sections for Ionization and Attachment in Gases by Electron Impact: I. Positive Ionization," *The Journal of Chemical Physics*, Vol. 43, No. 5, 1965, pp. 1464–1479.

[62] Hayashi, M., "Determination of Electron-Xenon Total Excitation Cross-Sections, from Threshold to 100 eV, from Experimental Values of Townsend's α," *Journal of Physics D: Applied Physics*, Vol. 16, 1983, pp. 581–589.

[63] Bell, E. W., Djurić, N., and Dunn, G. H., "Electron-impact ionization of In^+ and Xe^+," *Physical Review A*, Vol. 48, No. 6, 1993.

[64] Spitzer, L. J., *Physics of Fully Ionized Gases*, Interscience, New York, 1962.

[65] Sydorenko, D., Smolyakov, A., Kaganovich, I., and Raitses, Y., "Effects of non-Maxwellian electron velocity distribution function on two-stream instability in low-pressure discharges," *Physics of Plasmas*, Vol. 14, No. 013508, 2007, pp. 8.

[66] Simon, A., "Ambipolar Diffusion in a Magnetic Field," *Physical Review*, Vol. 98, No. 317, 1955.

[67] Brussaard, G., van der Steen, M., Carrere, M., van de Sanden, M., and Schram, D., "Langmuir probe measurements in an expanding magnetized plasma," *Physical Review E*, Vol. 54, No. 2, 1996, pp. 1906–1911.

[68] Godyak, V. and Demidov, V., "Prove measurements of electron-energy distribution in plasmas: what can we measure and how can we achieve reliable results?" *Journal of Physics D: Applied Physics*, Vol. 44, 2011.

[69] Chegotov, M., "A new regularization procedure as an appropriate algorithm for the evaluation of Langmuir-probe and Thomson scattering measurements," *Journal of Physics D: Applied Physics*, Vol. 27, 1994, pp. 54–62.

[70] Gutirrez-Tapia, C. and Flores-LLamasl, H., "A comparative analysis of the electron energy distribution function obtained by regularization methods and by a least-squares fitting," *Physics of Plasmas*, Vol. 11, No. 11, 2004, pp. 5102–5107.

[71] Singh, A. and Rowe, J., "Enhancement of Plasma Density in an Arc Discharge," *Journal of Applied Physics*, Vol. 36, No. 11, 1965, pp. 3535–3539.

[72] Longmier, B., Bering III, E., Carter, M., Leonard, C., Chancery, W., Franklin, C., Glover, T., Hershkowitz, N., Ilin, A., McCaskill, G., Olsen, C., and Squire, J., "Ambipolar ion acceleration in an expanding magnetic nozzle," *Plasma Sources Science and Technology*, Vol. 20, 2011.

[73] Merino, M. and Ahedo, E., "Influence of Electron and Ion Thermodynamics on the Magnetic Nozzle Plasma Expansion," *IEEE Transactions on Plasma Science*, 2014.

[74] Mikellides, I. and Katz, I., "Numerical simulations of Hall-effect plasma accelerators on a magnetic-field-aligned mesh," *Physical Review E*, Vol. 86, 2012.

[75] Araki, S. J., "Cell-Centered Particle Weighting Algorithm for PIC Simulations in a Non-Uniform 2D Axisymmetric Mesh," *Journal of Computational Physics*, Vol. 272, 2014, pp. 218–226.

[76] Ravaud, R., Lemarquand, G., Lemarquand, V., and Depollier, C., "Analytical Calculation of the Magnetic Field Created by Permanent-Magnet Rings," *IEEE Transactions on Magnetics*, Vol. 44, No. 8, 2008, pp. 1982–1989.

[77] Wagenaar, R. W. and de Heer, F. J., "Total Cross Sections for Electron Scattering from Ar, Kr and Xe," *Journal of Physics B: Atomic, Molecular and Optical Physics*, Vol. 18, 1985, pp. 2021–2036.

[78] Ester, T. and Kessler, J., "Absolute Elastic and Inelastic Electron Scattering Cross Sections for Xenon in the 15–100 eV Impact-Energy Region," *Journal of Physics B: Atomic, Molecular and Optical Physics*, Vol. 27, 1994, pp. 4295–4308.

[79] Chiu, Y.-H., Dressler, R. A., Levandier, D. J., Houchins, C., and Ng, C. Y., "Large-Angle Xenon Ion Scattering in Xe-Propelled Electrostatic Thrusters: Differential Cross Sections," *J. Phys. D: Appl. Phys.*, Vol. 41, 2008, pp. 165503.